JOURNAL OF GEOPHYSICAL RESEARCH, VOL. 85, NO. B11, PAGES 6185–6222, NOVEMBER 10, 1980

Heat Flow and Energetics of the San Andreas Fault Zone

ARTHUR H. LACHENBRUCH AND J. H. SASS

U.S. Geological Survey, Menlo Park, California

Approximately 100 heat flow measurements in the San Andreas fault zone indicate (1) there is no evidence for local frictional heating of the main fault trace at any latitude over a 1000-km length from Cape Mendocino to San Bernardino, (2) average heat flow is high (~2 HFU, ~80 mW m^{-2}) throughout the 550-km segment of the Coast Ranges that encloses the San Andreas fault zone in central California; this broad anomaly falls off rapidly toward the Great Valley to the east, and over a 200-km distance toward the Mendocino Triple Junction to the northwest. As others have pointed out, a local conductive heat flow anomaly would be detectable unless the frictional resistance allocated to heat production on the main trace were $\lesssim$100 bars. Frictional work allocated to surface energy of new fractures is probably unimportant, and hydrologic convection is not likely to invalidate the conduction assumption, since the heat discharge by thermal springs near the fault is negligible. Explanations for the low dynamic friction fall into two intergradational classes: those in which the fault is weak all of the time and those in which it is weak only during earthquakes (possibly just large ones). The first class includes faults containing anomalously weak gouge materials and faults containing materials with normal frictional properties under near-lithostatic steady state fluid pressures. In the second class, weakening is caused by the event (for example, a thermally induced increase in fluid pressure, dehydration of clay minerals, or acoustic fluidization). In this class, unlike the first, the average strength and ambient tectonic shear stress may be large, ~1 kbar, but the stress allocated to elastic radiation (the apparent stress) must be of similar magnitude, an apparent contradiction with seismic estimates. Unless seismic radiation is underestimated for large earthquakes, it is difficult to justify average tectonic stresses on the main trace of the San Andreas fault in excess of ~200 bars. The development of the broad Coast Range heat flow anomaly southward from Cape Mendocino suggests that heat flow increases by a factor of 2 within 4 m.y. after the passage of the Mendocino Triple Junction. This passage leaves the San Andreas transform fault zone in its wake; the depth of the anomalous sources cannot be much greater than the depth of the seismogenic layer. Some of the anomalous heat may be supplied by conduction from the warmer mantle that must occur south of the Mendocino transform (where there is no subducting slab), and some might be supplied by shear heating in the fault zone. With no contribution from shear heating, extreme mantle upwelling would be required, and asthenosphere conditions should exist today at depths of only ~20 km in the northernmost Coast Ranges. If there is an appreciable contribution from shear heating, the heat flow constraint implies that the seismogenic layer is partially decoupled at its base and that the basal traction is in the sense that resists right lateral motion on the fault(s). As a result of these basal tractions, the average shearing stress in the seismogenic layer would increase with distance from the main fault, and the seismogenic layer would offer substantial resistance to plate motion even though resistance on the main fault might be negligible. These speculative models have testable consequences.

INTRODUCTION

The simplest models of pure strike slip upper-crustal earthquakes such as those on the San Andreas fault can be considered in terms of three fundamental stresses: an average component of shearing traction in the direction of fault slip that exists at the onset of faulting, a corresponding component that exists at the conclusion of faulting, and an average resisting stress that results in the local conversion and loss of mechanical energy during an earthquake. Indirect estimates based on seismological observations provide information on differences among these generalized stresses but not on their absolute magnitudes. Similarly, geodetic observations of deformation at the earth's surface provide information on rates of accumulation and release of strain, but they do not generally distinguish between elastic and inelastic components, and in any case, they provide no means of extracting the absolute value of elastic strain necessary to estimate the magnitudes of the fundamental stresses. Although seismologic and geodetic observations have resulted in a substantial increase in the understanding of earthquakes, our ignorance of the magnitudes of the stresses precludes an understanding of their energetics. With the present uncertainty in these three quantities (perhaps an order of magnitude) we can scarcely claim to understand the physics of earthquakes or the resistance to plate motions. It is seen that with seismologic estimates of two independent relations among the stresses (for example, apparent stress and stress drop), it is in principle possible to estimate the magnitudes of all three stresses from an estimate of the magnitude of any one of them. Measurements of rock friction provide additional useful constraints. In the first part of this paper, we address the problem of estimating the magnitude of the resisting stress from considerations of the thermal budget of the fault zone.

It was pointed out by *Brune et al.* [1969] that for the long-term average displacement rates that have been documented on the San Andreas fault, the frictional heat generation should result in a conspicuous local heat flow anomaly if the average dynamic frictional resistance in the seismogenic zone exceeded a hundred bars or so. Since no such heat flow anomaly had been observed, it was concluded that this stress limit applied. Applying seismically derived constraints on stress drop and apparent stress, they concluded that the initial (tectonic) stress was probably limited to about 250 bars. Additional heat flow measurements and analysis [*Henyey and Wasserberg*, 1971; *Lachenbruch and Sass*, 1973] generally supported these conclusions. In a recent study of New Zealand's Alpine fault, however, *Scholz et al.* [1979] interpret local thermal metamorphism and argon depletion as evidence

Paper number 80B0929.

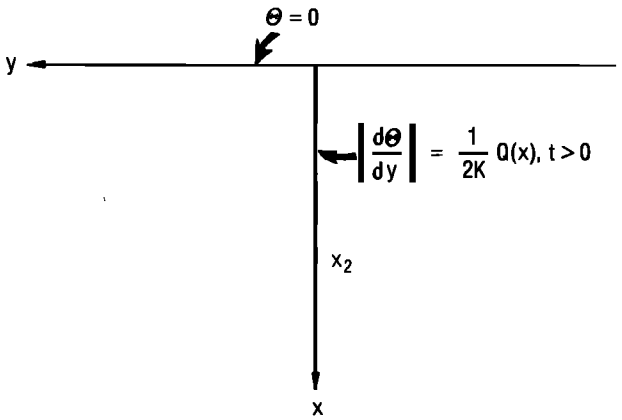

Fig. 1. Conditions for the problem of frictional heating on a strike slip fault.

that dynamic friction in the seismogenic zone of that fault averaged at least 1 kbar.

Conclusions from all of these studies were based upon heat conduction models, which are elaborated somewhat in the next section and then applied to the heat flow data presently available near the San Andreas fault. The new data generally confirm the conclusions of earlier studies, viz., that there is no detectable local heat flow anomaly at the San Andreas fault trace. After considering the probability of heat removal by hydrologic processes, we conclude that it is unlikely and consequently, that the 100-bars limit on average frictional resistance probably applies while fault motion is in progress. We then consider the heat flow constraint in terms of generalized results on rock friction and seismic stress differences and confirm that if the constraint on total seismic radiation is taken at face value, the fault must be surprisingly weak even when fault motion is not in progress. Following these considerations of heat flow near the fault trace, we examine the broad heat flow anomaly observed throughout the California Coast Ranges and its implications for the evolution and mechanical behavior of the San Andreas fault zone.

Resisting Stress and Long-Term Thermal Effects of Strike Slip Faulting

When slip occurs on a fault, elastic energy stored in the earth is released. Some may appear as kinetic energy of seismic radiation that leaves the fault zone, and the remainder is consumed locally in overcoming the resistance offered by the fault to progress of the slip motion. (In a recent model by *Melosh* [1979], resistance to the moving fault surface is reduced by acoustic oscillations. In our analysis of energetics, the acoustic energy absorbed in the vicinity of the fault will contribute to the fault resistance, and any remainder, to the radiated energy.) Despite its importance to the understanding of earthquakes and crustal stress, the magnitude of this resistance is unknown. Some of the work done against fault resistance must be allocated to the production of heat through various small-scale inelastic frictional processes; the rest could be consumed by other energy sinks such as metamorphic and chemical reactions or by the surface energy associated with the creation of new fractures and flaws. Although the nonthermal portions are generally expected to be small, they probably should be identified and evaluated systematically. In this section, we shall attempt to evaluate only the effects of surface energy. We shall then discuss the theory necessary to evaluate the thermal part of the resistance on the assumption that the frictionally generated heat is transmitted by conduction (an assumption we examine in a later section).

If the sliding motion of two rigid blocks with uniform relative velocity $2v$ is opposed by an average resisting stress $\bar{R}$, the rate of energy dissipation per unit fault area can be written as

$$2v\bar{R} = D + Q \tag{1}$$

where D is the average rate at which energy is consumed by creating new surface, and Q is the average rate of mechanical heat generation. If R_δ and τ represent the portions of the total resisting stress $\bar{R}$ allocated, respectively, to each process, then

$$D = 2vR_\delta \tag{2}$$

$$Q = 2v\tau \tag{3}$$

$$\bar{R} = R_\delta + \tau \tag{4}$$

We shall first consider the relative importance of R_δ.

The Role of Surface Energy

Consider a portion of a fault surface of area A that has been active for a time t during which relative displacement $2vt = 2u$ has occurred. We suppose that this motion has resulted in the creation of new surfaces of area a and specific surface energy δ, i.e.,

$$D = \frac{a\delta}{At}$$

Then from (2),

$$R_\delta = \frac{a\delta}{2uA} \tag{5}$$

If the newly created surface a is represented by a gouge zone of half-width B composed of cubes with dimension b, then

$$a \cong \frac{6AB}{b} \tag{6}$$

and

$$R_\delta \cong \frac{3\delta}{b}\frac{B}{u} \tag{7}$$

According to a careful study by *Brace and Walsh* [1962], δ is in the range 200–2000 erg/cm^2 for a wide variety of common rock-forming minerals. Taking $b \sim 1$ micron (10^{-4} cm) and $\delta \sim 10^3$ erg/cm^2, (7) yields

$$R_\delta \sim 3 \times 10^7 \frac{B}{u}\left(\frac{d}{\text{cm}^2}\right) = 30\frac{B}{u}\text{ [bars]} \tag{8}$$

Hence for these values the resisting stress allocated to fracture will not exceed 30 bars unless the ratio of gouge width to fault displacement exceeds $\sim 10°$. For the San Andreas fault, this ratio is probably $\lesssim 10^{-2}$ ($B \lesssim 1$ km, $u \gtrsim 100$ km), which seems to allow us to neglect R_δ with some room for error in the choices of b and δ.

It is important to distinguish between surface energy and the 'fracture energy' used in models of macroscopic fracture; most of the fracture energy ultimately appears as heat. In studies reported by *McGarr et al.* [1979], specific 'crushing energies' of about 5×10^5 erg/cm^2 were determined from crushing tests on quartzite. They emphasize, however, that it

is not known how the work of crushing was partitioned among surface energy, heat, and elastic waves.

It might be argued that over periods of millions of years the gouge might be repeatedly healed and refractured. Although this could be important to the energetics of individual events, it seems likely that the healing process would release the surface energy as heat, and no long-term cumulative storage as surface energy would result. In what follows, we shall neglect the contribution of surface energy and use the symbols τ and $\bar{R}$ interchangeably.

Thermal Effects

Equation (3) forms the basis for attempts to estimate resisting stress ($\bar{R} \cong \tau$) from measurements of surface heat flow [*Henyey*, 1968; *Brune et al.*, 1969; *Henyey and Wasserburg*, 1971; *Lachenbruch and Sass*, 1973; *Scholz et al.*, 1979]. In this section, we present results for heat flow and fault temperature that will be useful background for the discussions to follow. We consider the thermal effects of frictional heating by a vertical strike slip fault in the plane $y = 0$ in the half-space $x > 0$ (Figure 1). A frictional heat source of strength

$$Q(x) = 2v\tau(x) \tag{9}$$

starts at time $t = 0$, when the fault originates. From that time onward, the average slip velocity $2v$ and average dissipative resistance $\tau(x)$ are both assumed to be independent of time. Consequently, the rate of heat generation does not, on the average, change with time. The earth's surface $x = 0$ is maintained at zero temperature, the medium is homogeneous with thermal conductivity $K = 0.006$ cal/cm s °C (~2.5 W m^{-1} K^{-1}), and thermal diffusivity $\alpha = 0.01$ cm^2/s. Thermal conduction is the only mode of heat transfer, and the fault is considered to be infinitely extended in the direction perpendicular to the x, y plane. In Appendix A, analytical results

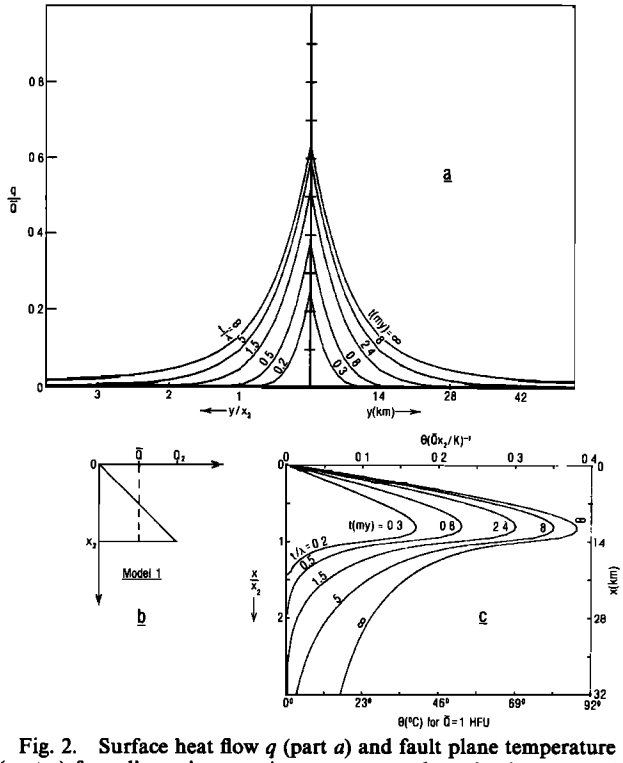

Fig. 2. Surface heat flow q (part *a*) and fault plane temperature θ (part *c*) for a linear increase in source strength to depth x_2 (part *b*). Dimensional results are for $x_2 = 14$ km, $K = 6$ mcal/cm s °C, and $\lambda = (x_2)^2/4\alpha = 1.6$ m.y.

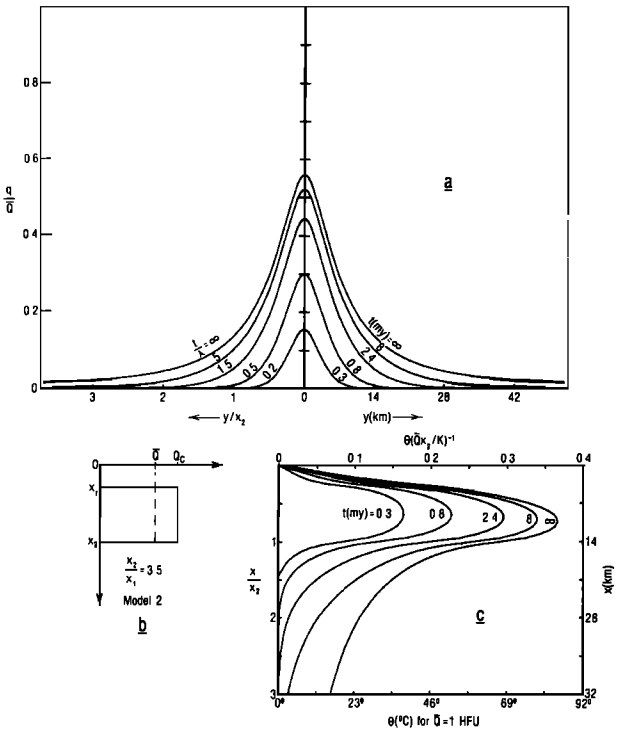

Fig. 3. Surface heat flow q (part *a*) and fault plane temperature θ (part *c*) for source strength distribution shown in Figure 3*b*. Dimensional results are for $x_2 = 14$ km, $K = 6$ mcal/cm s °C, and $\lambda = 1.6$ m.y.

for surface heat flow and fault plane temperature are given for two cases: model 1, a linear increase in $Q(x)$ from zero at the surface to Q^* at $x = x_2$, with zero source strength elsewhere (see Figure 2*b*), and model 2, a source of uniform strength Q_c between depths x_1 and x_2, with zero strength elsewhere (Figures 3*b* and 4*b*). (For model 2, the transient temperature distribution throughout the entire medium is given, equation (A8).) Results for these models can be superimposed to describe the effects of any source distribution $Q(x)$ composed of step and linear functions; a simple useful example is model 3, Figure 5*b*. In Figures 2–5, the results are normalized by $\bar{Q}$, the average rate of frictional heat production between the surface and x_2, and q represents heat flow at the earth's surface. The well-known results for steady state heat flow (appendix A, (A22*b*) and (A23*b*)) are represented by the curves labeled $t = \infty$ in Figures 2*a*, 3*a*, 4*a*, and 5*a*. The other curves in parts *a* of these figures represent transient states labeled in dimensionless quantities on the left, and dimensional ones on the right (using $x_2 = 14$ km, $\alpha = 0.01$ cm^2/s). The time constant is $\lambda = (x_2)^2/4\alpha$; it is about 1.6 m.y. for $x_2 = 14$ km, or 0.8 m.y. for $x_2 = 10$ km. Such depths are comparable to the thickness of the seismogenic layer for continental strike slip faults. Within this layer we often have reasonable assurance from microseismicity that a substantial amount of slip occurs in a narrow zone [e.g., *Eaton et al.*, 1970]. Beneath the seismogenic layer, the mode of mechanical deformation and heat generation is more obscure, but fortunately, the effect of such deep sources on the local heat flow anomaly is relatively unimportant. For example, increasing the depth x_2 of heat production from 14 km to 28 km in the model of Figure 4*b* would increase the maximum heat flow anomaly by only 15% after 10 m.y. of faulting (A23*a*), and near the fault the general form of the anomaly would be changed little.

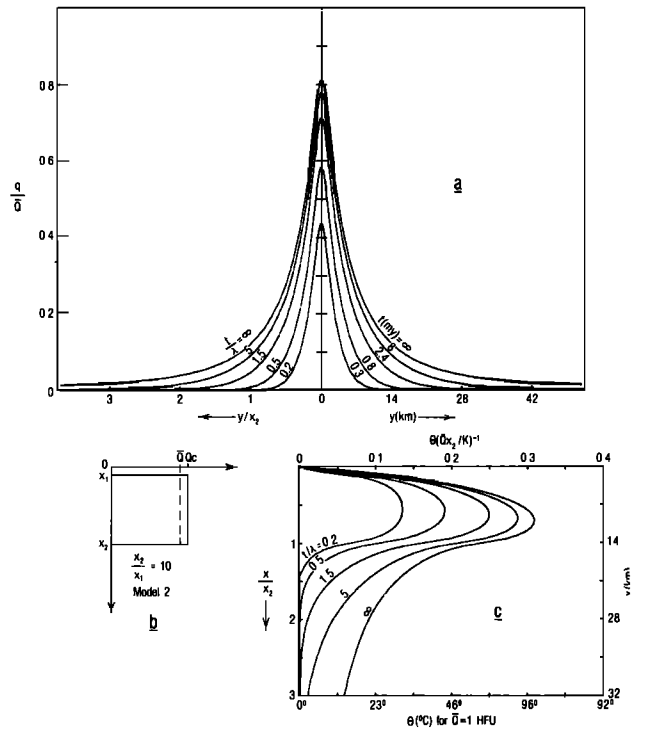

Fig. 4. Surface heat flow q (part a) and fault plane temperature θ (part c) for source strength distribution shown in Figure 4b. Dimensional results are for x_2 = 14 km, K = 6 mcal/cm s °C, and λ = 1.6 m.y.

The temperature rise on the fault plane is shown in parts c of Figures 2–5. On the upper scale, they are normalized by the 'scale temperature,' $\bar{Q}x_2/K$, which is the one-dimensional steady temperature that would result at the base of the seismogenic layer from a horizontal plane source of strength $\bar{Q}$ there. On the bottom abscissal scale the temperatures are shown in degrees centigrade for $\bar{Q}$ = 1 HFU = 41.8 mW/m² (and x_2 = 14 km, $K = 6 \times 10^{-3}$ cal/°C cm s). A useful conversion for frictional heat generation rate is

$$1 \text{ HFU} \equiv 41.8 \text{ mW/m}^2 \cong 1.32 \text{ kbar} \times 1 \text{ cm/yr} \quad (10)$$

As a rule of thumb, reasonable models for the vertical distribution of frictional heating in the seismogenic zone yield a maximum temperature rise of 30–40% of the scale temperature ($\bar{Q}x_2/K$); such temperatures are approached in two or three time constants, typically a few million years.

Similarly, inspection of parts a of Figures 2–5 suggests that the maximum long-term heat flow anomaly $q(y = 0, t = \infty)$ over a narrow strike slip fault is typically 60–80% of the average rate of frictional heating $\bar{Q}$ for reasonable vertical distributions $Q(x)$ in the seismogenic zone. These values, too, are generally approached in a few million years; they fall off by an order of magnitude at horizontal distances of about the thickness of the seismogenic layer. If appreciable frictional heating extends to within a few kilometers of the surface (Figures 2 and 3), a substantial fraction of the anomaly will develop in a few hundred thousand years, and the anomaly will be sharply peaked. For wider fault zones, the peaks of the heat flow curves would be subdued somewhat, but this effect is not important as long as the fault width is small in relation to the thickness of the seismic layer.

A major problem in applying models of an infinitesimally thin strike slip fault to frictional heating lies in determining what fraction of the relative plate motion can reasonably be assigned to a slip zone whose width is small in relation to the thickness of the seismogenic layer. According to *Atwater and Molnar* [1973], the relative right lateral motion between the Pacific and North American plates averaged 4 cm/yr between 10 and 4.5 m.y. ago, and 5.5 cm/yr thereafter. *Graham and Dickinson* [1978] believe that most of the motion was probably concentrated on the San Andreas fault proper for the past 6 m.y. Analysis of geodetic data by *Thatcher* [1979*a*] [see also *Savage and Burford,* 1973] implies that for the last century, localized displacement on the creeping portion of the San Andreas fault in central California probably averaged 3 cm/yr, and *Sieh* [1977] estimates an average localized slip rate of about 3½ to 4 cm/yr over the past 3400 yr in the presently locked portion of the San Andreas fault in the Carrizo Plain at the southern end of the Coast Ranges. At the latitude of the Salton trough in southern California, *Savage et al.* [1979] found that right lateral motion ~5 cm/yr was distributed over a 120-km zone including the San Andreas, San Jacinto, and Elsinore faults during the past 5 yr, and *Thatcher* [1979*b*] found a similar broad region of strain accumulation in southern California over the portion of the San Andreas fault zone that bounds the Mojave Block. These and other observations suggest that the present rate of plate motion is typical of the average over the last 10 m.y., ~5 cm/yr, and that the local slip on the San Andreas fault presently might range downward from perhaps 4 cm/yr in parts of the Coast Ranges to substantially smaller values in southern California.

The disparity between interplate slip and fault slip suggests that the problem of mechanically generated heat flow in the interplate shear zone has two parts: (1) that which can be identified with frictional resistance on a thin fault, and (2) that associated with more broadly distributed inelastic dissipation

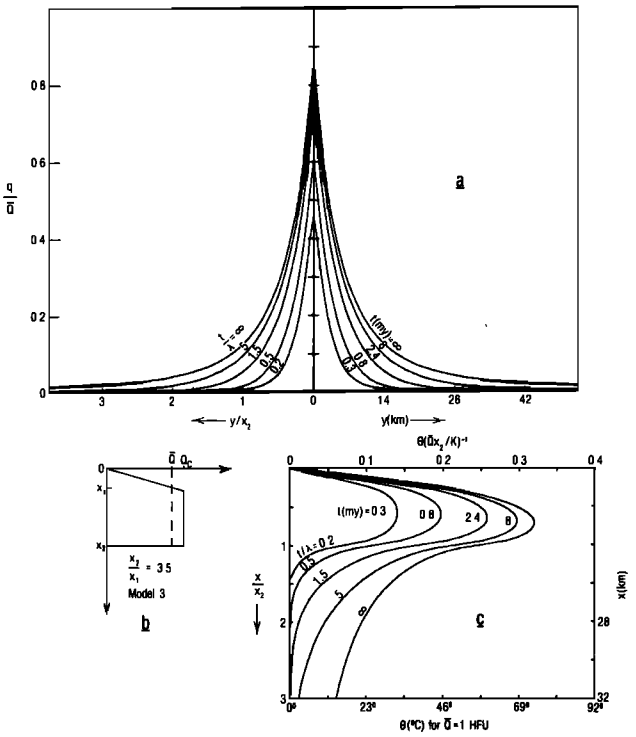

Fig. 5. Surface heat flow q (part a) and fault plane temperature θ (part c) for source strength distribution shown in Figure 5b. Dimensional results are for x_2 = 14 km, K = 6 mcal/cm s °C, and λ = 1.6 m.y.

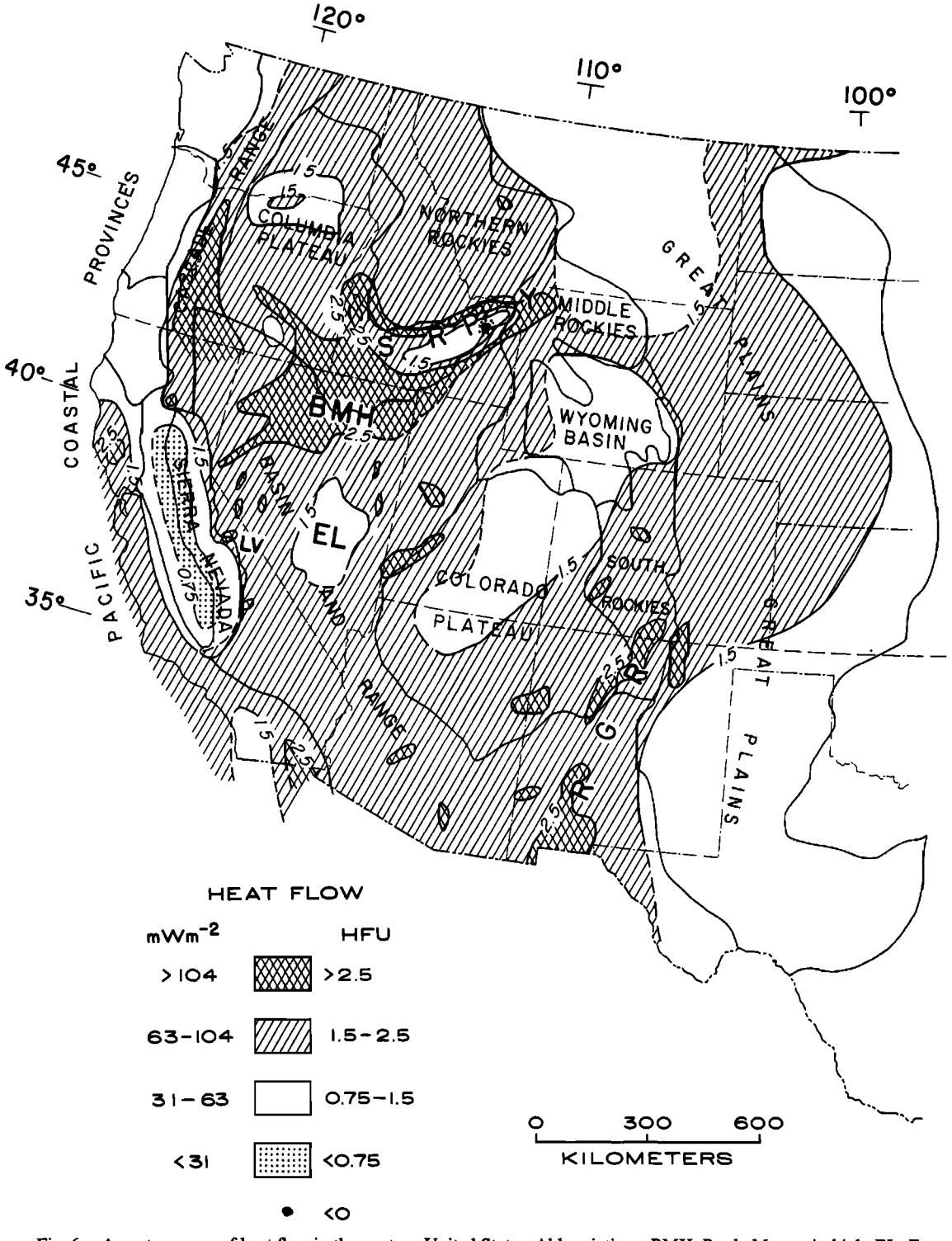

Fig. 6. A contour map of heat flow in the western United States. Abbreviations: BMH, Battle Mountain high; EL, Eureka Low; LV, Long Valley volcanic center; SRP, eastern and central Snake River Plain; Y, Yellowstone thermal area; and RGR, Rio Grande Rift.

in the body of the seismogenic layer or beneath it. If the former is appreciable, it should be associated with a local anomaly over the fault, according to the models we have just presented; the latter may be associated with a broader thermal anomaly [see *Lachenbruch and Sass,* 1973].

Although both parts of the problem will be discussed, at present, we are interested in limits to fault friction implied by local heat flow observations. For this purpose, we shall compare the observed heat flow with a reference model obtained from Figure 2 by selecting fault slip velocities ($2v$) of 2 cm/yr and 4 cm/yr. The linear increase of $Q(x)$ with depth in this model corresponds to a simple frictional law in which the effective normal stress during fault movement is proportional to overburden pressure. We select $\bar{Q} = \pi/2$ HFU so that the reference model yields a convenient maximum heat flow anomaly of 1 HFU (A23*b*), and we shall assume that the depth of

TABLE 1. Summary of Heat Flow and Heat Production Values Near the San Andreas Fault

Designation[1]	Locality	Reference[2]	Latitude	Longitude	Heat Flow		Heat Production	
					HFU	mW/m^2	HGU	μW/m^3
FS-STH	Salton Trough	CO 71	32–48.	115–15.	3.2	134.		
FS-AZ1	ANZA A-1	HW 71	33–30.	116–36.	1.87	78.3	3.6	1.5
FS-AZ2	ANZA A-3	HW 71	33–32.	116–36.	1.76	73.7	2.8	1.2
SB-AZ3	ANZA A-2	HW 71	33–32.	116–48.	1.46	61.1	2.2	0.9
FS-LB1	L.A. Basin LB-1	US 71	33–53.	118–02.	1.74	72.8		
FS-AC1	Santa Ana AC-1	US 71	33–58.	117–38.	1.60	67.0		
MB-YVW	Yucca Valley Water	US 79	34–13.5	116–24.2	1.12	46.9	6.5	2.7
FS-SB2	San Bernardino SB-2	HW 71	34–15.	117–19.	1.63	68.2		
FS-SB3	San Bernardino SB-10	HW 71	34–15.	117–20.	1.58	66.1	3.7	1.5
FS-SB4	San Bernardino SB-5	HW 71	34–16.	117–20.	1.08	45.2		
TR-PSA	Palmdale Stress A	US 79	34–25.6	117–51.8	1.58	66.1	3.8	1.6
TR-PSB	Palmdale Stress B	US 79	34–28.1	117–51.2	1.60	67.0	2.5	1.0
MB-PSC	Palmdale Stress C	US 79	34–33.2	117–42.9	1.51	63.2	3.0	1.3
FS-LH3	Lake Hughes LH-3	HW 71	34–39.	118–29.	1.68	70.3	2.6	1.1
MB-PSD	Palmdale Stress D	US 79	34–39.1	117–50.8	1.57	65.7	4.9	2.1
FS-LH2	Lake Hughes LH-2	HW 71	34–41.	118–26.	1.56	65.3	3.4	1.4
MB-PSE	Palmdale Stress E	US 79	34–43.9	117–41.7	1.64	68.7	6.2	2.6
MB-HVI	Hi Vista	US 79	34–43.9	117–41.7	1.60	67.0	6.2	2.6
FS-LH1	Lake Hughes LH-1	HW 71	34–44.	118–24.	1.72	72.0	8.7	3.6
GF-TE1	Tehachapi Mt. DH-15A	HW 71	34–51.	118–44.	1.48	62.0		
GF-TE2	Tehachapi Mt. DH-70	HW 71	34–52.	118–45.	2.21	92.5		
GF-TE3	Tehachapi Mt. DH-14	HW 71	34–52.	118–45.	2.03	85.0	7.7	3.2
GF-TE4	Tehachapi Mt. DH-43	HW 71	34–53.	118–46.	2.02	84.6	2.1	0.9
GF-TE5	Tejon Ran. DH-43	US 71	34–53.	118–46.	1.83	76.6		
GF-TE6	Tehachapi Mt. DH-65, 67	HW 71	34–56.	118–49.	1.30	54.4	1.1	0.5
GF-TE7	Tejon Ran. DH-61, 65, 67	US 71	34–56.	118–49.	1.36	56.9		
MB-PSF	Palmdale Stress F	US 79	34–56.1	117–45.7	1.64	68.7	5.7	2.4
FE-ML1	Maricopa	US 79	35–04.2	119–26.3	1.93	80.8		
FE-EH1	Elk Hills 382-3G	US 71	35–16.	119–23.	1.26	52.7		
FE-EH2	Elk Hills 343-4G	US 71	35–16.	119–24.	1.12	46.9		
FE-EH3	Elk Hills 344-35S	US 71	35–17.	119–22.	1.20	50.2		
FE-EH4	Elk Hills 372-35R	US 71	35–17.	119–28.	1.30	54.4		
FE-EH5	Elk Hills 326-28R	US 71	35–17.	119–31.	1.26	52.7		
FE-EH6	Elk Hills 385-24Z	US 71	35–18.	119–33.	1.20	50.2		
FE-EH7	Elk Hills 366-24Z	US 71	35–18.	119–34.	1.00	41.9		
FE-TL1	Temblor	US 79	35–21.3	119–49.7	1.45	60.7		
FW-TS1	La Panza TS-1	US 71	35–26.	120–30.	2.21	92.5	5.4	2.3
FE-WB1	West of Bakersfield	BE 47	35–28.	119–45.	1.29	54.0		
FW-HAR	Harmony	US 79	35–29.5	120–58.7	1.80	75.3	2.7	1.1
FW-PAT	Patterson et al.	US 79	35–55.5	121–01.7	2.3	96.	4.1	1.7
FW-PR1	PRC-2	US 79	36–01.9	120–51.6	2.0	84.		
FW-USL	USL1-3	US 79	36–02.9	120–46.6	2.25	94.	2.8	1.2
FW-PR2	PRC-7	US 79	36–03.0	120–48.7	2.0	84.		
FW-PR3	PRC-12	US 79	36–03.9	120–46.0	2.4	100.		
FW-PR4	PRC-19	US 79	36–05.7	120–42.5	2.1	88.		
FW-HT3	Hollister HO-3	HE 68	36–32.	121–40.	1.20	50.2		
FW-HT5	Hollister HO-5	HE 68	36–35.	121–27.	1.90	79.5		
FW-MOP	Monterey	US 79	36–36.3	121–54.9	1.56	65.3	3.8	1.6
FW-STC	Stone Canyon	US 79	36–38.4	121–15.5	1.79	74.9	3.5	1.5
FW-HT1	Hollister HO-1	HW 71	36–43.	121–24.	1.71	71.6	3.4	1.4
FW-HT4	Hollister HO-4	HE 68	36–48.	121–20.	2.30	96.3		
FW-HT6	Hollister HO-6	HE 68	36–50.	121–17.	2.30	96.3		
FW-HT2	Hollister HO-2 & 7	HE 68	36–53.	121–35.	1.70	71.2		
FW-HT7	Hollister HO-8	HE 68	36–55.	120–58.	1.40	58.6		
FE-PT1	Pacheco Tunnel 208	US 79	37–01.6	121–18.7	2.03	85.0	3.1	1.3
FE-PT0	Pacheco Tunnel 210	US 79	37–01.7	121–18.4	2.12	88.7	3.1	1.3
FE-PT9	Pacheco Tunnel 219	US 79	37–02.6	121–15.1	2.14	89.6	3.1	1.3
FE-PT2	Pacheco Tunnel 212	US 79	37–02.8	121–14.2	1.90	79.5	3.1	1.3
FE-PT3	Pacheco Tunnel 213	US 79	37–03.0	121–12.8	2.10	87.9	3.1	1.3
FE-PT6	Pacheco Tunnel 216	US 79	37–03.2	121–11.3	1.60	67.0	3.1	1.3
FE-PT5	Pacheco Tunnel 215	US 79	37–03.3	121–10.8	1.63	68.3	3.1	1.3
FW-BLM	Ben Lomond	US 79	37–06.9	122–09.1	1.61	67.4	2.2	0.9
FE-VCS	Valley Christ. School	US 79	37–14.3	122–04.1	2.15	90.		
FW-BHR	Pescadero BHR-1	US 79	37–14.7	122–23.7	2.53	105.9	4.6	1.9
FE-PRM	Permanente	US 71	37–19.	122–07.	2.20	92.1		
FE-SE1	Sunnyvale C-3	US 71	37–27.	122–02.	2.02	84.6		
FE-MP1	Melno Park MP-1	US 68	37–27.	122–10.	2.16	90.4		
FE-DM1	Dumbarton S.F. Bay	US 71	37–29.	122–08.	2.25	94.2		
FE-DE1	Dumbarton Earthquake 1	US 79	37–30.6	122–07.8	2.03	85.0		
FE-RCE	Redwood City Exp.	US 79	37–30.8	122–12.5	1.85	77.		
FE-MSL	May School	US 79	37–44.3	121–45.2	1.52	63.6	3.2	1.3

TABLE 1. (continued)

Designation[1]	Locality	Reference[2]	Latitude	Longitude	Heat Flow HFU	Heat Flow mW/m²	Heat Production HGU	Heat Production μW/m³
FE-TR1	Tracy DH-2	US 71	37–48.	121–35.	0.96	40.2		
FE-DA1	Danville	US 79	37–48.1	121–56.5	1.28	53.		
FE-MST	Berkeley MSTW	US 71	37–52.	122–15.	2.00	83.7		
FE-NIC	Nicasio	US 79	38–05.5	122–44.9	1.84	77.0	2.9	1.2
FW-PTR	Point Reyes	US 79	38–05.7	122–53.5	1.91	80.0	5.0	2.1
FE-SEA	Sea Ranch	US 79	38–42.0	123–25.1	2.2	92.		
FE-ANP	Annapolis	US 79	38–43.1	123–20.8	2.16	90.		
FE-CL1	Cloverdale	US 79	38–46.	122–58.	3.50	146.5	0.2	0.1
FE-GYS	3 Holes at the Geysers	US 79	38–48.	122–50.	10.00	418.6		
FE-GUI	Guinda	US 79	38–50.4	122–12.0	0.90	37.7		
FE-COL	Colusa Basin	US 79	38–53.0	121–53.7	0.80	33.5		
FW-PTA	Pt. Arena	US 79	38–55.7	123–42.6	1.44	60.3		
FE-BVL	Booneville	US 79	38–59.6	123–20.8	1.27	53.		
FE-UKI	Ukiah	US 79	39–03.4	123–09.1	1.78	74.		
FE-PVY	Potter Valley	US 79	39–20.4	123–06.1	1.8	76.		
FE-NOY	Noyo Hill	US 79	39–24.5	123–44.8	1.8	75.		
FE-WIL	Willitts EC-1	US 71	39–34.	123–07.	1.85	77.4		
CR-EG7	Cottonwood Glade EG-7	US 71	39–42.	122–48.	1.20	50.2	2.8	1.2
CR-EG8	Cold Creek EG-8	US 71	39–42.	122–53.	1.50	62.8	2.4	1.0
FE-LYN	Laytonville	US 79	39–43.8	123–30.1	1.42	60.		
FE-CLN	Covelo North	US 79	39–50.1	123–09.9	1.40	59.		
FE-LMR	Lake Mtn. Ranch	US 79	39–56.8	123–21.1	0.66	28		
FE-SCV	Shelter Cove	US 79	40–01.3	124–04.0	1.39	58.		
FE-GBL	Garberville	US 79	40–05.5	123–48.0	1.03	43.		
FE-EBG	Ettersburg	US 79	40–08.1	124–00.0	1.04	43.		
FE-KET	Kettenpom	US 79	40–08.3	123–24.6	1.2	50.		
FE-FTS	Fort Seward	US 79	40–13.0	123–38.4	1.44	60.		
FE-HON	Honeydew	US 79	40–14.4	124–07.6	1.8	75.		
FE-PRA	Petrolia	US 79	40–19.4	124–16.5	1.82	76.		
FE-GZB	Grizzly Bluff	US 79	40–32.8	124–10.6	1.31	55.		
FE-NOS	Nav. Ocean. Sta.	US 79	40–33.8	124–21.2	0.82	34.		
FE-EUR	Eureka B-69	US 79	40–43.6	124–12.8	0.83	34.7		
FE-KSM	King Salmon	US 79	40–44.4	124–12.8	0.92	38.		
FE-BLK	Blue Lake	US 79	40–52.6	123–58.8	1.18	49.		

[1]Subregions: FS, Fault South; SB, Southern California Batholith; MB, Mojave Block; TR, Transverse Ranges; GF, Garlock Fault; FE, Fault East; FW, Fault West; CR, Coast Ranges.

[2]CO 71, *Combs* [1971]; HW 71, *Henyey and Wasserburg* [1971]; US 71, *Sass et al.* [1971]; US 79, present paper; BE 47, *Benfield* [1947]; HE 68, *Henyey* [1968]; US 68, *Sass et al.* [1968].

the seismogenic layer (x_2) is 14 km. The reference model therefore represents the following conditions:

$$q = 1 \text{ HFU} = 41.8 \text{ mW/m}^2 \qquad y = 0 \qquad t = \infty \tag{11a}$$

$$\bar{Q}/2v \equiv \tau_{avg} \cong 518 \text{ bars} \qquad 2v = 4 \text{ cm/yr} \tag{11b}$$

$$\cong 1035 \text{ bars} \qquad 2v = 2 \text{ cm/yr} \tag{11c}$$

The scale temperature for use in Figure 2*c* is

$$\bar{Q}x_2/K = 365°\text{C} \tag{12a}$$

and the total rate of heat production per unit length of fault is

$$\bar{Q}x_2 = 2.2 \text{ cal/cm s} \tag{12b}$$

$$= 0.92 \text{ Mw/km} \tag{12c}$$

According to these results, if the average slip velocity were 2–4 cm/yr, we should expect to see a local heat flow anomaly of 1.0–0.2 HFU over the fault trace for each 100 bars of frictional resistance, unless the fault trace were very young or the frictional heat had been removed or redistributed by hydrologic processes. In the next two sections, we shall examine the data on heat flow and thermal springs in an attempt to obtain a limit to frictional resitance from this point of view.

HEAT FLOW

The status of published heat flow measurements in the western United States as of late 1979 [*Sass et al.*, 1980] is illustrated in Figure 6. The western United States is characterized generally by high and variable heat flow, although it also contains large areas of low-to-normal heat flow. High heat flow in regions of extensional tectonics like the Basin and Range province can be accounted for by the upward mass flow required for plausible rates of lithosphere extension [*Lachenbruch and Sass*, 1978; *Lachenbruch*, 1978]. Some zones of low heat flow like the continental margin of the Pacific Northwest may be related to heat sinks associated with subduction; others, like the 'Eureka Low' (EL, Figure 6), may be related to systematic regional hydrologic phenomena [*Lachenbruch and Sass*, 1977].

The part of the California Coastal region associated with the transform boundary between the North American and Pacific plates has a range of heat flows typical of most other parts of the western United States (Figure 6). This includes measurements offshore in the Southern California Borderland [*Lee and Henyey*, 1975].

In this paper, we shall examine a data set (Table 1, Figure 7) that includes: the first heat flow determination in California (WB1, Table 1, *Benfield* [1947]), subsequent measurements by *Combs* [1971], *Henyey* [1968], *Henyey and Wasserburg* [1971], *Sass et al.* [1971], *Roy et al.* [1972], USGS data, which until now have received only preliminary mention in the literature [*Lachenbruch and Sass*, 1973, 1977, 1978], and results from some recent drilling in the Northern California Coast Ranges.

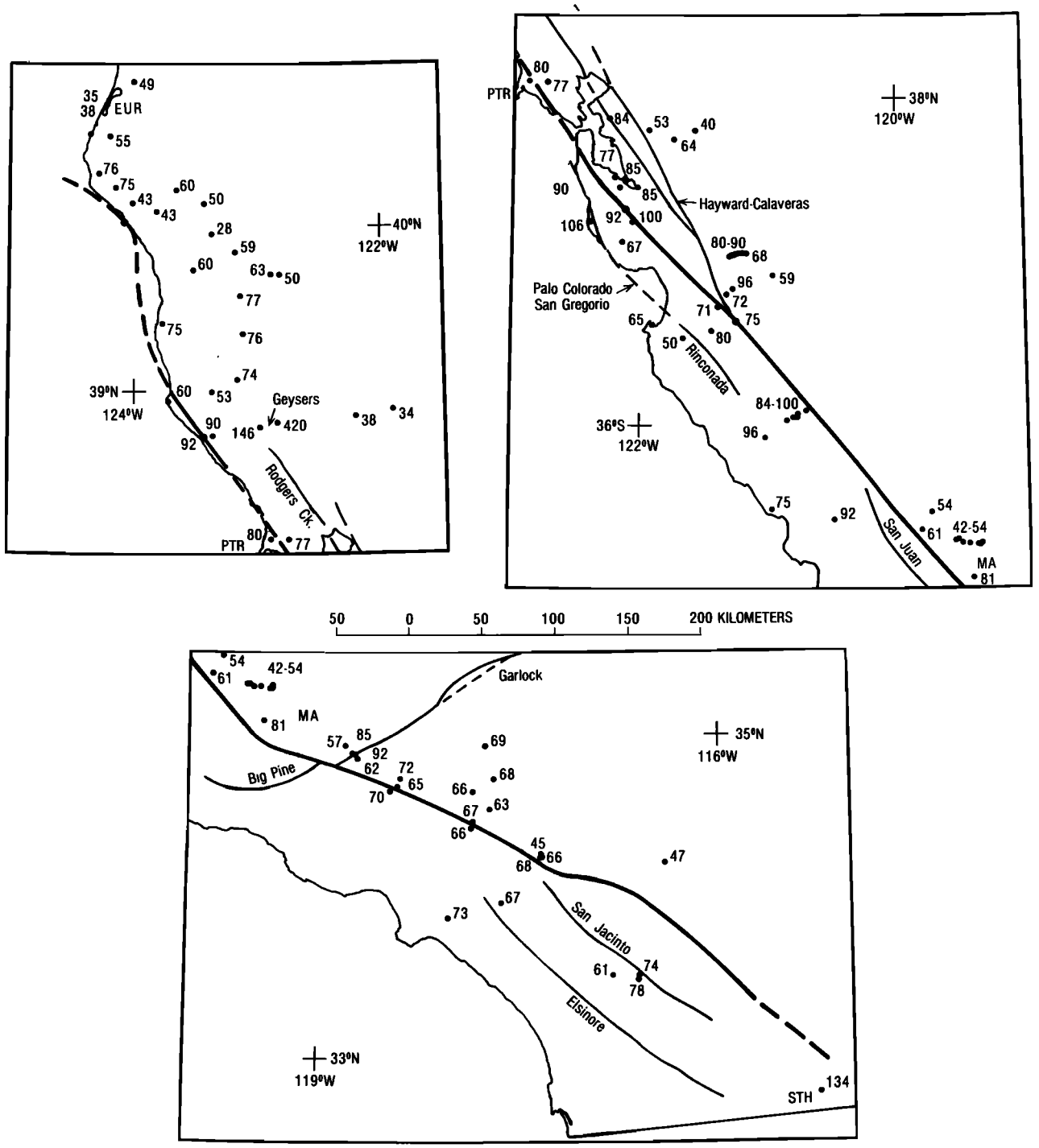

Fig. 7. Heat flow (mW/m^2) in relation to major recently or currently active strike slip faults in California: *a*, Eureka (EUR) to Point Reyes (PTR); *b*, Point Reyes to Maricopa (MA); *c*, Maricopa to Salton Trough hydrothermal areas (STH) (1 HFU = 41.8 mW/m^2).

Data from the latter two categories (designated 'US 79' in Table 1) should be considered preliminary and are subject to revision after more detailed study. Several heat flow determinations within a small area of the Salton Trough [*Combs*, 1971] have been averaged and are represented as a single point (STH) in Table 1 and the various illustrations. The entire data set is composed of 106 independent determinations at 103 distinct sites (Table 1, Figure 7) over a broad (~100 km wide) area including the main trace of the San Andreas fault. For most of our statistical analyses, we have excluded data from north of Cape Mendocino (region 1a, Figure 8), the Great Central Valley (EH1 through EH7, MSL, TR1, DA1, HT7, WB1, GUI, and COL, Table 1), the Geysers region (GYS and CL1, Table 1), and the Salton Sea Area (STH, Table 1), leaving a core of 81 heat flow determinations from the Northern and Central Coast Ranges, the Transverse Ranges, and the southern part of the San Andreas fault zone. Sites more than 100 km from the fault zone in the California borderland [*Lee and Henyey*, 1975] and the Mojave Block [*Lachenbruch et al.*, 1978] were omitted from our analysis.

Heat flow values are shown in relation to the San Andreas and other recently or currently active fault zones in Figure 7. In Figure 8, the locations of all sites are illustrated in relation to the main trace of the San Andreas fault and to a number of subregions to be discussed below. The core of 81 'fault zone' determinations form the basis for Figures 9, 11, and 12 and the associated statistical analyses.

The histogram of Figure 9 indicates a nearly normal distribution of heat flow, with a mean of 1.75 ± 0.04 HFU (72 ± 2 mW m^{-2}), significantly lower than the Basin and Range mean of 2.1 HFU [*Lachenbruch and Sass,* 1977, 1978] but comparable to the mean of 70 values for the Southern California Borderland discussed by *Lee and Henyey* [1975]. An examination of the heat flow—heat production data (Figure 10) suggests that despite a large amount of scatter, the mean 'reduced' heat flow q_r may be comparable to that from the Basin and Range province [see Figure 9-3, *Lachenbruch and Sass,* 1978]. However, there is evidently no linear relation between heat flow and heat production, as is found farther east in the Sierra Nevada batholith.

The heat flow as a function of distance normal to the fault is shown for the 81 data of Figure 9 in Figure 11. Shown also is the pattern of curves representing the reference anomaly discussed in the last section. As in Figure 2, the top curve represents the steady state, and the transient curves represent conditions at 8 m.y., 2.4 m.y., 0.8 m.y., and 0.3 m.y. after the start of faulting. It is seen from Figure 11 that even the steady state anomaly (representing a frictional resistance of 1 kbar for $2v$ = 2 cm/yr or 0.5 kbar for $2v$ = 4 cm/yr) might go almost undetected in such widely scattered data. However, Figure 11 obscures a certain amount of systematic variation. This can be seen from Figure 12 in which the heat flows are projected perpendicularly onto the San Andreas fault and plotted as a function of distance from Cape Mendocino along the fault trace to a distance of 1000 km, where the surface expression of the fault disappears in the vicinity of the Salton Sea. The profile of Figure 12 has been divided somewhat arbitrarily into subregions (see Figure 8 and Table 2) for the purpose of discussion. Although Figure 12 has a great deal of scatter, it shows that north of the Mendocino Triple Junction, where the San Andreas fault does not exist (region 1a), the average heat flow is low, about 1 HFU. Southward from the Triple Junction, the heat flow seems to increase over a distance of about 200 km (regions 1b and 2) to average values close to 2 HFU, characteristic of the remaining 550 km of the California Coast Ranges (regions 3–6). Heat flow is significantly lower (~1.6 HFU) farther south along the 150-km fault segment that bounds the Mojave Block (region 7). South of region 7, data are inadequate to indicate the relation of heat flow to the fault; however, the few data available are included in Figure 12. The high values from STH near the Salton Trough and CL1 near the Geysers are shown in Figure 12 for reference.

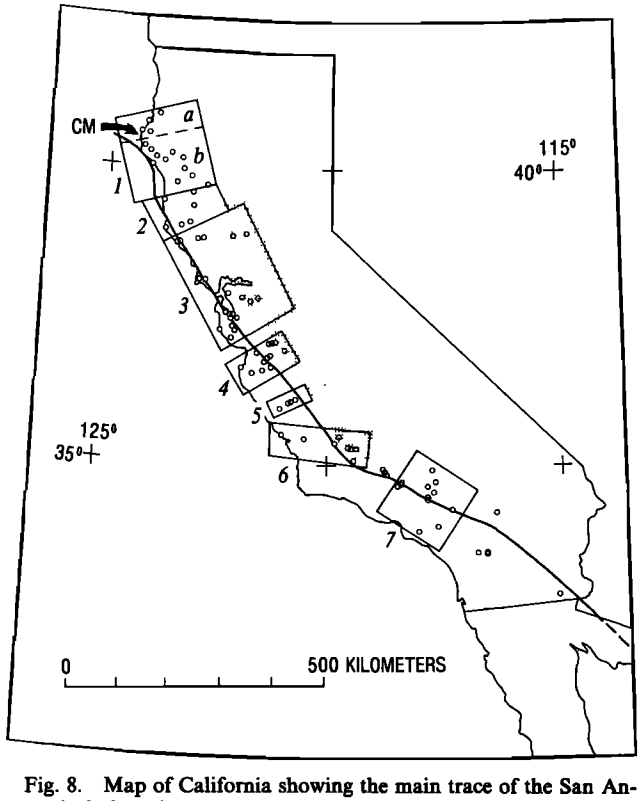

Fig. 8. Map of California showing the main trace of the San Andreas fault, heat flow control, and the regions depicted in Figures 13–19. Stippled area indicates the approximate extent of the Great Central Valley.

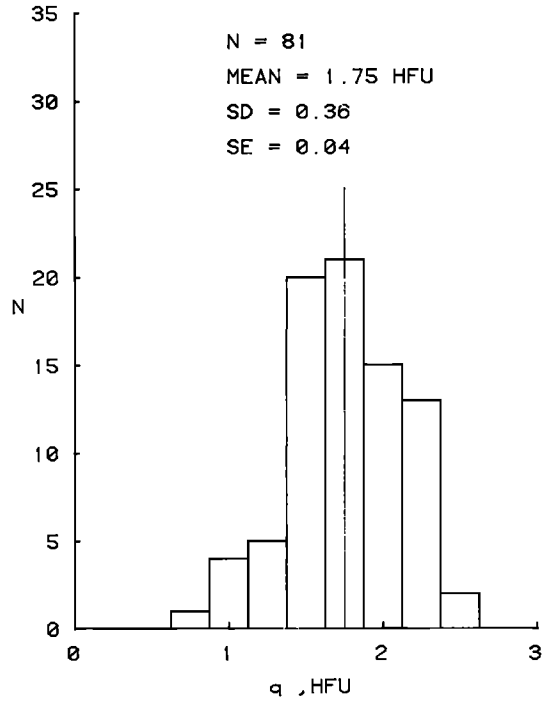

Fig. 9. Histogram of 81 values of heat flow in the San Andreas fault zone (Figures 7 and 8) (excluding hydrothermal areas, STH, GYS, CL1, Table 1, and data from the Great Valley and north of Cape Mendocino (region 1b)).

In Figures 13–19, heat flow in each of the seven regions (Figure 8) is shown (with the reference anomaly) as a function of distance from the fault trace. A casual inspection of the individual profiles reveals that there is no evidence for a thermal anomaly due to local frictional heating at any latitude; if such heating does occur, its magnitude must be much smaller ($\ll$1 HFU) than that represented by the reference anomaly. Attempting to decide just how much local heating at the fault trace could go undetected in an individual profile probably is more a matter for judgment than for statistics because of the uneven areal coverage, the variability from site to site in the quality of temperature and thermal conductivity data, and such locally variable conditions as hole depth, structure, hy-

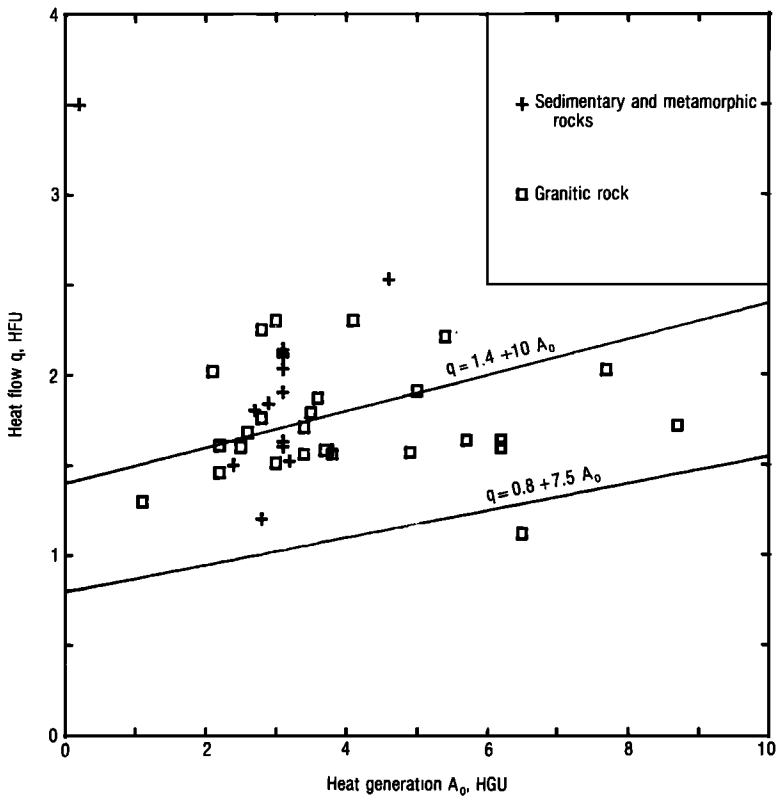

Fig. 10. Heat flow versus near-surface heat production for the San Andreas fault zone. Reference curves are for Basin and Range province (upper) and eastern United States (lower) [*Roy et al.*, 1968].

drology, and microclimate. Making allowance for some of these details, we judge that a local anomaly greater than 0.2 HFU is probably precluded in the Coast Ranges. Scaling from our steady state reference anomaly, this would imply a maximum frictional resistance of 50–70 bars assuming the present-day rate of fault slip of 3–4 cm/yr; allowing a bit for disequilibrium and finite fault width, a figure of ~100 bars would seem reasonable.

Some numerical support for a figure of this magnitude can be obtained if we consider the 39 heat flow determinations used to calculate means for regions 3–6 (Figure 12), the portion of the Coast Ranges in which the fault zone has probably been in existence on both plates for several million years. It is seen from these data (Figures 20*a* and 20*b*) that the difference between the mean heat flow within 10 km of the fault (Figure 20*a*) and beyond 10 km from the fault (Figure 20*b*) is quite insignificant (0.01 HFU). According to a two-sample T test for this data set, the mean heat flow within 10 km of the fault differs from the mean heat flow beyond 10 km from the fault by less than 0.2 HFU at the 95% confidence limit.

The remarkably uniform values in the Mojave segment of the fault (region 7, Figure 19) deserve special comment. (Following *Henyey* [1968] and *Henyey and Wasserburg* [1971], we exclude the single low value, SB4, Table 1, because of suspected hydrologic disturbances.) The total range is 1.51–1.74 HFU, and the means and standard deviations (Table 2, Figures 20*c* and 20*d*) are indistinguishable between data sets obtained within and beyond 10 km from the fault. In this region, the two-sample T test yields a difference in mean heat flows within and beyond 10 km from the fault of less than 0.08 HFU at the 95% confidence limit. Although it is risky to attach such precision to any heat flow measurements, the consistency of the data suggests that a local anomaly does not exist even at the 0.1 HFU level. However, this is the region in which *Thatcher* [1979*b*] found geodetic evidence for a broad shear zone, and the local slip velocity may well be only 2 cm/yr or less. Furthermore, the tectonics of the region suggests that the main fault trace could have shifted position in the last few million years. Hence even at this location, the thermal effects of frictional resistance as large as 100 bars might possibly go undetected.

The horizontal lines denoting mean heat flow values in regions 3, 4, and 6 (Figures 15, 16, and 18) terminate between the easternmost drainage divide of the Coast Ranges and the Central Valley. As in the case of heat flow north of the San Andreas fault zone (i.e., north of Cape Mendocino, Figure 12), the values to its east in the Great Valley fall off abruptly. (For discussion, see *Lachenbruch and Sass* [1973].)

In summary, the California Coast Ranges represent a region of generally high but variable heat flow enclosing the landward portion of the San Andreas fault zone. There is no evidence that the heat flow is greater near the fault trace than in the surrounding terranes over a 1000-km distance along the fault trace southward from Cape Mendocino. With reasonable assumptions for fault slip rate and age and assuming conduction is the only mode of heat transfer, this result suggests that the average dissipative resistance to motion on the fault does not exceed ~100 bars. The result supports conclusions from earlier studies [*Henyey*, 1968; *Henyey and Wasserburg*, 1971; *Brune et al.*, 1969; *Lachenbruch and Sass*, 1973]. We shall return to the problem of the broad Coast Range anomaly later; in the next section, we shall investigate the possi-

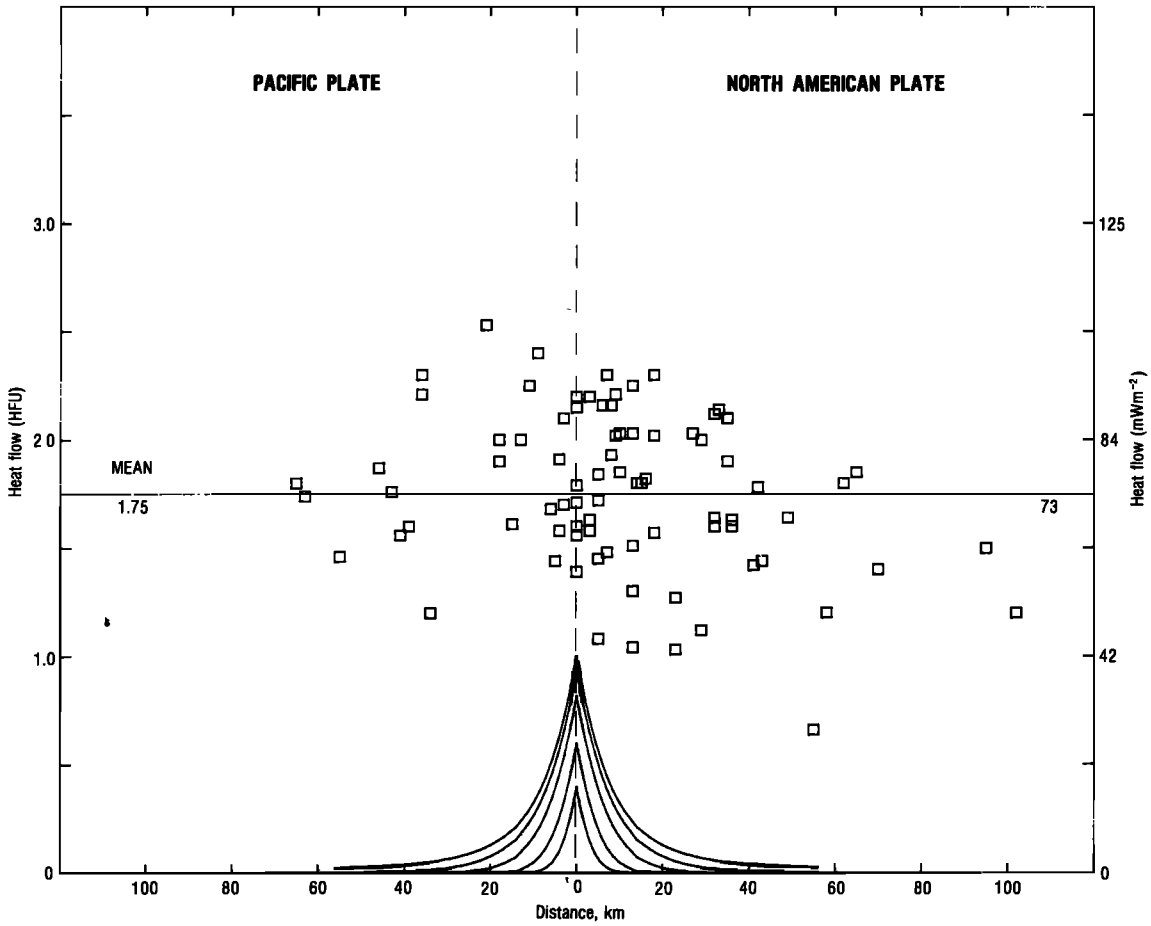

Fig. 11. Heat flow as a function of the distance from the main fault trace for 81 points of Figure 9. Pattern of curves is reference anomaly from Figure 2*a* (see (11) and (12)).

bility that appreciable amounts of frictional heat might have been generated and subsequently removed by hydrologic processes.

Hydrologic Transport and the Constraint on Frictional Heating

We have seen that if heat transfer in the fault zone has been predominantly by conduction, then the absence of a peaked heat flow anomaly suggests that the average stress allocated to frictional heating on the fault is small ($\lesssim$100 bars). If, however, substantial amounts of frictional heat were transferred convectively by moving ground water, much larger frictional stresses would be permissible. There are two possibilities for removal of the hypothetical undetected frictional heat: (1) it was discharged at the surface by thermal springs, or (2) it was redistributed uniformly over a broad zone (~100 km wide) by some unspecified hydrologic process.

Discharge by Thermal Springs

In attempting to reconcile the apparent lack of a peaked heat flow anomaly near the San Andreas fault with laboratory evidence for high mean shear stress (~1 kbar), some workers [e.g., *Hanks,* 1977; *Scholz et al.,* 1979] have suggested that the San Andreas fault zone is analogous to mid-ocean ridges, where the expected conductive heat flow anomaly is literally washed out by convection of seawater within permeable rocks. By this analogy, the heat generated by friction along the fault zone is removed by water flowing through relatively permeable rocks, and it is discharged by hot springs.

The distribution of thermal springs (those with a discharge temperature >15°F above mean annual air temperature) is shown in Figure 21 (modified from Figure 8 of *Waring* [1965]). Along the main trace of the fault, spring activity is very rare [see also *Jennings,* 1975]. Within the Coast, Transverse, and Peninsular Ranges, there is a scattering of thermal springs, but apart from those clearly associated with the Geysers geothermal zone north of San Francisco, their temperatures are not high, and their flow rates are small, typically of the order of 50 l/min or less. Many of the springs in southern California occur close to currently or recently active strike slip faults (for example, Elsinore, San Juan, Garlock, San Jacinto) [*Jennings,* 1975], but north of the San Bernardino Mountains (i.e., north of the southern limit of region 7, Figures 8 and 11), no thermal springs are reported precisely on the main trace of the San Andreas fault.

In Table 3 we have compiled data from all of the thermal springs that we could find described in the literature that lie within 10 km of the 950-km length of the San Andreas fault trace between Cape Mendocino and the southwest boundary of region 7 [*Waring,* 1965; *Renner et al.,* 1975; *Brook et al.,* 1979; *Sammel,* 1979]. The total convective discharge over this distance is 1.25 MW, 80% of which is contributed by a spring at the southern edge of the region (Table 3). The reference anomaly of the last section, which corresponds to a frictional

TABLE 2. Mean Heat Flows, Standard Deviations, and Standard Errors for the Regions Illustrated in Figures 8 and 13–19

Region	Number of Data*	Mean Heat Flow $\bar{q}$, HFU	Standard Deviation, HFU	Standard Error, HFU
1	17	1.23	0.33	0.11
1a	5	1.01	0.22	0.10
1b	12	1.32	0.33	0.09
2	6	1.66	0.24	0.10
3	14	2.06	0.22	0.06
4	15	1.87	0.31	0.08
5	6	2.17	0.17	0.07
6	4	1.85	0.32	0.16
7	15	1.58	0.15	0.04
	14†	1.62	0.06	0.02

*Excluding sites in the Great Valley, stippled, Figure 8.
†Excluding site SB4 (see text).

resistance of 500–1000 bars (depending on slip velocity), represents the generation of almost 1 MW of frictional heat per kilometer of fault length (13*b*). Hence if such stresses had been operative, hydrologic convection would have had to remove heat at the rate of almost 1 MW/km to account for the absence of a local heat flow anomaly at the fault. Stated another way, heat discharged convectively by the thermal springs could be generated on the fault by ~1 bar of frictional resistance. Allowing an order of magnitude increase for anomalously large conductive flux adjacent to the springs [see, e.g., *Olmsted et al.*, 1975], discharge by the spring systems still would not significantly affect our estimated limits of frictional stress based on conduction theory. Furthermore, since the distribution of springs does not indicate a concentration of activity on the San Andreas fault trace, there is no particular reasons to suppose that the fault is the source of their heat.

The possibility remains that the heat was flushed out in transient pulses immediately following unstable local heating of ground water during individual earthquakes. However, this should lead to conspicuous surface activity on a scale not generally observed, and the model leaves unexplained the absence of a local heat flow anomaly over creeping portions of the fault.

Lateral Redistribution of Heat by Hydrologic Circulation

If we take the broad heat flow anomaly in the Coast Range to be 0.8 HFU over a width of 84 km (6 times the depth of the seismogenic layer), the anomalous heat loss would be equivalent to the heat generated locally by 2 kbar of frictional stress on a fault with a slip velocity of 3 cm/yr. A similar result applies in southern California (region 7), where the regional anomaly is probably broader but less intense (~0.4 HFU?) [see also *O'Neil and Hanks*, 1980]. Thus the thermal budget would not be violated by very large frictional stresses if a mechanism existed to redistribute the frictional heat broadly and uniformly.

Thermally driven hydrologic convection is not a likely candidate. The absence of thermal springs suggests that models of thermally driven hydrologic convection should have a no-mass-flow boundary condition. In that case, hydrothermal circulation driven by the buoyancy of water heated on a vertical fault plain would generally result in an increase (not a decrease) of near-surface conductive flux near the fault trace. Further evidence against thermally driven convection comes from a recent study by *Murata et al.* [1979], who conclude that 'the presence of disordered cristobalite in shale adjacent to the San Andreas fault suggests that movements along the fault have not induced a sustained rise in temperatue of even a few degrees in the shale.'

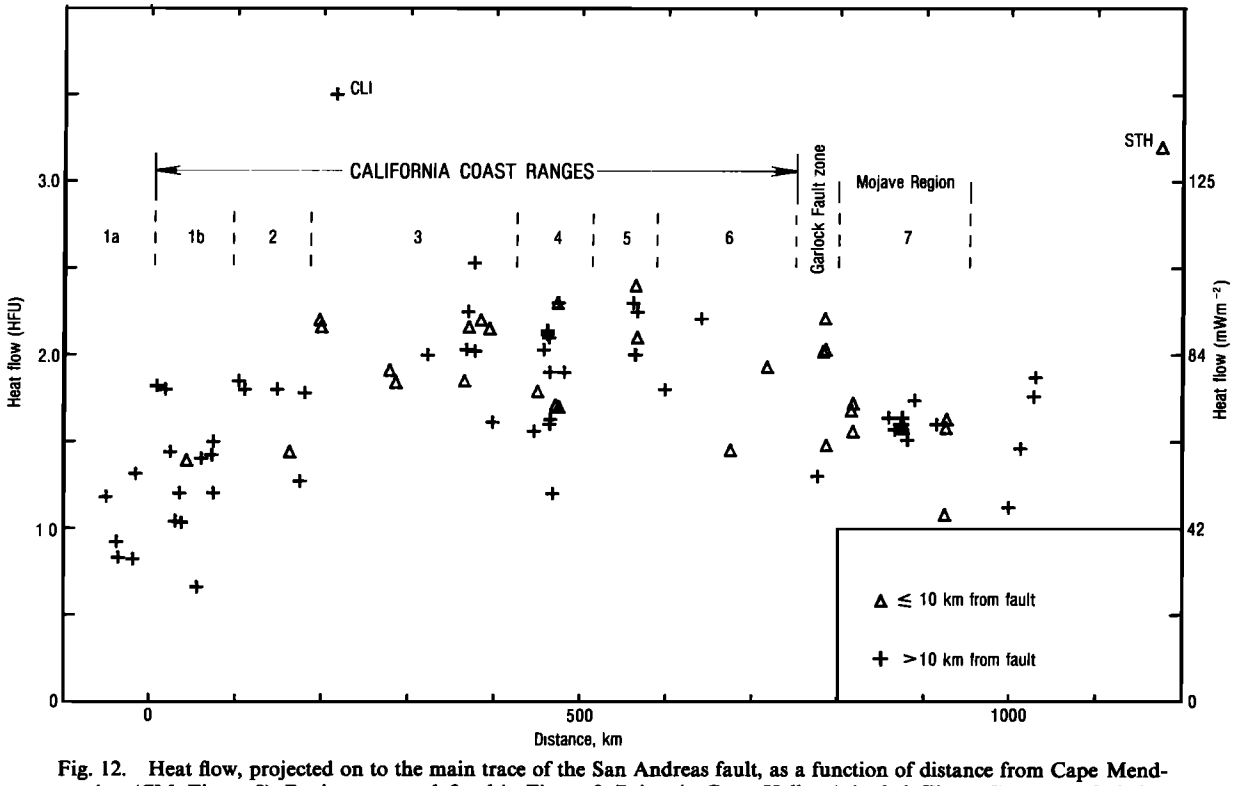

Fig. 12. Heat flow, projected on to the main trace of the San Andreas fault, as a function of distance from Cape Mendocino (CM, Figure 8). Regions are as defined in Figure 8. Points in Great Valley (stippled, Figure 8) were excluded.

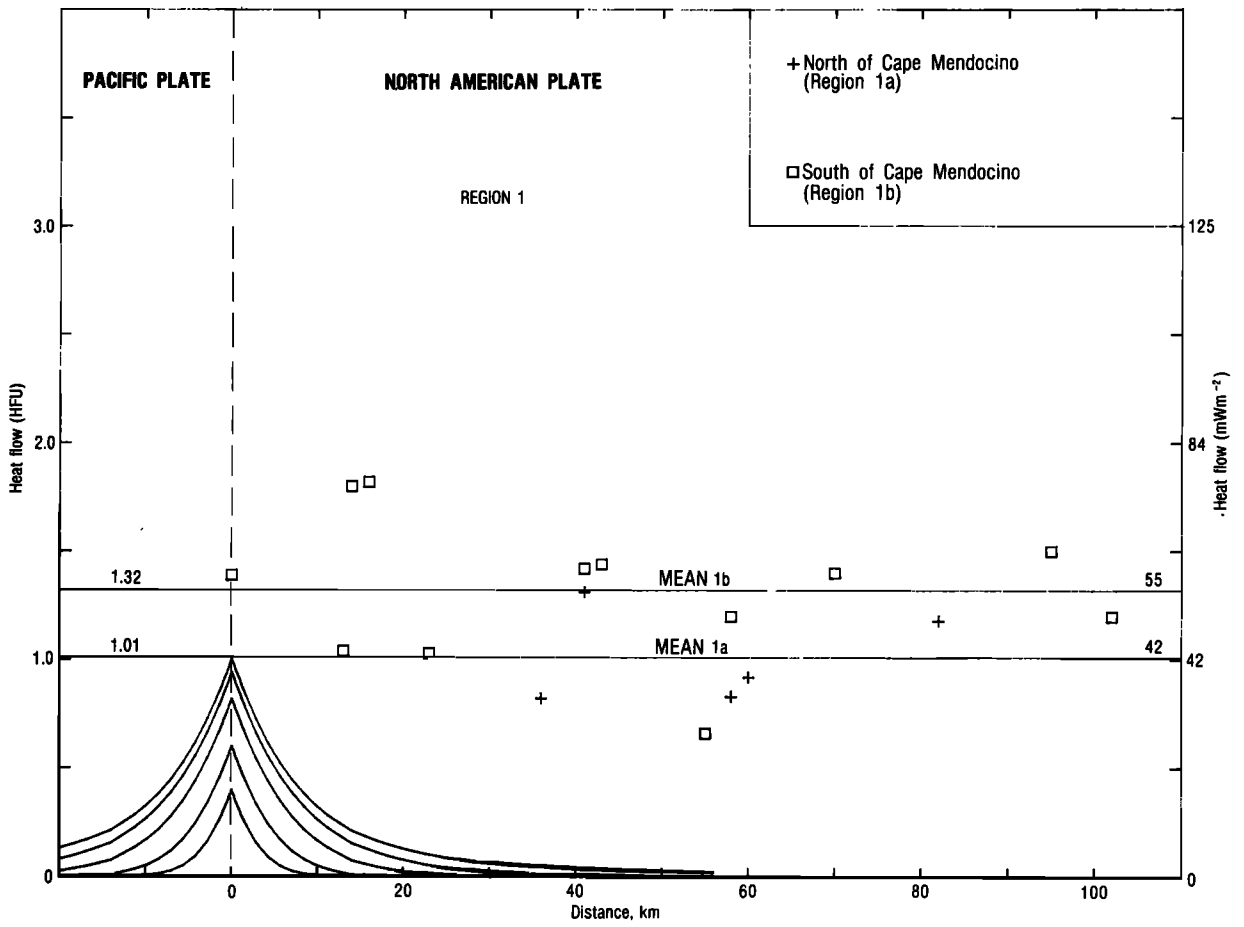

Fig. 13. Heat flow versus distance from the main trace of the San Andreas fault, region 1 (Figure 8), shown with reference anomaly. Horizontal lines show means for region 1a (north of Cape Mendocino) and region 1b (south of Cape Mendocino).

Any mechanism devised to account for a broad uniform redistribution of frictional heat by water movement must contend with the observation that on opposite sides of the fault the heat flows are similar, but the hydrologic regimes probably contrast sharply. In the Coast Ranges the San Andreas fault is bounded on the east by metamorphic and sedimentary rocks of the Franciscan formation and Great Valley sequence, which according to *Berry* [1973] are characterized by superhydrostatic pore pressures, approaching lithostatic in many places. On the west the fault is bounded by the Salinian Block, a fractured granitic terrain that probably has an open (hydrostatic) hydrologic regime [I. Barnes, personal communication, 1979; see also *Brace,* 1980]. It is difficult for us to imagine a hydrologic system that might transport heat to both the east and the west for distances of tens of kilometers in such a way as to produce similar heat flows in such contrasting terrains.

O'Neil and Hanks [1980] cite depletion of hydrogen and oxygen isotopes in a narrow band of granitic rocks adjacent to the San Andreas fault as evidence for profound water circulation in the fault zone. It is known that such depletion can result from interactions with ground water, which must penetrate to depths ~10 km to replace water heated during the cooling of a pluton [e.g., *Taylor,* 1978]. Since the origin of the granitic rocks predates the origin of the San Andreas fault (~20 m.y. B.P.) by about 50 m.y., however, it is not clear that the observed isotope depletion is associated with the fault. O'Neil and Hanks estimate that the isotope exchange in this anomalous band probably took place in the temperature range ~100–200°C, temperatures that obtain today in the depth range ~3–6 km. In the absence of pervasive surface hydrothermal activity, for which there is no evidence today, the surface from which their samples were obtained must have undergone 3–6 km of erosion since the isotope exchange took place. It follows that unless erosion of at least 3–6 km occurred at all of their sample sites during the last 20 m.y. or so, the water circulation responsible for the anomaly probably predated the fault and is unrelated to it. If such erosion did occur, it still does not necessarily imply that the anomaly is related to the fault; it could be the result of differential uplift and erosion near the fault, exposing a preexisting anomalous condition that was a function of depth. In any case, the evidence for isotope depletion occurs only on the west side of the fault and does not resolve the question of why heat flow is high on both sides in spite of the contrasting hydrologic characteristics.

In summary, the similarity of heat flow values and the contrast in hydrologic regimes on either side of the San Andreas fault, taken with the absence of appreciable convective heat discharge by springs in the vicinity of the fault make it extremely difficult to attribute the absence of local high heat flow to hydrologic transport in the fault zone. However, substantial undetected discharge at temperatures slightly above ambient is a possibility in almost any terrain, and more com-

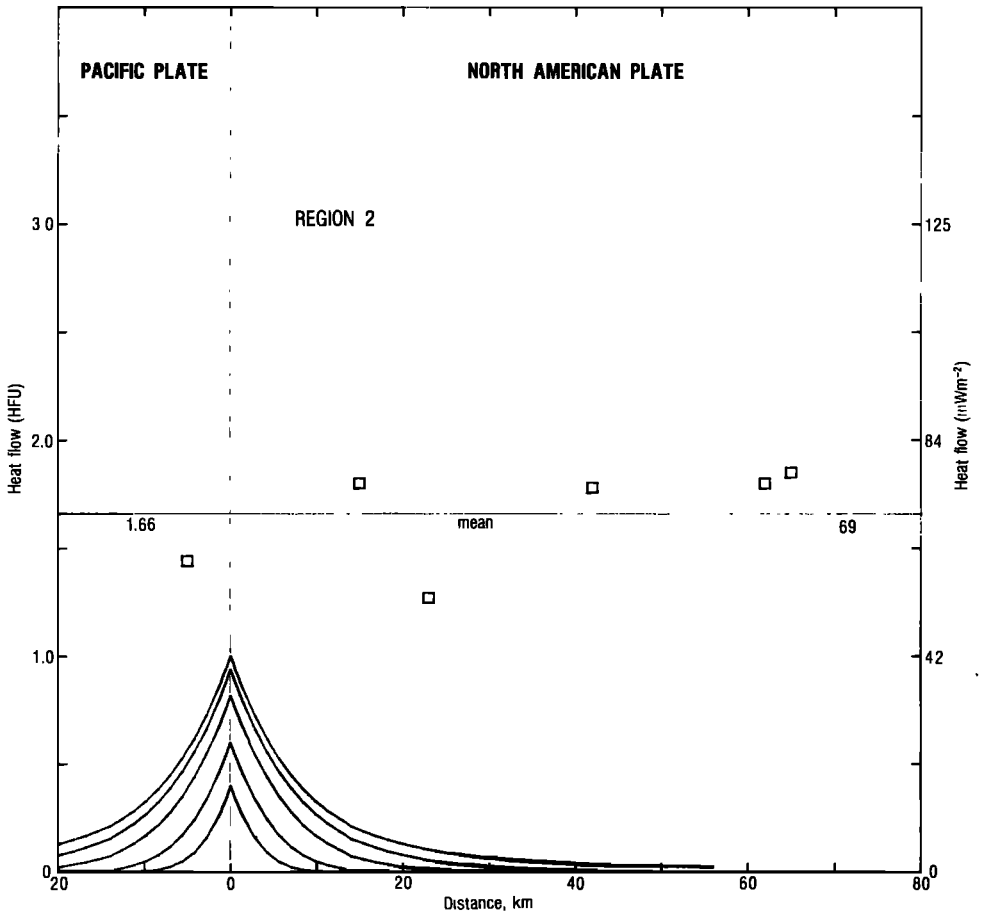

Fig. 14. Heat flow versus distance from the main trace of the San Andreas fault, region 2 (Figure 8), shown with reference anomaly.

prehensive studies of the hydrothermal budget of the fault zone may be worthwhile.

Implications of Uniform Heat Flow, Frictional Strength, and Seismic Constraints for Tectonic Stress

The foregoing discussion suggests that the average frictional resistance during strike slip motion in the seismogenic layer of the San Andreas fault does not exceed ~100 bars; it could, of course, be much less. To avoid a problem in notation (because we shall discuss several types of averages), we express this condition generally as

$$\text{average dissipative resistance} \lesssim 100 \text{ bars} = 10 \text{ MPa} \qquad (13)$$

Since this upper limit is an order of magnitude lower than the dynamic friction that one would expect from the most obvious extension of laboratory results to faults, (13) suggests that special conditions must prevail on the faults to account for their unexpected weakness. In the following section, we consider this 'strength paradox' in terms of generalized results from laboratory experiments on rock friction. It is followed by a section in which we consider additional constraints on fault stress imposed by seismic observations.

Rock Friction, Fluid Pressure, and Tectonic Stress State

We shall consider the relation between the heat flow constraint and rock friction in terms of parameters for the simplest frictional model, described as follows:

$$\tau_m = \mu \sigma_n' \qquad (14a)$$

$$\sigma_n' = \sigma_n - P \qquad (14b)$$

$$R = \mu_k \sigma_n' \qquad (15a)$$

$$= \frac{\mu_k}{\mu} \tau_m \lesssim \tau_m \qquad (15b)$$

The symbol $\bar{R}$ used previously is related to R and total fault slip u by

$$\bar{R} = \frac{1}{u} \int_0^u R \, du \qquad (15c)$$

The maximum stress (or 'frictional strength') that can be sustained by a fractured surface on which the normal stress is σ_n is denoted by τ_m, pore fluid pressure is P, and effective normal stress is σ_n'. The coefficient of (static) friction is the experimentally determined parameter μ. R is the instantaneous dissipative resisting stress (or dynamic friction) operating on the sliding surface while motion is in progress. The coefficient of dynamic friction is the parameter μ_k (15). Although the experimental basis for (15) is quite uncertain and the two equations oversimplify a very complex process, they provide a useful framework for discussion.

The frictional strength τ_m provides an upper limit to the tec-

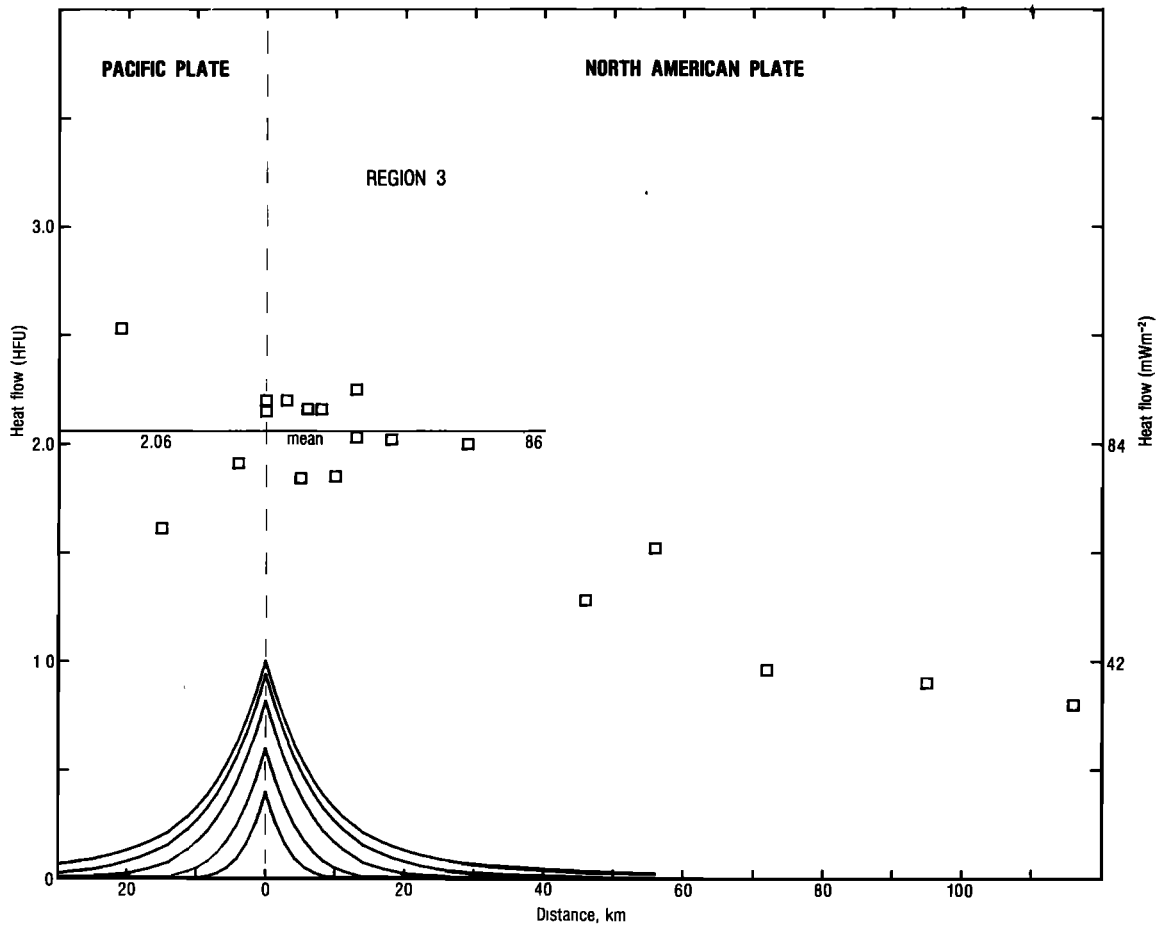

Fig. 15. Heat flow versus distance from the main trace of the San Andreas fault, region 3 (Figure 8), shown with reference anomaly. Horizontal 'mean-line' terminates at approximate edge of Coast Range province.

tonic stress that can be resolved on a fault surface and, consequently, on the initial stress prior to an earthquake. The frictional strength is not constrained by heat flow (13), and it may be as large as other constraints permit. The dynamic friction R is, of course, constrainted by heat flow, but only for those events responsible for most of the displacement on the San Andreas fault. We shall refer to such events as the 'principal events.' During principal events, the value of R may change if σ_n' changes (even if μ_k is assumed constant), but its displacement-average $\bar{R}$ must not exceed an average of ~100 bars over the faulted surface. In discussing the heat flow constraint in terms of rock friction, it is useful to distinguish between explanations that require small frictional strength τ_m and those that do not. In the first type, the fault is weak all of the time, and in the second type it must be weak only during principal events (the two classes are, of course, intergradational).

The simplest explanation of the first type ('permanent weakness') is that the fault contains intrinsically weak materials, for example, water-rich clay minerals [*Wu,* 1978; *Wang and Mao,* 1979, *Summers and Byerlee,* 1977] or quartz grains weakened by the action of water [*Rutter and Mainprice,* 1978] for which τ_m and hence R (15*b*) may never be much in excess of 100 bars. For such models the ambient tectonic stress in the fault zone must be very low. Models of the second type ('transient weakness') generally involve a mechanism for reducing friction while fault motion is in progress. They include the model of acoustic fluidization [*Melosh,* 1979], which can be viewed for our purpose as a reduction in R (15*a*) by a dynamic reduction of either the effective normal stress σ_n' or dynamic friction μ_k.

The most extensive body of laboratory data on sliding, rock surfaces can be interpreted in terms of models of either kind. It has been summarized by *Byerlee* [1978], who shows that for a remarkably wide variety of rock materials (with or without an intervening layer of disaggregated material) the maximum shearing stress τ_m on the sliding surface attained during each experiment is a simple linear function of the effective normal stress σ_n' on that surface. To conform to (14*a*), we have eliminated the constant in his fit to the experimental data and have adjusted the coefficient of friction μ accordingly (see appendix B). This results in the following value:

$$\mu \cong 0.75 \tag{16}$$

which yields a reasonably good approximation to Byerlee's equation for upper crustal conditions ($\sigma_n' < 6$ kbar).

After the frictional strength is reached in laboratory experiments, failure may proceed unstably by 'stick slip,' which is generally viewed as the analog of an earthquake, or by stable sliding, generally taken as the analog of a creep event in the earth. In spite of the generality of the laboratory results, *Stesky* [1978] cautions that 'we still don't know why Byerlee's law [generalized in (14) and (16)] holds nor why stick slip occurs. Until we understand the deformation mechanism, we will really have little confidence in extrapolating our laboratory results to the earth.' Nevertheless, the simplicity of By-

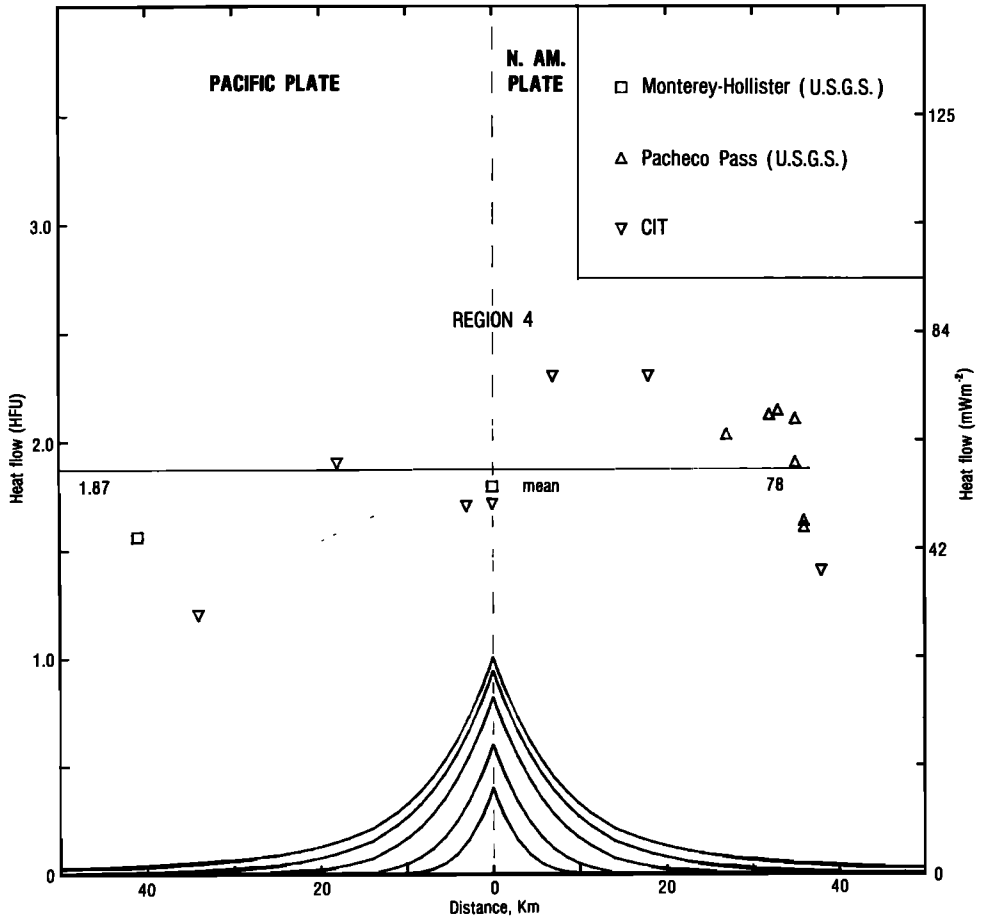

Fig. 16. Heat flow versus distance from the main trace of the San Andreas fault, region 4 (Figure 8), shown with reference anomaly. Horizontal 'mean-line' terminates at approximate edge of Coast Range province.

erlee's generalization ((14) and (16)) invites a comparison with the heat flow constraint on the San Andreas fault (13).

In experiments on polished granite, *Byerlee* [1970] found that $\bar{R}/\tau_m \sim 75\%$, and he commented that for other media the ratio is usually larger. To the degree of approximation of (14) and (15), this suggests

$$\frac{\mu_k}{\mu} \geq \frac{3}{4} \tag{17}$$

The approximation ((14) and (16)) leads to an expression for the frictional strength of the most favorably oriented fracture in terms of the maximum (σ_1'), minimum (σ_3'), and average (σ_{avg}'), effective principal stresses (see appendix B):

$$\begin{aligned} \tau_m &= 1.2\,\sigma_3' \\ &= 0.5\,\sigma_{avg}' \\ &= 0.3\,\sigma_1' \\ &= 0.4\,(\sigma_1 - \sigma_3) \end{aligned} \tag{18}$$

Equations (18) may be used to estimate frictional strength τ_m by inserting the appropriate effective stress at the time of failure. It may also be used (with (15), (16), and (17)) to calculate the average dynamic friction $\bar{R}$ provided we insert the appropriate average values of effective stress that obtain while faulting is in progress. We shall take the second choice, since it includes the first as a special case.

Combining (15*b*) and (18) and differentiating, we obtain expressions for the increase in dissipative resistance with depth:

$$\frac{d\bar{R}}{dx} = 1.2\,\frac{\mu_k}{\mu}\left[\frac{d\sigma_3}{dx} - \frac{dP}{dx}\right] \tag{19a}$$

$$= 0.5\,\frac{\mu_k}{\mu}\left[\frac{d\sigma_{avg}}{dx} - \frac{dP}{dx}\right] \tag{19b}$$

$$= 0.3\,\frac{\mu_k}{\mu}\left[\frac{d\sigma_1}{dx} - \frac{dP}{dx}\right] \tag{19c}$$

where the unprimed stresses denote total values. For the case in which the fluid pressure gradient is normal (~100 bars/km; by 'normal' we shall mean conditions in an unconfined column of water with unit specific gravity) and where the rock density ρ is 2.7 g/cm^3, (17) and (19) yield

$$\frac{d\bar{R}}{dx} = 153 \text{ bars/km} \qquad \bar{R}\ (7 \text{ km}) = 1070 \text{ bars} \qquad \sigma_3 \text{ vertical} \tag{20a}$$

$$\frac{d\bar{R}}{dx} = 64 \text{ bars/km} \qquad \bar{R}\ (7 \text{ km}) = 445 \text{ bars} \qquad \sigma_{avg} \text{ vertical} \tag{20b}$$

$$\frac{d\bar{R}}{dx} = 38 \text{ bars/km} \qquad \bar{R}\ (7 \text{ km}) = 270 \text{ bars} \qquad \sigma_1 \text{ vertical} \tag{20c}$$

where the vertical stress is assumed to represent the weight of overburden ($\rho g x$); $\bar{R}$ evaluated at $x = 7$ km represents the av-

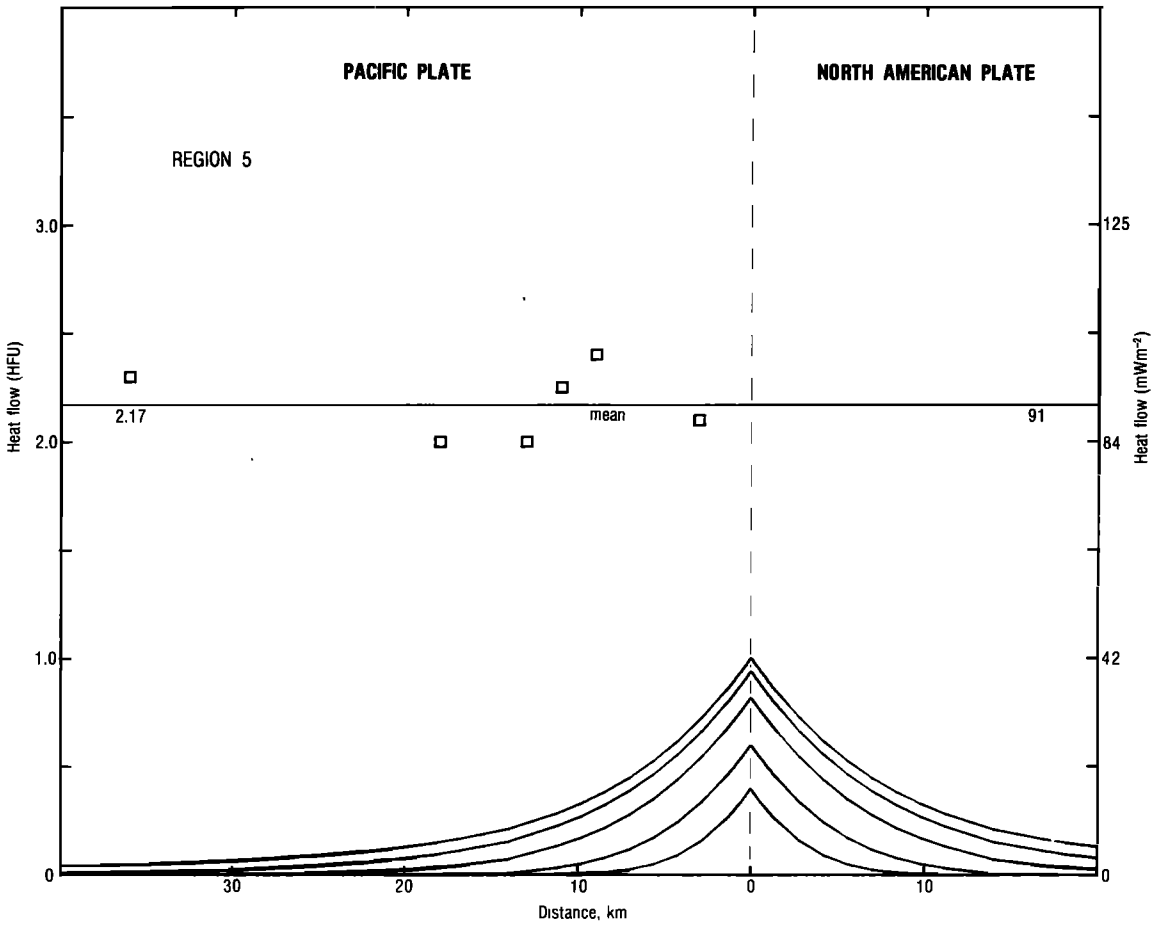

Fig. 17. Heat flow versus distance from the main trace of the San Andreas fault, region 5 (Figure 8), shown with reference anomaly.

erage resistance of a 14-km seismogenic layer. The values of $\bar{R}$ in (20) are perhaps the most 'expectable' ones for this extreme range of tectonic stress states. For an average slip velocity ($2v$) of 3 cm/yr they correspond (from top to bottom, respectively) to local conductive steady state heat flow anomalies of 2.4, 1.0, and 0.6 HFU. The constraint (13) imposed by the absence of such anomalies implies, however, that

$$\frac{d\bar{R}}{dx} \leqslant \frac{100 \text{ bars}}{7 \text{ km}} \sim 15 \text{ bars/km} \tag{21}$$

Combining this condition with (19) yields the constraint on the average fluid pressure during faulting:

$$\frac{dP}{dx} \geqslant 253 \text{ bars/km} \qquad \sigma_3 \text{ vertical} \tag{22a}$$

$$\frac{dP}{dx} \geqslant 230 \text{ bars/km} \qquad \sigma_{avg} \text{ vertical} \tag{22b}$$

$$\frac{dP}{dx} \geqslant 203 \text{ bars/km} \qquad \sigma_1 \text{ vertical} \tag{22c}$$

According to (22), fluid pressure during faulting would have to exceed the normal value by a factor of 2 or more, irrespective of the state of tectonic stress. This calculation illustrates the difficulty in trying to reconcile the heat flow constraint with Byerlee's law and the frictional theory of faulting. (A similar analysis has been made by *Stesky and Brace* [1973].)

This result says nothing about the frictional strength τ_m at the onset of faulting unless the effective stresses in (18) were the same before and during faulting. We shall assume that this condition is satisfied if the fluid pressure was unchanged during the event. For this case, we obtain the condition of permanent weakness ((13), (15*b*), and (17)):

$$\tau_m(\text{avg}) \leqslant 100 \text{ bars} \times \frac{\mu}{\mu_k} \cong 133b \tag{23}$$

The fluid pressures (22) would then be a permanent (ambient) condition of the fault zone. If the uncertain value of μ_k were decreased by a factor of 2, it would, of course, increase the limit on frictional strength proportionally, but the fluid pressures (22) required for materials satisfying Byerlee's law would be reduced by only 10% or so. The restriction (23) on frictional strength stems from the assumption that the fluid pressure governing failure is the same as the one governing dynamic friction. The alternative will be discussed presently, but first we shall comment on explanations for anomalous ambient fluid pressure.

The question arises whether the large fluid pressures implied by (22) could be generated by long-term frictional heating of the fault. Water expanding at constant volume under upper crustal conditions undergoes a pressure increase of about 15 bars/°C [*Lachenbruch*, 1980]. Hence to increase the fluid pressure by a factor of 2 from a hydrostatic state would require an average temperature increase of 47°C in a 14-km seismogenic layer. However, for a dissipative resistance of 100

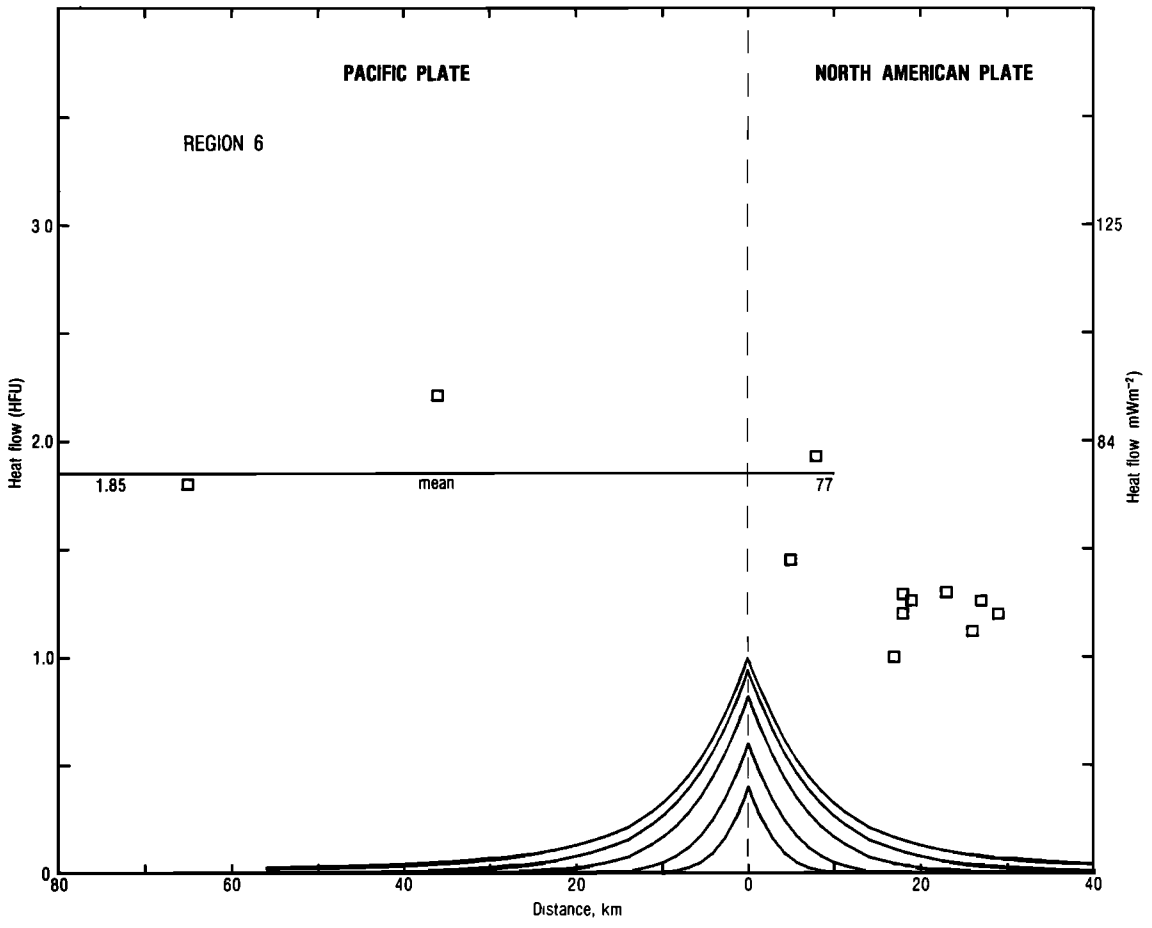

Fig. 18. Heat flow versus distance from the main trace of the San Andreas fault, region 6 (Figure 8), shown with reference anomaly. Horizontal 'mean line' terminates at the approximate edge of Coast Range province.

bars (13) and slip velocity of 4 cm/yr ($\bar{Q} \sim 0.3$ HFU, equation (10), Figures 3*c*, 4*c*, 5*c*, and 6*c*) the average temperature increase on the fault plane would be only 10° or 15°C after 10 m.y. of faulting. Hence even if the rock permeability were zero, this long-term source of high ambient fluid pressure does not seem possible. (Thermal expansion of pore fluid during evolution of the broad Coast Range anomaly is, however, a possible source; it will be discussed later.)

Berry [1973] has presented evidence for near-lithostatic fluid pressure in parts of the Franciscan formation, which bounds the San Andreas fault on the east in the Coast Ranges. *Irwin and Barnes* [1975] have noted that creeping portions of the fault occur where metamorphic fluids from the Franciscan formation are confined by an overlying section of the Great Valley sequence, and they postulate that in such places the confined fluid is forced into the fault zone. However, the heat flow data imply negligible dynamic friction in both the creeping and seismic portions and within the Coast Ranges and to the south (Region 7, Figures 8 and 19) where no Franciscan rocks occur. Hence it seems unlikely that the heat flow data can be accounted for by special local geologic conditions.

If the small dynamic resistance is to be reconciled with Byerlee's generalization, high fluid pressures seem inevitable. (We also have alternatives such as the intrinsically weak fault or acoustic fluidization, previously discussed.) However, such pressures do not have to be an ambient condition of the fault zone; they might be caused by transient frictional heating and expansion of the fluid during large earthquakes [e.g., *Sibson*, 1973], which probably account for most of the cumulative fault displacement. Important contributions to the transient pressure increase could also arise if there were relaxation of precusory pore dilatation or dehydration of clay minerals [*Raleigh*, 1977]. These alternatives, discussed in detail elsewhere [*Lachenbruch*, 1980], allow failure to occur at low ambient fluid pressure (P_0), thereby relaxing the constraint on frictional strength τ_m (23) and leading to a 'transient weakness' model. In this mechanism the shear stress would undergo an initial drop from a static value ($\leq \tau_m$) to $R(t = 0)$ (determined by (15*b*)), and subsequently, the pressure $P(t)$ would increase as the earthquake proceeded. As $P(t)$ approached σ_n, the effective normal stress σ_n' (15) would approach zero, and so would $R(t)$. One difficulty with the model concerns the possible limit imposed on $P(t)$ by σ_3, the least principal stress. As $P(t)$ approached σ_3, conditions for hydrofracturing would obtain, and further pressure increase might be inhibited. This condition can be written as

$$\begin{aligned} R(t) &\equiv \mu_k (\sigma_n - P(t)) \\ &\geq \mu_k (\sigma_n - \sigma_3) \\ &\geq \mu_k (\sigma_n - P_0)\left[1 - \frac{\sigma_3 - P_0}{\sigma_n - P_0}\right] \end{aligned} \tag{24}$$

Under these conditions, the minimum resisting stress $R(t)$ would be limited by ((B6*a*), (15) and (17))

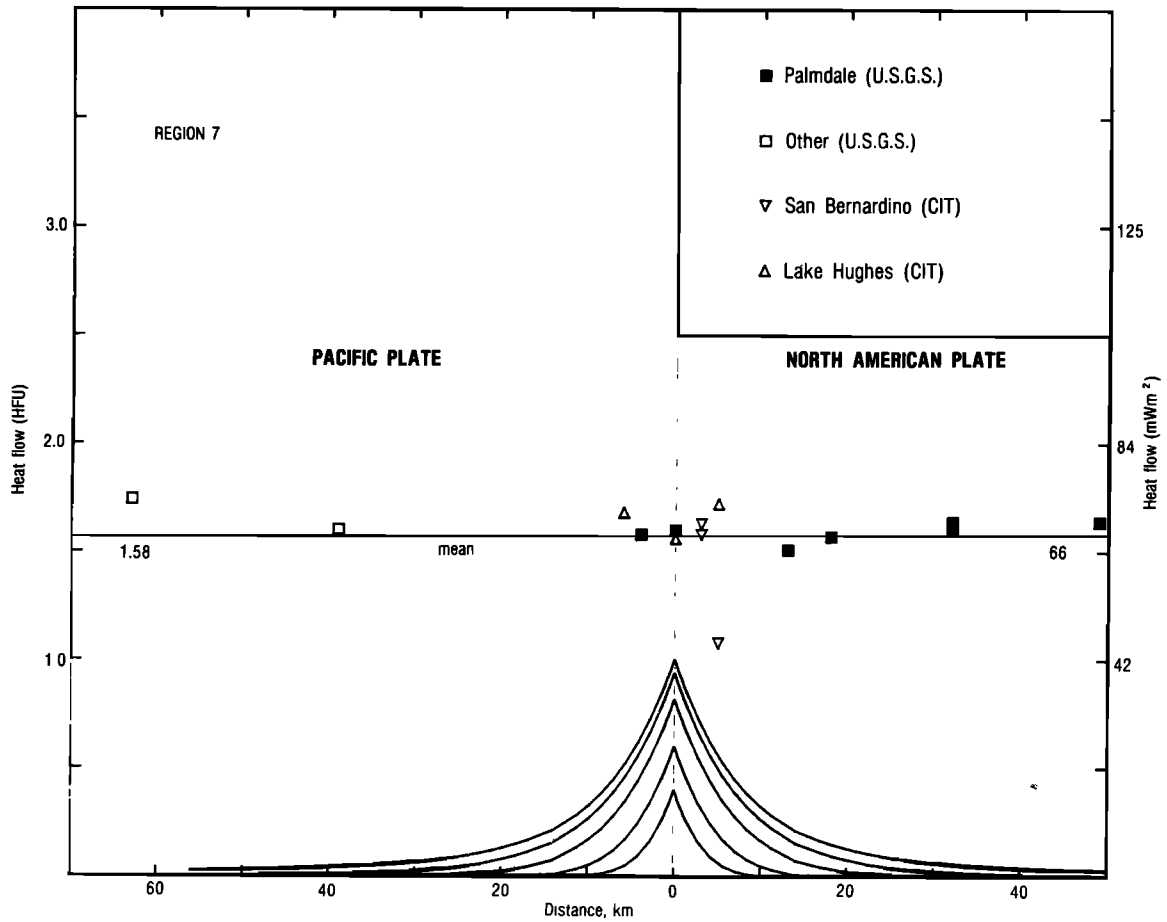

Fig. 19. Heat flow versus distance from the main trace of the San Andreas fault, region 7 (Figure 8), shown with reference anomaly.

$$R(t) \gtrsim 0.375\, R(0) \cong 0.375\, \frac{\mu_k}{\mu}\tau_m \qquad (25a)$$

$$\cong 0.28\tau_m \qquad (25b)$$

The average resisting stress $\bar{R}$, of course, would be a larger value obtained by integrating $R(t)$ [*Lachenbruch*, 1980]. Whether or not this limit (25) applies depends upon whether significant hydrofracturing can develop on the time scale of an earthquake.

Results from the above calculations are compared in Table 4. The case 'dry, $P = 0$' represents the maximum stresses permitted by (14)–(18). Case 2, Table 4 may be viewed as the transient alternative if we suppose the ambient pressure is normal and that an increase in fluid pressure or acoustic fluidization during slip events can indeed satisfy (13), i.e., that the resistance can be reduced from an initial value $R(t = 0)$ to yield an average $\bar{R} \lesssim 100$ bars for those events that account for most of the slip. Case 1, Table 4 represents the case of permanent weakness corresponding to constant ambient fluid pressure. If the permanent weakness results from anomalously weak gouge materials, the assumption (of (18) and Table 4) that faulting occurs on the most favorably oriented surface is not justified, but effects of the assumption on numerical values are probably unimportant for these approximate calculations. Hence the last three columns of Table 4, case 1, can probably be used whether the low strength results from high steady state fluid pressures or from anomalously weak fault materials. Tectonic stress differences in the last column of Table 4 are obtained from (18), and numerical values are based on $\mu_k/\mu = 0.75$, $\rho = 2.7$ g/cm^3.

The foregoing discussion can be summarized as follows:

1. The heat flow constraint on dissipative resistance (13) has strong implications for the frictional strength τ_m if we interpret faulting in terms of Byerlee's law and a frictional theory applied to a randomly fractured upper crust. The relation between $\bar{R}$ and τ_m depends upon two additional variables: the state of tectonic stress and the fluid pressure; it is most sensitive to the latter.

2. The heat flow constraint (13) requires that irrespective of tectonic stress state, fluid pressure must be near lithostatic while fault displacement is in progress if Byerlee's law applies.

3. Such high fluid pressure may be an ambient (steady state) condition of the fault zone (case 1, Table 4), or it may be a transient effect developed during the slip event (for example, case 2, Table 4).

4. If steady state (or if Byerlee's law does not apply, and the fault is intrinsically weak), then frictional strength τ_m is of the same general magnitude as dissipative resistance $\bar{R}$, differing only by the ratio of static to dynamic friction, and tectonic stress differences do not exceed a few hundred bars. This ('permanent weakness') alternative leaves the anomalous fluid pressure (required by faults satisfying (14)) unexplained.

5. If fluid pressure during faulting is transient (or if acoustic fluidization occurs), then ambient fluid pressures may be

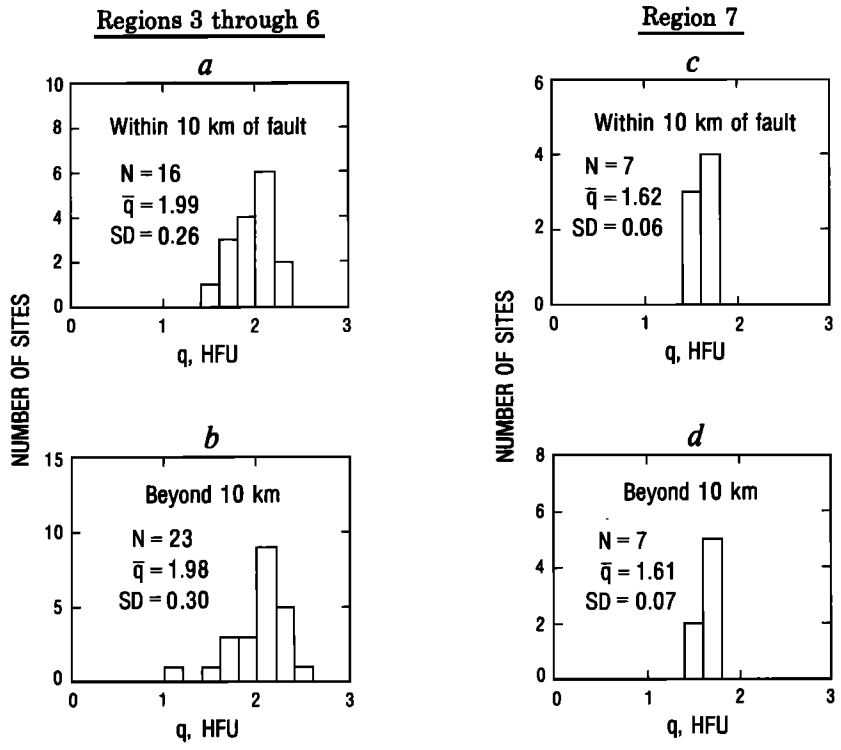

Fig. 20. A comparison between heat flow within 10 km of the main trace of the San Andreas fault (*a* and *c*) and heat flow at greater distances (*b* and *d*) for regions 3–6 (*a* and *b*) and region 7 (*c* and *d*).

normal, friction strength τ_m and tectonic stress may be large, and low dissipative resistance is explained as a consequence of the slip events. Difficulties with this ('transient weakness') alternative lie in our ignorance of the dynamics of transient events during faulting.

It might be argued that the absence of a local heat flow anomaly over presently creeping portions of the fault implies the condition of permanent weakness described by condition 4 above and that in such places at least, the tectonic stress differences must be very small. However, it can be shown from the results in appendix A that even if the resolved shear stress (and hence the average frictional resistance) on the fault were ~1 kbar, creep at plate velocities would have to persist for more than 10,000 yr before a measurable heat flow anomaly would result. Consequently, if creep episodes of centuries or even thousands of years duration were separated by much longer episodes of seismic displacement, the heat flow constraint could be satisfied with large tectonic stress (condition 5, above) if large earthquakes were responsible for most of the displacement and if they developed high transient fluid pressures. In the next section, we shall investigate seismological constraints on this alternative.

Fault Energetics and Seismic Estimates of Stress Difference

In the last section, we found that insofar as laboratory information on rock friction is concerned, there are two intergradational classes of simple models that can account for the low dynamic friction implied by the heat flow constraint: (1) permanent-weakness models in which the average frictional strength is also low, and (2) transient-weakness models in which the static friction may be an order of magnitude greater, the upper limit being determined by rock strength. The first type requires low tectonic (i.e., initial) stresses, but the second type permits large ones. In this section, we examine the energetics of the earthquake process and find that models of the second type yield large quantities of radiated kinetic energy, in apparent contradiction with interpretations of a large body of seismic observations. We shall introduce one new unknown, the final elastic stress, and two new partially known quantities obtained from seismology, the apparent stress and the stress drop (defined below).

Figure 22 is a schematic representation of the local energy budget of an earthquake [see also *Andrews*, 1978*a*]. Here, τ^* and τ' are the initial and final average values of the component of elastic shearing stress in the direction of fault slip u, and $\bar{r}$ is the corresponding average value of the dissipative resistance in the direction opposite to fault slip. The total slip averaged over the faulted surface is u_m. (We shall denote the faulted surface by Σ, and its area by A_Σ.) The straight line joining the average initial and final elastic stresses represents the unloading of a linear elastic medium; the area beneath it is the total elastic energy (E/A_Σ) released (per unit area of slipped surface) at the locus of faulting Σ. Hence

$$\frac{E}{A_\Sigma u_m} = \frac{1}{2}(\tau^* + \tau') \tag{26}$$

The area beneath the horizontal line with ordinate $\bar{r}$ or the curve $r(u)$ (Figure 22*b*) is energy (E_R/A_Σ) lost from the mechanical system. Thus

$$\frac{E_r}{A_\Sigma u_m} = \bar{r} \tag{27}$$

The area between the elastic stress curve and the dissipation curve represents energy (E_a/A_Σ) allocated to elastic radiation. Consequently,

$$\frac{E_a}{a_\Sigma u_m} = \frac{1}{2}(\tau^* + \tau') - \bar{r} \tag{28}$$

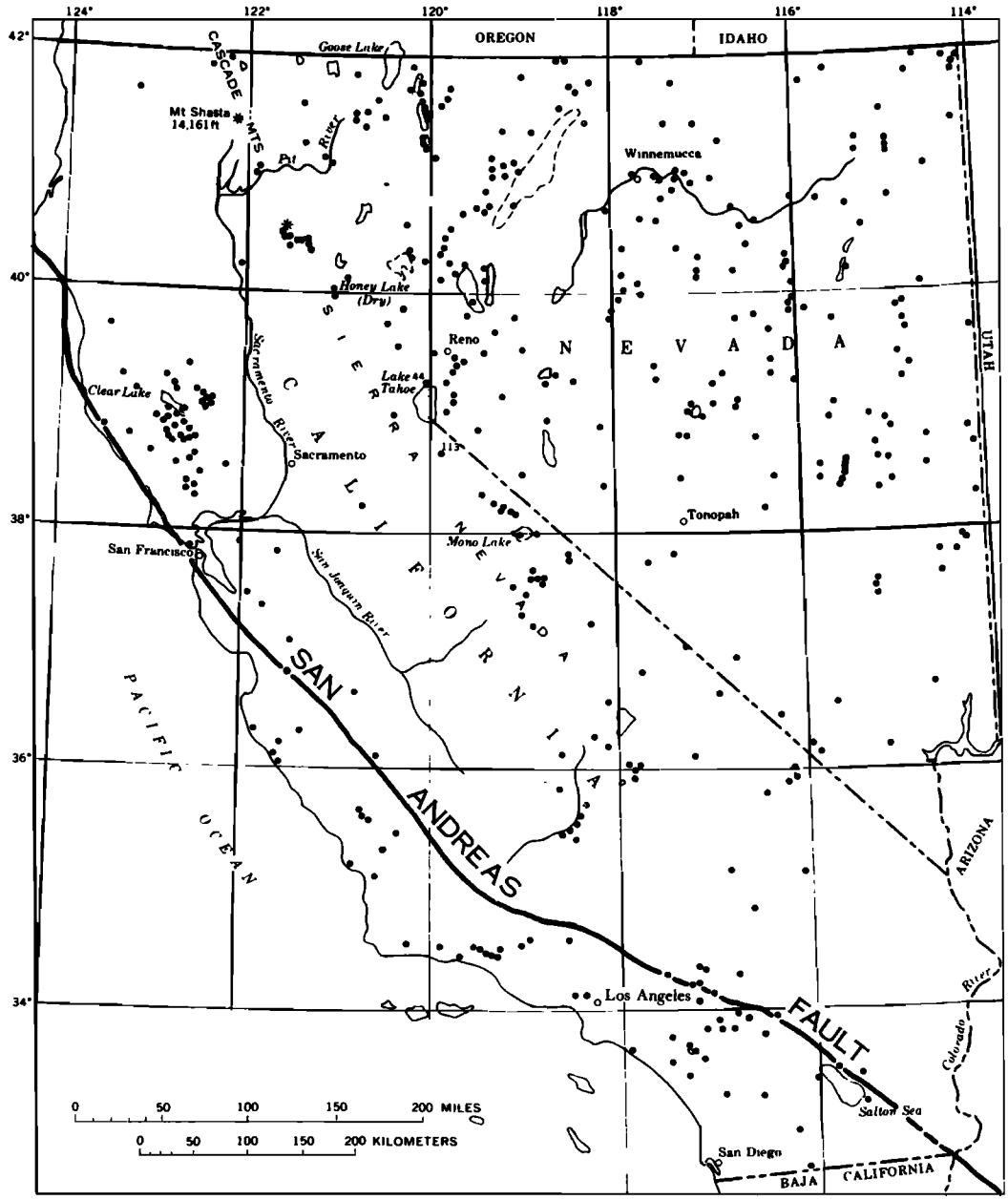

Fig. 21. Thermal springs in California and Nevada (reproduced with modifications from figure 8 of *Waring* [1965]). Heavy line is the main trace of the San Andreas fault.

Figure 22*a* is shown for three different values of $\bar{r}$ and Figure 22*b* for variable r.

This interpretation of areas in Figure 22 is fairly general as long as we define τ^*, τ', and $\bar{r}$ respectively, as weighted averages of initial stress, final stress, and $\bar{R}$ (15*c*) over the faulted surface, the weighting function being the local fault slip. For refined models of faulting in which significant amounts of energy are dissipated at the propagating edges in complex stress fields, the representation in Figure 22 will not, in general, provide a useful view of the sequential values of the stresses at any typical location. Nevertheless, the three generalized stresses (τ^*, τ', $\bar{r}$) defined in this way are useful descriptive parameters, whatever their relation may be to the details of the mechanics of the earthquake process. For the purpose of discussion, we can consider Figure 22 to represent one-dimensional models of the fault, in which case their intuitive meaning is clearer.

We define the average elastic stress τ_e and the apparent stress τ_a by

$$\tau_e = \frac{1}{2}(\tau^* + \tau') \tag{29}$$

$$\tau_a = \frac{1}{2}(\tau^* + \tau') - \bar{r} \tag{30}$$

The energy balance,

$$E = E_a + E_R \tag{31}$$

can now be expressed ((26)–(31)) as

$$\tau_e = \tau_a + \bar{r} \tag{32}$$

TABLE 3. Data on Thermal Springs Within 10 km of the Main Trace of the San Andreas Fault Between Cape Mendocino and the San Bernardino Mountains

Name	Latitude	Longitude	Flow Rate $l\,s^{-1}$	Temperature, °C	Discharge, MW
Point Arena Hot Springs	38°52.5′	123°31′	0.3	44	0.035
Rocky Point Spring	37°53′	122°37′	0.3	38	0.030
Near Sergent Santa Clara County	36°56.8′	121°33.8′	0.5	25	0.020
Fresno Hot Springs	36°8.8′	120°33.5′	1.3	31–36	0.110
Tyler's Bath Springs	34°13.5′	117°29.5′	0.3	33	0.015
Arrowhead Hot Springs	34°11.2′	117°14.5′	3.2	94	1.0
Waterman Hot Springs	34°11′	117°15.5′	0.3	50	0.04
					1.25 Total

Thus the deformation energy released locally during an earthquake is the work done by the average operating elastic stress τ_e, which can be expressed as the sum of a part allocated to the production of seismic radiation, τ_a, and a part allocated to the production of heat, $\bar{\tau}$. For the transient class of models discussed previously, τ_e can be large, and since $\bar{\tau}$ must be small, this would imply large seismic radiation (i.e., large τ_a). The permanently weak models, on the other hand, would be consistent with small contributions from both $\bar{\tau}$ and τ_a. In what follows, we shall express the energy constraint (32) in terms of the friction parameters of the last section so that the numerical results obtained there can be compared formally to those obtained from seismology.

The relations among the seismically related stresses can be discussed in terms of the following identity:

$$\bar{\tau} \equiv \tau^* - \frac{1}{2}(\tau^* - \tau') - \left[\frac{1}{2}(\tau^* + \tau') - \bar{\tau}\right] \tag{33}$$

Although seismology provides no reliable means of estimating the magnitudes of the three stresses in (33), it does provide indirect estimates of two stress differences [*Wyss and Brune,* 1968; *Wyss,* 1970; *Savage and Wood,* 1971]: the apparent stress τ_a, just discussed (30), and the stress drop Δ, which is the difference between the average fault stress immediately before and after an earthquake:

$$\Delta \equiv \tau^* - \tau' \tag{34}$$

The seismic efficiency η is defined as the fraction of the released energy that is allocated to the generation of elastic waves:

$$\eta = \frac{E_a}{E} = \frac{\tau_a}{\tau_a + \bar{\tau}} \tag{35}$$

Combination of (30), (33), and (34) yields

$$\tau^* - \bar{\tau} \equiv \tau_a + \frac{1}{2}\Delta \tag{36a}$$

$$\tau' - \bar{\tau} \equiv \tau_a - \frac{1}{2}\Delta \tag{36b}$$

Since $\bar{\tau}$, τ_a, and Δ are generally positive on physical grounds, it follows from (36*a*) that the average initial stress has lower bounds given by

$$\tau^* > \bar{\tau}, \tau_a, \frac{1}{2}\Delta > 0 \tag{37}$$

If we limit our discussions to events typical of those whose cumulative effect resulted in hundreds of kilometers of displacement on the San Andreas fault (the 'principal events'), we can write the heat flow constraint (13) as

$$\bar{\tau} \lessapprox 100 \text{ bars} \tag{38}$$

The preponderance of values of stress drop Δ determined for crustal earthquakes [*Hanks,* 1977; *Kanamori and Anderson,* 1975] satisfy

$$1 \text{ bar} < \Delta < 100 \text{ bars} \tag{39}$$

Although seismically estimated values of τ_a are less certain, *Savage and Wood* [1971] present data from many earthquakes to show that within reasonable limits of uncertainty,

$$\tau_a < \frac{1}{2}\Delta \tag{40}$$

and *Kanamori and Anderson* [1975] find that on the average $\tau_a \sim (1/2)\Delta$.

Substituting upper limits given by (38), (39), and (40) in (36*a*) and using (37), we obtain bracketing conditions for the initial stress τ^* preceding earthquakes:

$$0 < \bar{\tau}, \tau_a, \frac{1}{2}\Delta \lessapprox \tau^* \equiv \bar{\tau} + \tau_a + \frac{1}{2}\Delta \leqq 200 \text{ bars} \tag{41a}$$

The right-hand inequality is equivalent to the result obtained by *Brune et al.* [1969] (except that they used $\tau_a \lessapprox 100$ bars instead of (40)). Their result for the case in which displacement

TABLE 4. Ambient Conditions in Fault Zone for Three Tectonic Stress States: Case 1. Fluid Pressure Does Not Change With Time, Case 2. Ambient Fluid Pressure 'Normal' and (13) Satisfied By Transient Effects

Case	Ambient Pressure Gradient, dP/dx, bars/km	Initial Dynamic Resistance, $R(t=0)$, bars	Frictional Strength, τ_m, bars	Tectonic Stress Difference, $\sigma_1 - \sigma_3$, bars
		σ_3 Vertical (Thrust Faulting)		
Case 1	≳253	≲100	≲133	≲332
Case 2	100	1070	1426	3565
Dry, $P=0$	0	1700	2265	5560
		σ_{avg} Vertical		
Case 1	≳230	≲100	≲133	≲332
Case 2	100	445	593	1482
Dry, $P=0$	0	710	990	2355
		σ_1 Vertical (Normal Faulting)		
Case 1	≳203	≲100	≲133	≲332
Case 2	100	270	360	900
Dry, $P=0$	0	430	570	1430

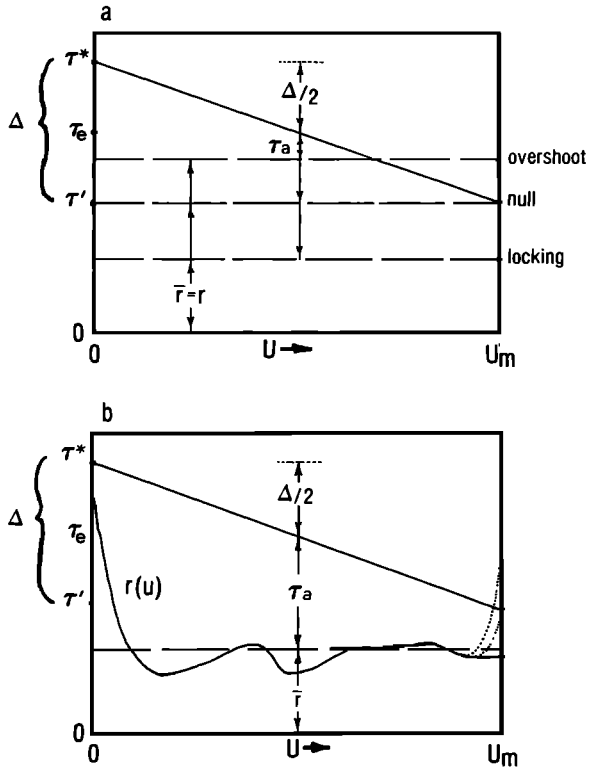

Fig. 22. Schematic representation of relations among averaged values of initial stress τ^*, final stress τ', dissipative resistance $\bar{r}$, apparent stress τ_a, mean elastic stress τ_e, and stress drop Δ for an event with mean total displacement u_m. Figure 22*a* illustrates the three cases of (42), and Figure 22*b* shows a one-dimensional locking model with variable dynamic friction r.

is exclusively by uniform creep follows from (41*a*) by setting $\Delta = \tau_a = 0$:

$$\tau^* \leqslant 100 \text{ bars} \qquad (41b)$$

The result (41*b*) is essentially the same as the frictional result (23), since both are controlled by the heat flow constraint. However, the upper limit of 200 bars in (41*a*), obtained from heat flow and seismic observations combined, imposes a much more severe constraint than rock strength (Table 4), which limited the initial stress in models of transient weakness, discussed in the last section. Because of the potential importance of the possibility of large initial stress to the understanding of earthquakes, we shall eliminate the least certain of the seismic constraints, the one on τ_a (40), substitute the limit on rock strength (Table 4), and investigate some of the consequences.

Simple earthquake models can be discussed in terms of the relative magnitudes of the final stress and the average resisting stress [see *Brune*, 1976]. The three possibilities, illustrated in Figure 22*a*, are

$$\tau' - \bar{r} < 0 \quad \text{overshoot} \qquad (42a)$$

$$= 0 \quad \text{null} \qquad (42b)$$

$$> 0 \quad \text{locking} \qquad (42c)$$

If it is assumed that the resisting stress is constant (i.e., $r(u) \equiv \bar{r}$), the null model (the 'Orowan assumption' of *Brune et al.* [1969]) attributes the final stress to the dynamic frictional characteristics of the surface. The locking model [e.g., *Brune*, 1976] is unrelated to average friction; it could occur in a one-dimensional model with elastic barriers (for example, the jumping of one notch in opposing sawteeth). *Savage and Wood* [1971] point out that if friction stops the faulting, inertia requires the overshoot model, a sufficient condition for which is (40) (according to (42*a*) and (36*b*)). If, however, the resisting stress varies during an earthquake, the physical significance of this classification is lost, since the final value, not the average $\bar{r}$, should be used in (42) to relate τ' to friction. This is illustrated in Figure 22*b* for a one-dimensional locking model (42*c*) in which r increases sharply at the end of an event (dotted lines, Figure 22*b*). *Brune* [1976] suggests that such an increase in resistance might result when the particle velocity drops below a critical limit. The resistance is sensitive to shear zone width and pore dilatation, both of which vary as particle velocity changes during an earthquake; unstable propagation of hydrofractures might reduce fluid pressure rapidly, and strengthening due to loss of fluid pressure by dissipation of frictional heat or Darcian flow can probably contribute [*Lachenbruch*, 1980]. For the case of acoustic fluidization [*Melosh*, 1979], rapid strengthening might occur in the decelerating stage with the loss of acoustic energy. In any case, however, the classification in (42) is useful for discussion; for a given stress drop and resistance, τ_a and the seismic efficiency will be greatest for the locking model. Intuitively, the locking model generates additional elastic radiation by its terminal impact against a large hypothetical final resistance. (We make no attempt to reconcile these suggestions with fracture mechanical considerations of fault stoppage.)

In one-dimensional models it is natural to equate the average initial stress τ^* to the frictional strength τ_m. For more realistic two- and three-dimensional models, it is clear that the initial stress must equal the strength only at the point at which rupture initiates (and this strength may be lower than the laboratory value because of the size effect); elsewhere the stress is probably determined by dynamic friction [e.g., *Berg*, 1968; *Burridge and Halliday*, 1971]. We shall assume therefore that the average value of initial stress can be bracketed by the static and dynamic friction:

$$\tau_m \geqq \tau^* \geqq \frac{\mu_k}{\mu} \tau_m \qquad (43)$$

We shall consider two cases, τ_m small and τ_m large, corresponding respectively to cases 1 and 2, Table 4. The permanent low strength in case 1 can result from high steady state fluid pressure or from intrinsically weak fault materials. The high strength in case 2 is a consequence of normal ambient fluid pressure; weakening during the earthquake can be from a transient increase in fluid pressure or acoustic fluidization. The limiting values on the left and right in (43) are represented respectively by columns 2 and 3 in Table 4. Thus in case 2, (43) becomes

(270 bars, 445 bars, 1070 bars)

$$\leqq \tau^* \leqq \text{(360 bars, 595 bars, 1425 bars)} \qquad (44)$$

where the values from left to right in parentheses correspond respectively to the stress states: σ_1 vertical, σ_{avg} vertical, and σ_3 vertical. The corresponding result for case 1 (constant fluid pressure or an intrinsically weak fault) is ((23) and (28*c*))

$$0 < \bar{r}, \tau_a, \frac{1}{2}\Delta < \tau^* \leqq \frac{\mu}{\mu_k}\bar{r} \cong 133 \text{ bars} \qquad (45)$$

In evaluating the constraint on other stresses, we shall use (44) or (45), inferred from frictional properties, the heat flow con-

straint (38), and the constraint on stress drop (39). The apparent stress τ_a, possibly the least certain of the semimeasurable quantities, will be retained as a parameter.

Using the left-hand inequality in (44) with (36), (38), (39), (41), and (43), we obtain the following lower limits for the transient case 2:

$$\tau^* - \bar{\tau} \gtrsim (170 \text{ bars}, 345 \text{ bars}, 970 \text{ bars}) \quad (46a)$$

$$\tau_a \gtrsim (120 \text{ bars}, 295 \text{ bars}, 920 \text{ bars}) \quad (46b)$$

$$\tau' - \bar{\tau} \gtrsim (70 \text{ bars}, 245 \text{ bars}, 870 \text{ bars}) > 0 \quad (46c)$$

$$\eta \gtrsim (0.55, 0.75, 0.90) \quad (46d)$$

Similarly, for case 1, (45) and the foregoing relations yield

$$\tau^* - \bar{\tau} \lessapprox \left(\frac{\mu}{\mu_k} - 1\right)\bar{\tau} \lessapprox 33 \text{ bars} \quad (47a)$$

$$0 < \tau_a \lessapprox 33 \text{ bars} - \frac{1}{2}\Delta < 33 \text{ bars} \quad (47b)$$

$$-50 \text{ bars} \lessapprox -\frac{1}{2}\Delta \lessapprox \tau' - \bar{\tau} \lessapprox 33 \text{ bars} - \Delta < 33 \text{ bars} \quad (47c)$$

$$\eta = \frac{\tau^* - \bar{\tau} - \frac{1}{2}\Delta}{\tau^* - \frac{1}{2}\Delta} \lessapprox \frac{\tau^* - \bar{\tau}}{\tau^*} \lessapprox \left(1 - \frac{v_k}{\mu}\right) \cong 0.25 \quad (47d)$$

Thus the transient high-stress alternative (case 2) requires very large τ_a (46*b*) in violation of (40). This leads to a high seismic efficiency (46*d*) and the requirement for a locking-type earthquake model (46*c*) according to the classification of (42). In contrast, the steady state pressure alternative (or the intrinsically weak fault) is consistent with the small values of τ_a (47*b*) usually reported; it leads to a low seismic efficiency (47*d*) and could be consistent with any of the three alternatives in (42) (see (47*c*)).

Although it compounds the problem of fault stoppage, the transient alternative, with initial stress ~1 kbar and dissipative resistance ≤0.1 kbar, is not inconsistent with the observation that the stress drop Δ is generally small (≤0.1 kbar). It is, however, inconsistent with the general inference that τ_a is small and, in particular, with the Savage and Wood constraint (40). However, the physical argument for the validity of (40) is based on the constancy of r and does not necessarily apply in the transient case. The question then remains whether the seismically determined quantity τ_a corresponds to the one defined in this section, or whether the seismic 'τ_a' might represent only a small fraction of the energy radiated from the locus of faulting during those events responsible for most of the displacement on the San Andreas fault, probably very large earthquakes. Only in the latter case would the transient alternative and the possibility of large strength and tectonic stress be viable [see also *Brune et al.*, 1969].

In summary, the heat flow constraint, taken with measurements of rock friction and seismic observations, seems to have the following implications regarding stresses on the San Andreas fault:

1. If we accept the heat flow constraint, then resistance to fault motion must be small (≲100 bars = 10 MPa) during those events responsible for most of the fault displacement (the 'principal events').

2. This condition can be satisfied by two simple (intergradational) classes of models: (1) Those in which the fault resistance is small all of the time ('permanent weakness'), or (2) those in which it is small only during short-lived events, including but not necessarily limited to the principal events ('transient weakness').

3. For the class 1 models, the average resolved tectonic stress on the fault cannot be appreciably greater than 100 bars. For the class 2 models, tectonic stress is limited by the average frictional strength of upper crustal rocks; under normal fluid pressure this is ~0.4–1.5 kbar, depending on tectonic stress state.

4. If the principal events are slow creep, permanent-weakness (type 1) models are required. However, creep events at plate velocities lasting no longer than $\sim 10^4$ yr are not necessarily principal events (i.e., they need not contribute appreciably to the heat flow even if the ambient stress is large).

5. Physical models for permanent weakness (type 1) include those in which the gouge material has anomalously low friction coefficients, and those in which the friction coefficients are normal, but the ambient fluid pressure in the fault zone is close to the overburden pressure. Although there is little independent information that either of these conditions is general in the fault zone, these models are consistent with the small stress drops and apparent stresses (and, consequently, small seismic radiation) inferred from earthquake seismology. Models of type 1 require low seismic efficiency; they are consistent with all three types of earthquake models: locking, null, and overshoot.

6. Physical models for transient weakness (type 2) include those in which the ambient fluid pressure and frictional strength of the fault zone are normal, and resistance is decreased during principal events, for example, by a transient increase in fluid pressure [*Lachenbruch*, 1980] or acoustic fluidization [*Melosh*, 1979]. For such models, the principal events are probably large earthquakes. These models have the advantage that the anomalous weakness (necessary to satisfy the heat flow constraint) is 'explained' as a consequence of the slip event. Only models of this type can be consistent with large ambient tectonic stress and the heat flow constraint. They have the disadvantage that for tectonic stress controlled by normal rock strength, they require apparent stresses in the range 100 bars–1kbar (depending on tectonic stress state). This is an order of magnitude greater than the range inferred for crustal events from earthquake seismology. For large tectonic stress, type 2 models require large seismic efficiency and locking models of the earthquake process for principal events.

Factors that might control the transient variations of fluid pressure during an earthquake are discussed in another paper [*Lachenbruch*, 1980]. Although they might ultimately prove to be important to the earthquake process, if the heat flow and seismic data are taken at face value (41*a*), even such transient-weakness models are limited by a fault strength of only ~200 bars. In the next section, we shall investigate the possible relation between these local fault stresses and those throughout the broader interplate shear zone by considering the origin of the broad Coast Range heat anomaly. It is shown that if much of the heat flow anomaly is mechanically generated, it is likely that the seismogenic layer is partially decoupled from the underlying material and that the resulting basal stresses lead naturally to a relatively weak fault, with much larger stresses elsewhere in the shear zone.

THE BROAD HEAT FLOW ANOMALY AND ENERGETICS OF THE FAULT ZONE

The heat flow data from the San Andreas fault region have two notable features: (1) the absence of a local heat flow anomaly over the 1000-km length of fault trace from which

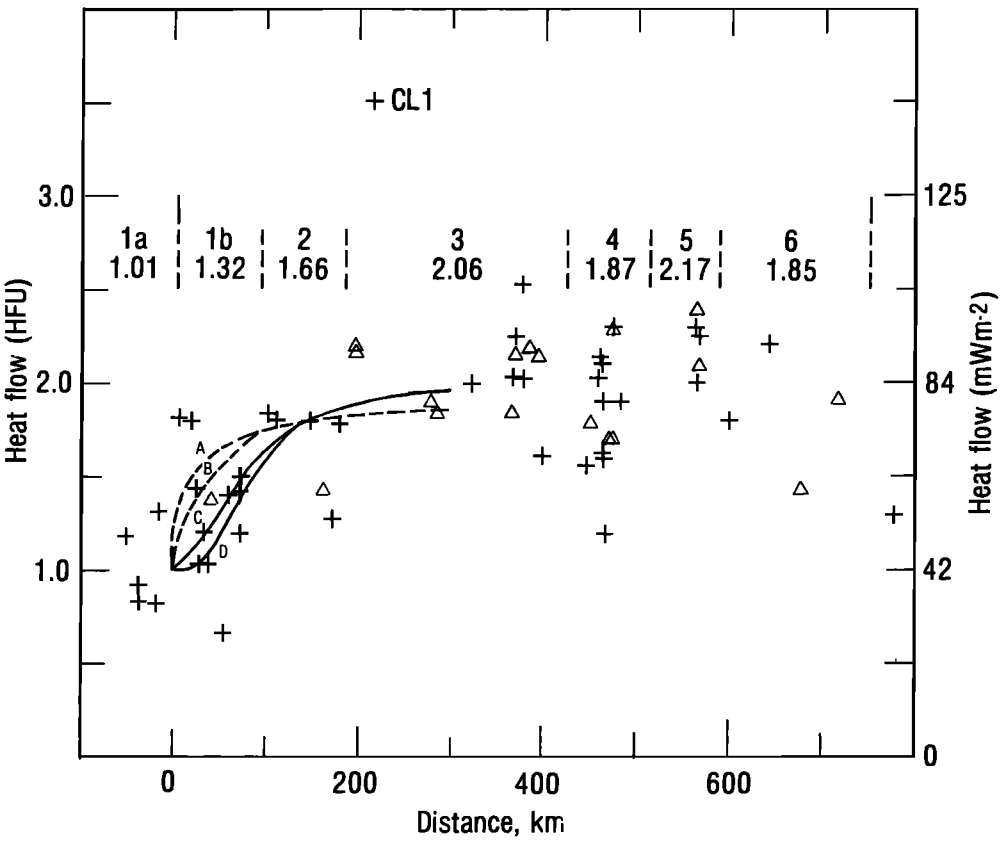

Fig. 23. Northern portion of Figure 12 showing models for the transient rise in temperature caused by northward migration of the Mendocino Triple Junction. Curves A, B, C, and D correspond to models of equations (38*a*), (38*b*), (38*c*), and (38*d*), respectively. Mean heat flows (in HFU) are indicated for each region.

data are available, and (2) the broad anomaly across the Coast Ranges extending for more than 500 km along the fault zone (regions 3 through 6, Figures 8 and 12). In the previous section we discussed some implications of the first feature for the local mechanics of the main fault. In this section we shall consider possible implications of the Coast Range anomaly for thermal and mechanical conditions throughout a broad interplate shear zone surrounding the main fault. The analysis is limited to the Coast Range anomaly, because it is a conspicuous feature with well-defined boundaries on the east and north, and it encloses a region in which most of the relative plate motion can generally be attributed to the main trace of the San Andreas fault. However, the possible westward extent of the anomaly onto the continental shelf is unknown. South of the Coast Ranges, conditions are very complex, the shearing deformation is evidently distributed over a broader zone, and the heat flow anomaly is smaller but distributed over a large region including the offshore borderland and parts of the Mojave Block and the Salton Trough; an island of low heat flow occurs in the southern California batholith (Figure 6) [see also *Roy et al.*, 1972]. Possible relations between heat flow and the tectonics of this complicated region have been discussed by *Lee and Henyey* [1975]; present heat flow coverage there is inadequate to warrant the construction of explicit models.

The Coast Range Anomaly and Depth to Its Source

From heat flow measurements in central California, we noted in an earlier paper [*Lachenbruch and Sass*, 1973] that the Coast Range anomaly falls off from average values of about 2 HFU to values of perhaps 1.2 HFU in the Great Valley to the east over a distance of only tens of kilometers (see, for example, Figures 15 and 18). This suggests that the source of the Coast Range anomaly is in the upper crust and that it might be related to the tectonics of the San Andreas fault zone; however, details of the thermal transition are complicated by effects of rapid sedimentation in the western portion of the Great Valley. To test the relation between the fault zone and the heat flow anomaly, we subsequently extended measurements northward to and beyond the Mendocino Triple Junction, where the San Andreas fault on the North American plate should, in principle, have zero age. Owing to the nature of the formations and the youthful topography, confident heat flow measurements in this northern region (as in many other parts of the Coast Ranges) are difficult to obtain, and this might account for much of the scatter in the data. Nevertheless, the results shown in Figure 12 suggest that the Coast Range anomaly does, indeed, fall off to the north. North of the Triple Junction (region 1a, Figure 12) the average heat flow is about 1 HFU, consistent with results from the Klamath Mountains and northward along a coastal strip to the Canadian border (see Figure 6), the region in which subduction is believed to be in progress today [see also *Lachenbruch and Sass*, 1977; *Blackwell*, 1978]. South of the Triple Junction, average heat flows seem to rise over a distance of about 200 km (regions 1b and 2, Figure 12) to values characteristic of the Coast Range anomaly.

From plate tectonic reconstructions [*Atwater and Molnar*, 1973], the Triple Junction is believed to have been migrating northwestward at roughly 5 cm/yr for the past several million years. Hence the age of the fault zone on the North American plate should increase about 1 m.y. for each 50 km of distance

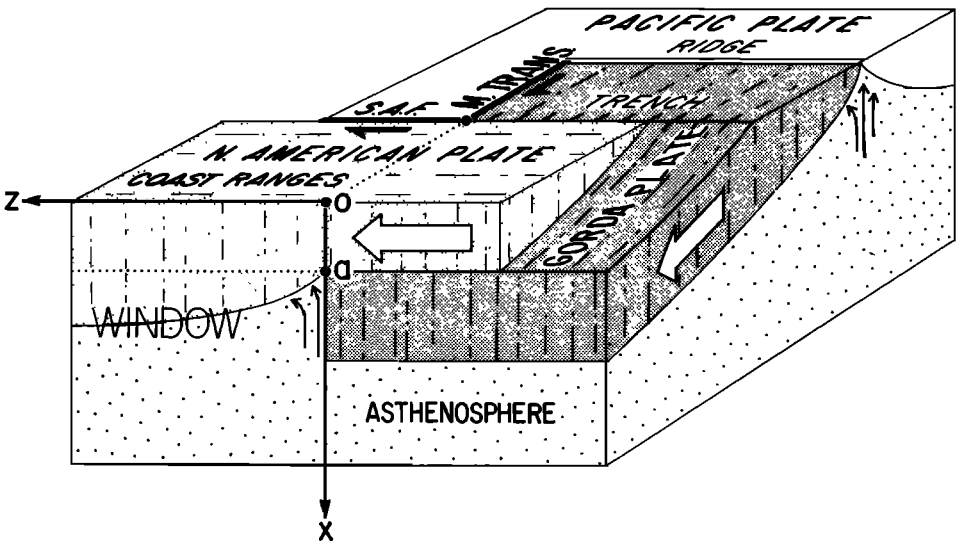

Fig. 24. Idealized relations among tectonic plates near the Mendocino Triple Junction (intersection of the Mendocino transform (M. Trans.) and the San Andreas fault (S.A.F.)). Arrows indicate motion relative to a fixed Pacific plate. Coordinate axes refer to model in text (see also Figure 25).

southeastward from the Mendocino Triple Junction. (All of the sites in the arbitrary regions 1b and 2 (Figure 12) were, of course, on the North American plate as the Triple Junction migrated northward along an offshore trench.) To obtain a rough idea of the depth of the sources that might be responsible for the northward transition in heat flow, we have shown the effects of four simple one-dimensional transient heat conduction models, curves A, B, C, and D, in Figure 23. For each model the time origin is taken at the present Triple Junction, and each anomaly is constrained to reach 80% of its steady state value of 1 HFU at 3 m.y., which corresponds to a point about 150 km southeastward from the present Triple Junction. For each model, the depth of anomalous sources ($x = d$) was adjusted to meet these conditions; the results are

Model A: constant plane source at $x = d$; $d \cong 3$ 1/2 km (48*a*)

Model B: uniform sources in $0 \leqq x \leqq d$; $d \cong 7$ km (48*b*)

Model C: step change in flux at $x = d$; $d \cong 11$ km (48*c*)

Model D: step change in temperature at $x = d$; $d \cong 20$ km (48*d*)

The deeper the source, the greater its initial strength must be and the more intense is the associated temperature anomaly; for example, model C requires an initial source strength twice as great as model A and a temperature anomaly greater by a factor of 3. If the values of d were doubled, the horizontal scale of curves in Figure 23 would be extended by a factor of 4. Thus as in the transition toward the Great Valley, a shallow origin ($\lesssim$20 km) is suggested.

Before undertaking further analysis of these results, it is worth noting that the observed increase in heat flow would correspond to an increase in thermal gradient above the source of $\gtrsim$15°C/km. The expansion of pore water at constant volume under upper crustal conditions leads to a fluid pressure increase ~ 15 bars/°C [see, e.g., Figure 3, *Lachenbruch,* 1980]. Consequently, an increase in thermal gradient of only ~13°C/km could increase the fluid pressure gradient by ~200 bars/km, enough to raise the fluid pressure from hydrostatic to lithostatic. In the Coast Ranges, this could be effective if the time constant for Darcian flow were an order of magnitude greater than the time constant for heat flow, i.e., if the permeability of overlying rocks did not exceed ~0.1 nanoDarcy [see Figure 8, *Lachenbruch,* 1980]. A possible source of water is sediment scraped from the subducting plate. Hence it is quite possible that the thermal evolution of the broad Coast Range anomaly could have a substantial effect on the mechanical evolution of the San Andreas fault zone through the weakening effect of high fluid pressure on mid- and upper-crustal rocks.

We can imagine two plausible mechanisms for the anomalous near-surface source of heat in the Coast Ranges:

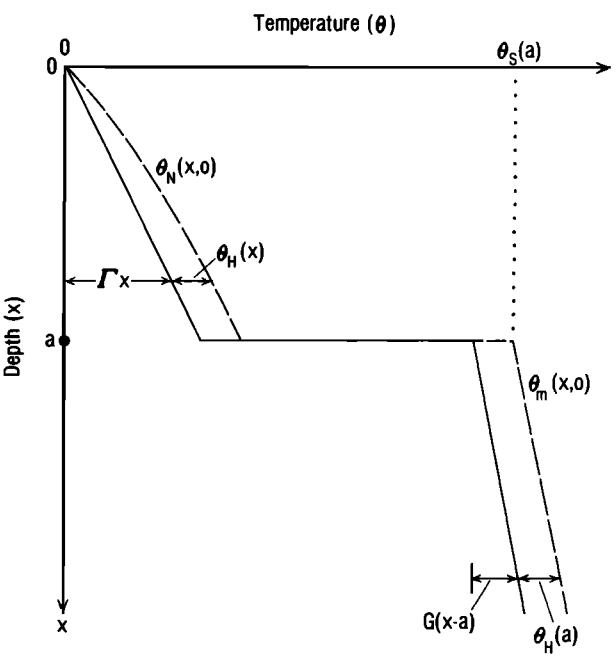

Fig. 25. Dashed curves show temperature at $z = 0+$, Figure 24, the initial condition for model in text. Solid curves show initial temperature with contribution from radioactivity removed.

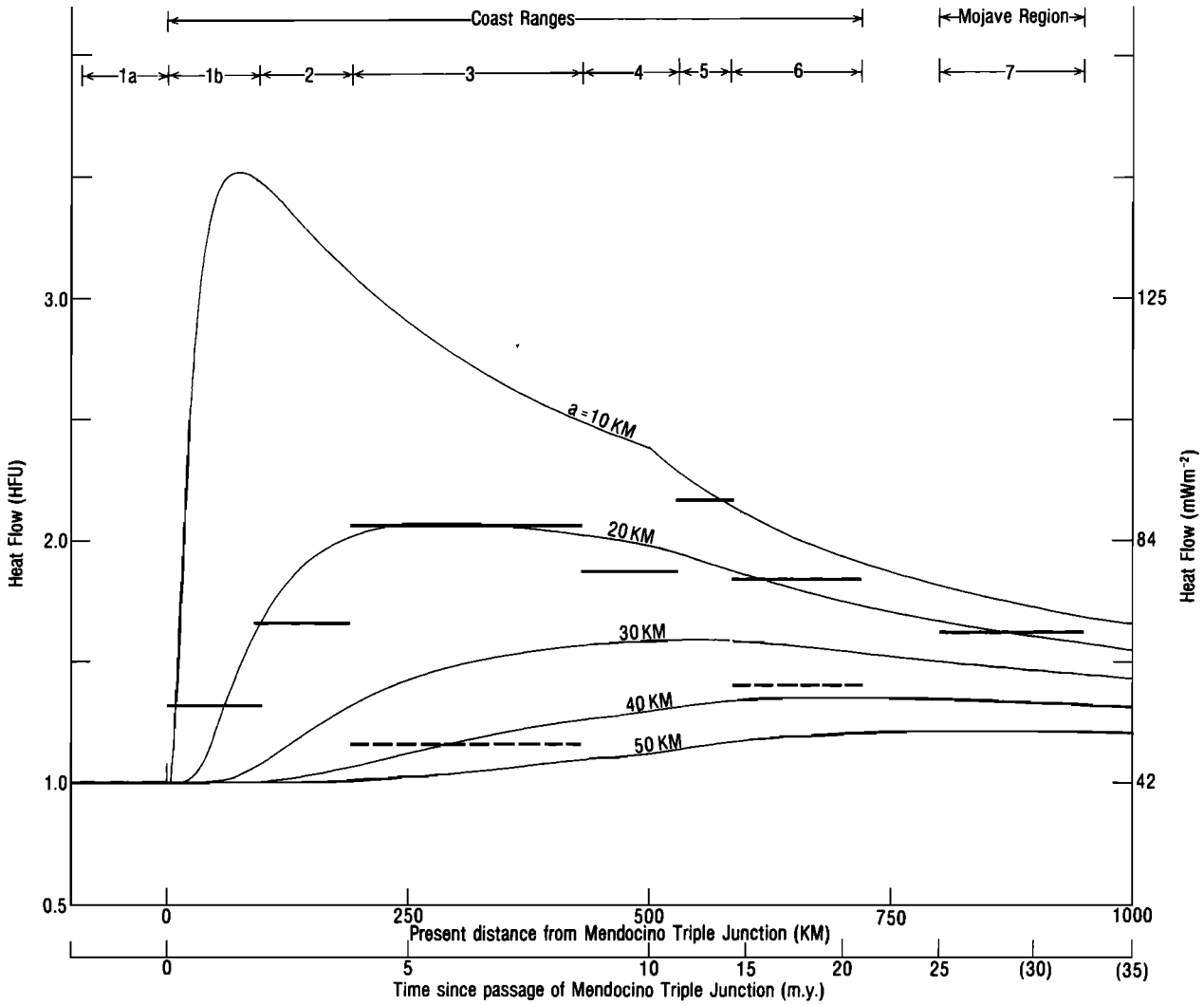

Fig. 26. Heat flow as a function of distance from the Mendocino Triple Junction for selected initial thicknesses a of the North American plate (see Figures 24, 25, and (22)). Horizontal solid lines are mean heat flows in the fault zone for regions delineated in Figure 8. Horizontal dashed lines are mean (corrected) heat flows interior to Great Valley. See text for further explanation.

1. As the North American plate moves southeastward (relative to the Pacific plate) past the projection of the Mendocino transform ($z = 0$, Figure 24), its base at depth $x = a$ (Figure 24) slides from the Gorda plate, cooled by subduction, to a region of warmer mantle material, the northern edge of the 'window' of *Dickinson and Snyder* [1979]. Conduction from this material might supply the anomalous heat provided $a \leq$ 20 km (as required by (48)).

2. A second plausible shallow source of the anomaly is shear-strain heating associated with distortion and possible basal decoupling of the seismogenic layer of the San Andreas fault zone, which originates in the North American plate at this location ($z = 0$, Figure 24).

In an earlier stage of this study [*Lachenbruch and Sass*, 1980] we discounted the first possibility, since we thought it unlikely that the top of the subducting plate would be at mid-crustal depths ($a \leq 20$ km) for distances ~100 km from a trench at the continental margin, and even if it were, low heat flow in the Great Valley would be left unexplained. However, preliminary results from a recent gravity study near Cape Mendocino by Robert Jachens and Andrew Griscom (oral communication, 1980) suggest that the North American plate might presently be thin enough in the Coast Ranges to satisfy this condition. Since an understanding of the nature of the San Andreas fault zone might depend upon a distinction between the relative contributions of these two processes, we shall consider models for each.

Models for Conductive Heating of the Coast Ranges by a Warm Mantle

According to *Dickinson and Snyder* [1979], shortly after the Mendocino Triple Junction contacted North America, the Farallon plate began to disappear beneath the continental margin, leaving a growing triangular region, the 'window,' in which upwelled asthenosphere was left in contact with the original base of the North American plate. The northern edge of the window is the inland projection of the Mendocino transform fault; it moves with the Pacific plate and has not been occupied by a subducting slab for more than 20 m.y. The temperature in the window (region $x > a$, $z > 0$, Figure 24) depends upon the motion within it during that period, and this, in turn, depends upon how the window material has been

coupled to the original North American plate at their interface $x = a$.

We shall consider only the most extreme case of heating which occurs when the mechanical coupling at $x = a$ ($z > 0$) is complete (i.e., no slip); after the plate of thickness a slides off the Gorda plate, it drags the underlying mantle material with it. This would generate a one-sided buried spreading center at the inland projection of the Mendocino transform as illustrated in Figure 24. Upwelling asthenosphere at $z = 0$ would be cooled and accrete to the thickening North American plate as it moved southeastward.

The 'initial' condition (at $z = 0+$, Figure 24) for quasi-one-dimensional conductive cooling is shown by the dashed curves in Figure 25. The temperature $\theta_N(x)$ in the North American plate (of thickness a) is the sum of a steady state contribution $\theta_H(x)$ from radioactivity in the plate and a linear part Γx associated with reduced heat flow. The temperature in the upwelling mantle below a is a linear function, $\theta_m = \theta_s(a) + G(x - a)$, where $\theta_s(a)$ is the mantle solidus (at depth a) given by

$$\theta_s(a) = \theta_s(0) + \gamma a \tag{49}$$

and G is a gradient, artificially introduced to accommodate heat flow from below a. The transient part of the problem involves the solid lines in Figure 25, which are denoted collectively by $\theta_r(x, 0)$; it is the temperature whose (transient) gradient yields the reduced heat flow $q_r(t)$. The radioactive contribution is additive. Thus the initial condition is:

$$\theta_r(x, 0) \equiv \theta(x, 0) - \theta_H(x) = \Gamma x \qquad x < a \tag{50a}$$

$$= \theta_s(0) - (G - \gamma)a + Gx - \theta_H(a) \qquad x > a \tag{50b}$$

The corresponding solution to the differential equation of heat conduction with zero surface temperature is

$$\theta_r(x, t) = \Gamma x + \frac{1}{2}[\theta_s(0) - (G - \gamma)a - \theta_H(a)] \cdot \left[\operatorname{erf}\frac{x + a}{(4\alpha t)^{1/2}} + \operatorname{erf}\frac{x - a}{(4\alpha t)^{1/2}}\right] + \frac{1}{2}(\Gamma - G)a\left\{\frac{x}{a}\left[\operatorname{erf}\frac{x + a}{(4\alpha t)^{1/2}} - \operatorname{erf}\frac{(x - a)}{(4\alpha t)^{1/2}} - 2\right] - \frac{1}{(\pi)^{1/2}}\frac{(4\alpha t)^{1/2}}{h}\left[e^{-[(x-a)^2/(4\alpha t)]} - e^{-[(x+a)^2/(4\alpha t)]}\right]\right\} \tag{51}$$

and the reduced heat flow at time t is given by

$$\frac{q_r(t)}{q_r(0)} = 1 + \left[\frac{\theta_s(0) - \theta_H(a)}{\Gamma h} - \frac{G - \gamma}{\Gamma}\right] \cdot \frac{2}{(\pi)^{1/2}}\frac{a}{(4\alpha t)^{1/2}}e^{-[a^2/(4\alpha t)]} - \left(1 - \frac{G}{\Gamma}\right) \cdot \left[\operatorname{erfc}\frac{a}{(4\alpha t)^{1/2}} + \frac{2}{(\pi)^{1/2}}\frac{a}{(4\alpha t)^{1/2}}e^{-[a^2/4\alpha t)]}\right] \tag{52}$$

Taking the initial reduced heat flow $q_r(0)$ to be the value today at Cape Mendocino (~0.8 HFU) and assuming the steady heat flow from below a to be 0.5 HFU, we obtain

$$\Gamma = 13.3°\text{C/km} \tag{53a}$$

$$G = 8.3°\text{C/km} \tag{53b}$$

where we have used a thermal conductivity K of 6 mcal/cm s °C. In western California, $\theta_H(a)$ is probably small, ~30°C ± 50%. Allowing 15°C for the mean annual surface temperature and assuming the mantle solidus temperature at atmospheric pressure to be 1045°C yields

$$\theta_s(0) - \theta_H(a) \sim 1000°\text{C} \tag{54}$$

We assume further that the solidus gradient γ is 3°C/km and the thermal diffusivitiy α is 0.01 cm²/s.

Equation (52) gives the reduced heat flow at any point in the North American plate at time t after passage of the Mendocino transform (provided the Farallon plate disappeared there first and 'opened the window'). In Figure 26, results are shown for selected initial plate thicknesses a, with the time converted to distance z by assuming the relative velocity of the Pacific and North American plates to have been 5 cm/yr for the past 10 m.y. and 2 cm/yr previously [*Atwater and Molnar*, 1973]. Theoretical reduced heat flows have been increased 0.2 HFU for radioactivity. Horizontal solid lines denote means (Table 2) for the various regions of the fault zone delineated in Figure 8. The two dashed lines denote means for data interior to the Great Valley in regions 3 and 6; these values were adjusted by 0.2 HFU for effects of rapid sedimentation. The mean for the Mojave region is shown only for curiosity; it could not be accommodated by the model for the chronology we have assumed, since its time origin (~30 m.y. B.P.) predates the arrival of the Triple Junction at the continental margin.

It is seen that a simple model of this type fits the Coast Range data (solid lines, Figure 26) fairly well, provided the North American plate thickness a was only about 20 km there while subduction was in progress. The Great Valley data fit an initial plate thickness $a \sim 40$ km (dashed lines, Figure 26). Hence according to the model, the rapid drop in heat flow between the Coast Ranges and Great Valley represents a rapid steepening of subduction there. (This model could be used also to estimate the heat flow at a fixed point on the North American plate following disappearance of the Farallon plate beneath southern and central California; for this purpose a larger initial heat flow might be appropriate; see *Pilger and Henyey* [1979].)

The foregoing model illustrates that extreme conditions (for example, very shallow subduction and a full-fledged spreading center in the mantle at a depth ~20 km) are required to account for the heat flow transition in the Coast Ranges by heat conduction from a warm mantle. The consequences of the model are also extreme (a 'hot line' sweeping northward under the edge of North America), and perhaps they could be confirmed by studies in the Cape Mendocino area. If such conditions do not exist, less extreme warm mantle models would apply, and it is likely that a contribution from shear-strain heating (discussed in the next section) would have to be invoked, at least in the northern Coast Ranges. Less extreme models include those with steeper subduction (for example, $a \gtrsim 30$ km, Figure 26) or those in which the North American plate becomes only weakly coupled to the mantle (at $x = a$) when it passes the Mendocino transform ($z = 0$, Figure 26), thereby requiring less intense divergence and upwelling. (If a should turn out to be even less than 20 km, weaker-coupling models could, of course, account for the anomaly without invoking shear heating.)

Taken literally, the model of Figures 24 and 25 leads to a deep San Andreas fault that penetrates the entire North

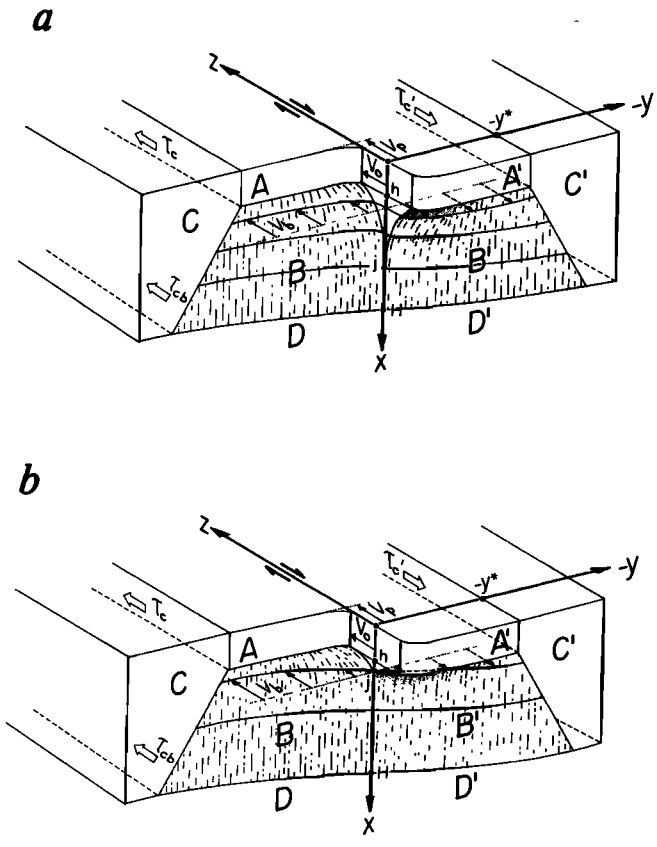

Fig. 27. Steady state models for plate interaction at a transform boundary; C and C′ move with velocity of plate interiors ($\pm v_p$): (*a*) minor decoupling at base of seismogenic layer AA′, (*b*) major decoupling at base of seismogenic layer.

American lithosphere, a reasonable condition during early stages of the fault boundary between thin plates. However, subsequent eastward jumps of the locus of surface faulting [*Atwater and Molnar*, 1973] may be more compatible with continuous deformation across the North America-Pacific plate boundary at depth in the thickening lithospheres, with shallow faulting confined to a superficial brittle layer, partially decoupled at its base. (Shallow decoupling has often been suggested in the past; see, for example, *Anderson* [1971].) Whether or not this is so, it is shown in the next sections that such a superficial fault configuration is probably necessary if shear heating is to contribute appreciably to the Coast Range anomaly without violating the heat flow constraint (13); the model has testable implications for fault zone stresses.

Models for a Mechanical Contribution of Anomalous Heat in the Coast Ranges

If shear heating contributes to the Coast Range anomaly and friction on the fault is negligible, resisting stresses must be appreciable somewhere in the fault zone. Although we do not yet know how large a contribution is required from a frictional source, it is worth investigating the conditions under which it could be appreciable and what they might imply about the mechanics of the fault zone and the resistance to plate motion at a transform plate boundary.

For this purpose, we consider the quasi steady state mechanical models of Figure 27 in which H represents lithosphere thickness and h represents the depth to which slip on the main fault trace is uniform and discontinuous. At some depth j (Figure 27*a*) beneath h, the medium deforms ductilely, and velocity is continuous across the projected plane of the main fault trace $y = 0$. For physical reasons, there must be a transitional layer between h and j; we generally expect h to lie at or beneath the base of the seismogenic layer and j to lie at or above the top of the fluid asthenosphere. Anticipating the problem of accounting for shallow heat sources, in Figure 27*b* we illustrate the extreme case, with h at the base of the seismogenic layer and j only a few kilometers beneath it at the base of a 'partial decoupling layer' with large vertical velocity gradients.

Displacements occur only in the positive and negative z directions, and they are anti-symmetric in y. Hence our reference frame is fixed in space as the primed and unprimed regions move past it in a right lateral sense. Since we are interested in effects of interaction between the primed and unprimed lithosphere plates, we assume the material at great depth to be at rest relative to the reference frame. In the seismogenic layer AA′, in which uniform fault slip is permitted, we assume that v is independent of depth, i.e., plastic deformation or secondary slip can occur only across planes parallel to $y = 0$. We assume further that no distortion of the seismogenic layer occurs beyond $y = \pm y^*$. The regions C and C′ are rigid and move with velocities $\pm v_p$ characteristic of the respective plate interiors. In summary,

$$\frac{\partial v}{\partial x} = \frac{\partial v'}{\partial x} = 0 \qquad x < h \tag{55a}$$

$$v(y) = -v'(-y) \qquad \text{all } x \tag{55b}$$

$$v(y^*) = -v'(-y^*) = v_p \qquad x < h \tag{55c}$$

$$v(0^+) = -v'(0^-) = v_0 \qquad x < h \tag{55d}$$

$$> 0 \qquad x < j \tag{55e}$$

$$= 0 \qquad x \geqq j \tag{55f}$$

$$h < j \leqq H \tag{55g}$$

$$v, v' \to 0 \qquad x \to \infty \tag{55h}$$

In discussing this model, we shall refer only to the unprimed (y positive) portion, with the understanding that the corresponding primed velocities and stresses are equal in magnitude and reversed in sign unless otherwise noted. We shall use the outer normal; tractions that drive the right lateral motion of A are positive, and those that drive right lateral motion of A′ are negative.

The displacements illustrated in Figure 27 are values averaged over times very much longer than the cycle of recurrence of earthquakes. The associated stress state is also a long-term average condition, and it is unchanged by the deformation associated with these velocities. The work done on such a system must be dissipated, and we shall assume that the principal sources of heat and seismic radiation dissipated in the fault zone can be accounted for by a steady model of this kind. If most of the transient effects are elastic and if stress changes during earthquakes are as small as seismic estimates indicate, this should be a useful approximation.

The complex deformation in the region of plate interaction, AA′, BB′, DD′, is a consequence of the vertical variation in failure and deformation characteristics of the outer layers of the earth. The stresses τ_c and τ_{cb} exerted by C on A and B, respectively, are reactions to resistance in the shear zone AA′BB′DD′. We shall assume that the boundaries of C and C′ have been selected so that

$$\tau_c, \tau_{cb} > 0 \tag{56}$$

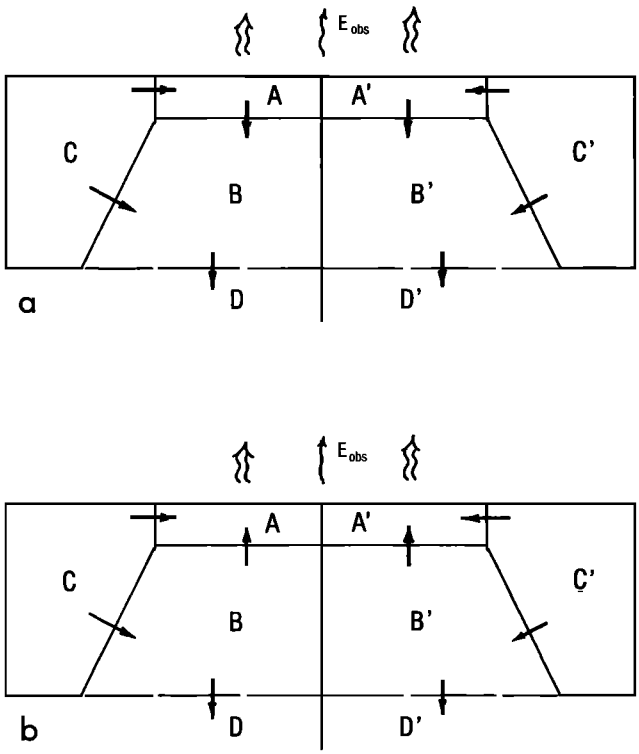

Fig. 28. Major alternatives for flow of mechanical energy in zone of plate interaction: (*a*) subcrust BB′ moves slower (in right lateral sense) than seismogenic layer AA′, which it retards, (*b*) BB′ moves faster than AA′, which it drives. E_{obs} represents loss of heat and seismic radiation energy. Arrows denote the direction of steady flow of energy from one region to another.

and that the neglected basal traction between C and D is unrelated to plate interaction.

We are left with two principal options for the steady flow of mechanical energy into and through the zone of plate interaction (Figure 28). They are distinguished by whether B and B′ drive (Figure 28*b*) or resist (Figures 28*a* and 27) the right lateral motion of A and A′, or equivalently, whether A and A′ are moving slower (Figure 28*b*) or faster (Figure 28*a*) than B and B′ in a right lateral sense. (The 'brittle' model of *Lachenbruch and Sass* [1973] is an example of conditions in Figure 28*a*, and the 'ductile' model is an example of Figure 28*b*.) Condition (56) excludes the possibility that arrows in Figure 28 point from A and B to C.

We denote the shearing traction at the base of A by τ_b and the velocity of A by $v_a(y)$. The velocity a short distance (relative to h) below A will be denoted by $v_b(y)$ (Figure 27). Unless $v_b(y) \equiv v_a(y)$, A will be partially decoupled from the rest of B by this thin zone, and energy will be dissipated within it at the rate $\tau_b(v_b - v_a)$, a positive quantity, because τ_b will have the sign of the velocity difference. According to (48), heat generated in this partial decoupling zone beneath the seismogenic layer might contribute appreciably to the Coast Range anomaly, but heat generated at greater depth (say $\gtrsim$20 km) probably could not. The rate of deformation in this zone may be substantial, with $v_b(y)$ continuous at $y = 0$ (as in Figure 27*b*), or it may be slight, as in Figure 27*a*. Furthermore v_a may be greater or less than v_b, and the sign of their difference could change throughout the half-width y^* of the fault zone. We shall be interested primarily in the following case (illustrated in Figures 27):

$$v_a > v_b \qquad 0 < y < y^* \tag{57a}$$

$$v_a = v_b = v_p \qquad y = y^* \tag{57b}$$

where y^* is the half-width of the fault zone, and the corresponding anti-symmetric relations apply for negative y. For small y, (57*a*) is required if v_b is continuous at $y = 0$ and v_a is not (Figure 27*b*), but the inequality could be reversed for larger y ($< y^*$) if most of the right lateral shearing of B were concentrated in a thin shear zone at $y = 0$, as is often assumed [see, e.g., *Savage and Burford,* 1973; *Hanks,* 1977]. In that case, the seismogenic layer would be driven by the basal stress (Figure 28*b*), a condition that we shall show to be incompatible with the heat flow constraint if there is appreciable heat generation in the fault zone [see also *Lachenbruch and Sass,* 1973].

The fault slip velocity in the seismogenic layer is given by

$$v_0 = v_p - v_a(0^+) \tag{58a}$$

$$v_0' = v_p' + v_a(0^-) \tag{58b}$$

The difference between v_p and v_0 represents inelastic deformation in A (v_p, v_p', v_0, and v_0' are treated as positive quantities.)

The long-term resistance to plate motion offered by the fault at $y = 0$, $x < h$ is the average elastic fault stress τ_e, which in the notation of an earlier section is given by

$$-\tau_e = +\tau_e' = \frac{1}{2}(\tau^* + \tau') \tag{59a}$$

$$= \bar{r} + \tau_a \tag{59b}$$

$$\lesssim 100\, b + \tau_a \tag{59c}$$

We continue to use the apparent stress τ_a and dissipative resistance $\bar{r}$ as positive parameters. Equation (59*b*) expresses the fact that insofar as plate motion is concerned, seismic radiation and frictional heat both represent energy dissipated by the mechanical system.

The average (tensor) component of shearing stress τ_{yz} in A is constrained by the condition of equilibrium:

$$\tau_{yz}(y) = -\tau_e - \frac{1}{h}\int_0^y \tau_b\, dy \tag{60}$$

For purposes of illustration, we shall assume that τ_b is constant, determined by a plastic yield stress; for conditions (57), τ_b is negative, and τ_b' is positive, as in Figure 28*a*. (The case of τ_b proportional to $(v_b - v_a)$ has been discussed by *Lachenbruch and Sass* [1973]; T. C. Lee (personal communication, 1979) has pointed out that a factor of 1/2 is missing before the braces of equation 7 in that paper.) With this simplification, (60) yields

$$\tau_{yz}(y) = -\tau_e - \frac{y}{h}\tau_b \tag{61a}$$

and at $y = y^*$,

$$\tau_c = -\tau_e - \frac{y^*}{h}\tau_b \tag{61b}$$

Thus if τ_b is positive (Figure 28*b*), the greatest shearing stress in the seismogenic layer occurs on the fault and the least on the periphery; if τ_b is negative (Figure 28*a* and Figures 27), the minimum occurs at the fault and the maximum at the periphery.

Energetics of Plate Interaction

Let E_T be the total rate of energy dissipation per unit length at a symmetrical transform plate boundary, and let R_T be the

corresponding resistance (per vertical unit area) to plate motion. Then for an antisymmetric shear zone,

$$E_T = 2hv_p\tau_c + 2\int_{CB} \tau_{cb}v_p\, ds \tag{62a}$$

$$= 2Hv_pR_T \tag{62b}$$

where the integral is taken over the boundary between C and B, and τ_{cb} is the traction there. Application of (56) yields a lower limit to plate resistance:

$$R_T > \frac{h}{H}\tau_c \tag{63}$$

Let E_{obs} be the sum of the 'observable' losses of mechanically generated heat and seismic radiation energy. Assuming all of the seismic energy originates on the main fault trace, we have

$$E_{obs} = 2y^*\overline{\Delta q} + 2hv_0\tau_a \tag{64a}$$

$$= 2hv_pR_{obs} \tag{64b}$$

where $\overline{\Delta q}$ is the average value of the mechanically generated part of the broad heat flow anomaly, and R_{obs} is the resistance to plate motion that is, in principle, observable from studies of heat flow and earthquakes:

$$R_{obs} \equiv \frac{y^*}{h}\frac{\overline{\Delta q}}{v_p} + \frac{v_0}{v_p}\tau_a \tag{64c}$$

Since the portion of E_T generated deep within the lithosphere cannot contribute to E_{obs}, (62*b*) and (64) yield a second lower limit to plate resistance:

$$R_T > \frac{h}{H}R_{obs} \tag{65}$$

According to (48), E_{obs} should be approximately equal to the net rate at which work is done on the seismogenic layer plus the underlying decoupling layer after a few million years of transform faulting. If we assume v_b is continuous at $y = 0$ (as in Figure 27*b*), then

$$E_{obs} \cong 2hv_p\tau_c + 2\int_0^{y^*} v_b\tau_b\, dy \tag{66a}$$

$$\cong 2hv_p\tau_c + 2y^*\,\overline{v}_b\tau_b \tag{66b}$$

where $\overline{v}_b$ is the average value of v_b, and we have assumed τ_b to be constant.

Combining (64) and (66) yields the energy balance for the seismogenic and decoupling layers:

$$hv_p\tau_c = y^*\overline{\Delta q} + hv_0\tau_a - y^*\overline{v}_b\tau_b \tag{67a}$$

$$\tau_c = \frac{y^*}{h}\frac{\overline{\Delta q}}{v_p} + \frac{v_0}{v_p}\tau_a - \frac{y^*}{h}\frac{\overline{v}_b}{v_p}\tau_b \tag{67b}$$

$$= R_{obs} - \frac{y^*}{h}\frac{\overline{v}_b}{v_p}\tau_b \tag{67c}$$

The term on the left in (67*a*) is work done by the plate in driving the seismogenic layer; the first two terms on the right are the heat and seismic radiation that leave the system, and the last term is work done by the decoupling zone on the underlying crust if τ_b is negative (Figure 28*a*) or on the decoupling zone by the underlying crust if τ_b is positive (Figure 28*b*). It is seen from (67*c*) that the sign of τ_b determines whether τ_c is greater or less than R_{obs}, and consequently, whether (63) or (65) imposes a stronger condition on resistance to plate motion.

Combining (59*c*), (61*b*), and (67*a*), we can now express the heat flow constraint (13) as follows:

$$0 < \bar{r} = \frac{y^*}{h}\frac{\overline{\Delta q}}{v_p} - \left(1 - \frac{v_0}{v_p}\right)\tau_a + \frac{y^*}{h}\left(1 - \frac{\overline{v}_b}{v_p}\right)\tau_b \lesssim 100 \text{ bars} \tag{68}$$

For the Coast Ranges we select the following values:

$$\left.\begin{aligned} 2v_p &= 5 \text{ cm/yr} \\ 2v_0 &= 3 \text{ cm/yr} \end{aligned}\right\} \quad \frac{v_0}{v_p} = 0.6$$

$$\left.\begin{aligned} h &= 14 \text{ km} \\ 2y^* &= 84 \text{ km} \end{aligned}\right\} \quad \frac{y^*}{h} = 3 \tag{69}$$

which leads to the following relation (see (10)):

$$0 < \bar{r}\,[\text{bars}] = 910\overline{\Delta q}\,[\text{HFU}] - 0.4\tau_a + 3\left(1 - \frac{\overline{v}_b}{v_p}\right)\tau_b \leqq 100$$

where stresses are expressed in bars. If the basal stress τ_b vanished, a large heat flow contribution would require a very large apparent stress (~2 kbar/HFU); if τ_b were positive (Figure 28b), τ_a would have to be larger still. Hence a substantial heat flow contribution from the shear zone would seem to imply basal drag on the seismogenic layer (i.e., τ_b negative, as in Figures 27 and 28*a*). This requires that the minimum shearing stress in the seismogenic layer be the value at the main fault and the maximum be the value at the periphery τ_c (61).

Using the equilibrium relation (61) and the energy balance (67), we can express the basal and peripheral stresses on the seismic layer in terms of heat flow and the fault stresses (τ_a and $\bar{r}$) as follows:

$$-\tau_b = \left[1 - \frac{\overline{v}_b}{v_p}\right]^{-1}\left\{\frac{\overline{\Delta q}}{v_p} - \frac{h}{y^*}\left[\left(1 - \frac{v_0}{v_p}\right)\tau_a + \bar{r}\right]\right\} \tag{70a}$$

$$= \left[1 - \frac{\overline{v}_b}{v_p}\right]^{-1}\{303\overline{\Delta q}\,[\text{HFU}] - 3[0.6\tau_a + \bar{r}]\} \tag{70b}$$

$$\tau_c = \left[1 - \frac{\overline{v}_b}{v_p}\right]^{-1}\left\{\frac{y^*}{h}\frac{\overline{\Delta q}}{v_p} - \left(\frac{\overline{v}_b}{v_p} - \frac{v_0}{v_p}\right)\tau_a - \frac{\overline{v}_b}{v_p}\bar{r}\right\} \tag{71a}$$

$$= \left[1 - \frac{\overline{v}_b}{v_p}\right]^{-1}\left\{910\overline{\Delta q}\,[\text{HFU}] - \left(\frac{\overline{v}_b}{v_p} - \frac{3}{5}\right)\tau_a - \frac{\overline{v}_b}{v_p}\bar{r}\right\} \tag{71b}$$

where stress is in bars in the dimensional forms, which incorporate (69). It is seen that these stresses are very sensitive to the ratio $(\overline{v_b}/v_p)$ of the average speed of the base of the decoupling layer to the speed of the rigid plates.

For convenience, we represent v_b by

$$v_b = v_p\left(\frac{y}{y^*}\right)^n \qquad n > 0 \tag{72a}$$

from which it follows that

$$\frac{\overline{v}_b}{v_p} = \frac{1}{n+1} \tag{72b}$$

Small n implies large right lateral velocities in the subcrust, and large n implies small ones, a condition generally associ-

ated with substantial decoupling of the seismogenic layer (the amount depending on the form of $v_a(y)$). This relation is illustrated in Figure 29 where v_b is shown for $n = 1/2$, 1, and 2. The solid curve labeled $v_a v_a'$ represents motion of the seismogenic layer for a central fault. As we have assumed τ_b to be constant, the form of $v_a(y)$ enters the analysis only through its effect on the sign of τ_b (which is the sign of $v_b(y) - v_a(y)$) and on the fault slip v_0.

The least value of τ_c occurs in the physically unrealistic case of complete decoupling $\bar{v}_b = 0$, which leads to

$$\tau_c > 910\overline{\Delta q}\ [\text{HFU}] + 0.6\tau_a \equiv R_{\text{obs}} \tag{73}$$

where stress is in bars. The greatest value of τ_c occurs with complete coupling at the base of the seismogenic layer, i.e., $\bar{v}_b \cong \bar{v}_a$. Judging from the measurements of *Thatcher* [1959] in the Coast Ranges, $\bar{v}_a/v_p \sim 0.8$–0.9, which leads to (71*b*)

$$\tau_c\ [\text{bars}] \sim (5\text{–}10 \times 910\overline{\Delta q}\ [\text{HFU}] \tag{74}$$

Hence in the absence of decoupling, appreciable heat generation would require peripheral stresses of several kilobars. If the average speed at the base of the decoupling layer were 1/2 plate velocity ($n = 1$, Figure 29), a condition that would represent substantial decoupling in the Coast Ranges, peripheral stresses are still large for modest heat flow contributions. It is clear from (71) that the permissible amount of mechanically generated heat will be limited by the condition that the peripheral stress τ_c not exceed the strength of upper crustal rocks; the stress is insensitive to τ_a and hence to whether the fault is weak always or only during earthquakes. The required basal stress (70) is generally less than the peripheral stress by a factor $\sim 1/3$, becoming somewhat smaller for larger τ_a.

Rearranging (71*a*), we can express the heat flow anomaly by

$$\overline{\Delta a} = \frac{h}{y^*} v_p \left\{ \tau_c \left[1 - \frac{\bar{v}_b}{v_p} \right] + \tau_a \left[\frac{\bar{v}_b}{v_p} - \frac{v_0}{v_p} \right] + \bar{r} \frac{\bar{v}_b}{v_p} \right\} \tag{75}$$

Taking an upper limit for rock strength under normal fluid pressure of 1.5 kbar (Table 4), the maximum permissible contribution of mechanically derived heat in the Coast Ranges is

$$\overline{\Delta q}\ [\text{HFU}] = 0.65 \left\{ 1.5 \left[1 - \frac{\bar{v}_b}{v_p} \right] + \tau_a \left[\frac{\bar{v}_b}{v_p} - \frac{3}{5} \right] + \bar{r} \frac{\bar{v}_b}{v_p} \right\} \tag{76a}$$

$$\sim \left[1 - \frac{\bar{v}_b}{v_p} \right] [\text{HFU}] \tag{76b}$$

where stress is in kilobars. This yields 0.5 HFU for conditions illustrated by $n = 1$ (equation (72), Figure 29), 0.33 HFU for $n = 1/2$, and 0.1–0.2 HFU for complete coupling ($n \sim 1/4 - 1/5$). Thus, unless most of the plate motion in the interplate shear zone is confined to the seismic layer (i.e., roughly, unless $n > 1$), it is unlikely that shear heating can account for more than about half of the steady state heat flow anomaly in the Coast Ranges. Even this amount of heating requires substantial decoupling at the base of the layer and large stresses at the periphery of the shear zone.

These results raise questions about stress conditions on peripheral faults. In deriving them, we assumed that all of the seismic energy was generated on the principal central fault, equivalent to assuming that the heat-generating stress on minor peripheral faults is the average ambient tectonic stress there. Implications of a broad mechanically generated heat flow anomaly for stress conditions on minor peripheral faults will depend upon more detailed considerations of apparent stress and dynamic friction on such faults and their possible observable seismic and geothermal consequences. If the principal interplate slip should occur at the periphery of the shear zone, the high stresses required by the central fault would not be eliminated; they would only be moved elsewhere [see *Lachenbruch and Sass*, 1980]. For the symmetrical peripheral faults illustrated by the dashed curve $v_a v_a'$, Figure 29, the central stress (at $y = 0$) is the same as the peripheral stress τ_c (at $y = \pm y^*$) for the corresponding central fault provided n is replaced by its reciprocal; under these conditions, the magnitudes of the basal stresses are also the same. For a single peripheral fault (at $y = -y^*$), Figure 30, which approximates conditions at the southern end of the Coast Ranges, the stress at the opposite side of the shear zone ($y = +y^*$, Figure 30) is the same as that for the corresponding central fault (i.e., with the same n), but the basal stress is reduced by a factor of $\frac{1}{2}$. In each of these cases, the basal stress opposes right lateral motion on the fault(s), for otherwise, the heat flow constraint would be violated.

Hence no matter where in the shear zone the principal faults are located, an appreciable mechanical contribution to the broad heat flow anomaly is possible only if the average shear stress in the seismogenic layer increases rapidly with distance from the fault(s), a testable consequence. Decoupling at the base of the faulted blocks would generally be in the sense that resists their right lateral motion. Under these conditions, the unobserved maximum stress away from the fault(s) (τ_c for the central fault) would determine the resistance offered by the seismogenic layer to plate motion. If there is an appreciable heat flow contribution, this resistance will generally be substantially larger than R_{obs} (68) estimated from measurements of seismic radiation and heat flow. The unobserved dissipated energy represents work done by the decoupling layer on the material beneath it.

The Form of the Heat Flow Anomaly; Independence of Distance From the Fault

The foregoing discussion of energetics does not address the details of the heat production process nor, indeed, whether models of the type considered could reasonably contribute a broad uniform heat flow anomaly throughout the fault zone, such as the data from the California Coast Range suggest.

The heat flow anomaly $\Delta q(y)$, discussed only as an average $\overline{\Delta q}$ in the last section, can be viewed as the sum of three contributions [see *Lachenbruch and Sass*, 1973]:

$$\Delta q(y) \cong q_{yz}(y) + q_b(y) + q(y) \tag{77}$$

For convenience, we consider again the centrally faulted antisymmetric shear zone, for which it is only necessary to describe the y positive side. The terms in (77) can be expressed as

$$q_{yz}(y) = h\tau_{yz} \frac{dv_a}{dy} = -h \left[\tau_e + \frac{y}{h} \tau_b \right] \frac{dv_a}{dy} \tag{78a}$$

$$q_b(y) = -\tau_b(v_a - v_b) \tag{78b}$$

$$\int_0^{y^*} q\, dy = \bar{r} v_0 \tag{78c}$$

Here, q_{yz} is the rate of heat generation per horizontal unit area resulting from inelastic distortion of the seismogenic layer (for

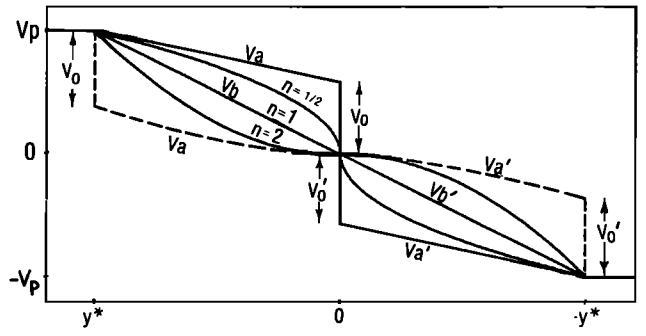

Fig. 29. Velocity of seismogenic layer shown for a central fault (solid curve v_a, v_a') and symmetrical peripheral faults (dashed curve v_a, v_a') with three different velocity distributions v_b, v_b' at base of decoupling layer.

example, by plastic flow or subsidiary faulting), q_b is the rate of heat generation by flow in the hypothetical decoupling layer beneath the seismogenic layer, and q is heat generated by friction on the main fault trace, discussed in detail in an earlier section. In (78*a*) and (78*b*) we have neglected conductive smoothing between the source and the surface, justified by the approximate nature of the calculation and the fact that the depth of the sources ($x \lesssim h$) is small relative to the width of the shear zone ($2y^* \sim 6h$).

From (78*a*) it is seen that computation of the form of the heat flow contribution requires information on the distortion of the seismogenic layer not required in the calculation of energy balance. The heat flow anomaly is more sensitive also to the y dependence of v_b, formerly entering the analysis as an average, and of τ_b, which we have assumed to be constant. Reasonable assumptions regarding the forms of $v_a(y)$ and $v_b y)$, and of τ_b, which will depend upon them both, must come from an analysis of the controlling constitutive relations, an effort beyond the scope of this study. (Substantial decoupling near the base of the seismogenic layer will probably require effective viscosities $\lesssim 10^{22}$ P at temperatures ~750°K, conditions that might be compatible with 'wet quartzite' and 'limestone' but not the other media discussed by *Yuen et al.* [1978].) Without pursuing unwarranted refinements, we present only one simple example to illustrate some general points.

We have shown (61) that for τ_b positive, τ_{yz} increases as the central fault is approached, and from (78*a*) and (78*b*) it is seen that both q_{yz} and q_b would generally tend to contribute to a heat flow maximum (not observed) at $y = 0$. For τ_b negative (Figure 28*a*), the two contributions tend to vary in opposite senses, and τ_{yz} is a minimum at the fault. Hence a uniform heat flow anomaly is consistent with a relatively weak fault. This is illustrated for a simple model with linear v_a and v_b in which $v_a > v_b$ and hence τ_b is negative (v_a, v_a' is the solid curve in Figure 29, and v_b, v_b' is the curve $n = 1$):

$$v_a = v_0 + (v_p - v_0)\frac{y}{y^*} \tag{79a}$$

$$v_b = v_p \frac{y}{y^*} \tag{79b}$$

From (66),

$$\Delta q - q = q_{yz} + q_b$$

$$= -\frac{h}{y^*}(v_p - v_0)\left(\tau_e + \frac{y}{h}\tau_b\right) - \tau_b v_0\left(1 - \frac{y}{y^*}\right) \tag{80a}$$

$$= -\frac{h}{y^*}(v_p - v_b)\tau_e - v_0\tau_b - \frac{y}{y^*}(v_p - 2v_0)\tau_b \tag{80b}$$

which results in the desired uniform anomaly (independent of y) if the slip velocity v_0 is half the plate velocity v_p (80*b*). There is a triangular minimum at $y = 0$ if the slip velocity is faster than half the plate velocity and a maximum if it is slower. The possibility of a minimum in $q_{yz} + q_b$ raises the question of whether this might 'hide' a more substantial contribution from fault friction q than we have acknowledged in deriving the heat flow constraint ((13) and (38)) [see *Lachenbruch and Sass,* 1973]. In any case, the local anomaly could not exceed the total broad anomaly of about 0.8 HFU, a condition that would relax the constraint on fault friction to

$$\bar{\tau} \lesssim 400 \text{ bars} \tag{81}$$

However, such a minimum requires rather special conditions, and the absence of an observable local anomaly in the contrasting tectonic and thermal regimes of northern and southern California makes this alternative extremely unlikely.

SUMMARY

We have summarized heat flow data from more than 100 sites within about 100 km of the San Andreas fault in California. From these measurements we have made three generalizations, the mechanical implications of which we have attempted to interpret:

1. There is no measurable local heat flow anomaly along the 1000-km length of fault trace (Cape Mendocino to San Bernardino) from which measurements are available.
2. The heat flow is anomalously high (~2 HFU, ~80 mW m^{-2}) throughout the southern 550 km of the Coast Ranges, a region that encloses the San Andreas fault in central California.
3. This broad Coast Range anomaly falls off rapidly toward the Great Valley to the east, and northwestward over a 200-km distance to Cape Mendocino.

The first generalization (first discussed by *Brune et al.* [1969]) imposes a severe constraint on the local energetics of the main fault, and the second and third might contain information on the energetics of plate interaction and the mechanical behavior of the broad shear zone.

The importance of generalization 1 to the mechanics of

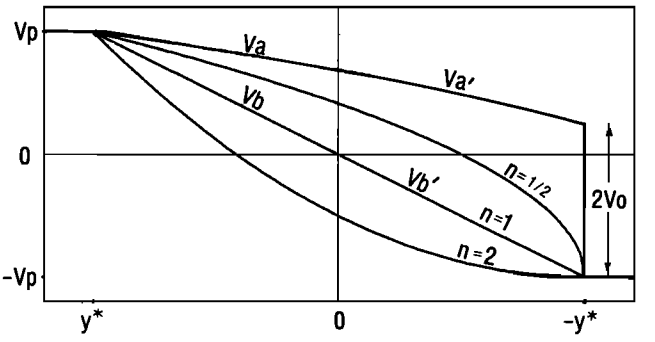

Fig. 30. Velocity of seismogenic layer v_a, v_a' for a one-sided peripheral fault and three different velocity distributions v_b, v_b' at base of decoupling layer.

faulting depends upon the applicability of two conditions: (1) heat transfer near the fault is primarily by conduction, and (2) work done against resisting forces on the fault surface is dissipated primarily as heat. If both conditions apply, then generalization 1 implies that during events responsible for the preponderance of fault motion, the average (instantaneous) resisting stress on the fault surfaces did not exceed ~100 bars; we refer to this limit as the 'heat flow constraint.' If heat were removed convectively by water circulating in the fault zone (in violation of condition (1)), much larger resisting stresses would be permissible. However, we consider this unlikely, because the heat discharge of thermal springs near the fault is negligible and heat flows are similar on each side of the fault, but hydrologic conditions probably contrast sharply. Undetected heat discharge into surface drainage at temperatures slightly above ambient is a possibility that may deserve further study. Larger resisting stresses are permissible also if much of the energy dissipated in overcoming them is consumed by creating new surfaces or by other energy sinks (in violation of condition 2). Our estimate (based on specific surface energies from *Brace and Walsh* [1962] and an average three-dimensional fracture spacing of 1 micron in the gouge zone) suggests that conversion of work to surface energy is too small by 2 orders of magnitude to affect the heat flow constraint. There is, however, a large uncertainty in the rate of creation of surface area in gouge by faulting. Other possible energy sinks such as chemical and metamorphic reactions should be investigated, although we consider it unlikely that they will invalidate the heat flow constraint. Our interpretations are based on the assumption that the constraint is valid.

The heat flow constraint provides an upper limit (~100 bars) to the average dynamic frictional resistance that obtained during those events responsible for most of the slip on the San Andreas fault; this probably excludes small earthquakes and isolated creep episodes lasting no more than 10,000 yr. The importance of the constraint lies in the information it provides on the ambient tectonic stress state. If almost all of the slip took place by steady uniform creep, the implications are straightforward; the resolved tectonic shear stress on the fault could not, on the average, have exceeded ~100 bars and consequently, tectonic stress differences could not have exceeded a few hundred bars.

If, however, most of the displacement occurred during earthquakes, it is the initial stress prior to the event, not the frictional stress during the event, that indicates the ambient state of tectonic stress. The relation between the two is most easily discussed in terms of the frictional theory of faulting wherein the initial stress is bounded above by the static frictional strength and bounded from below by the dynamic friction. The frictional strength is given approximately by the product of the coefficient of static friction and the ambient effective normal stress on the fault; the average dynamic friction (constrained by the heat flow) is the product of the coefficient of dynamic friction and the (displacement averaged) effective normal stress while faulting is in progress. The implications of the heat flow constraint are different depending upon whether or not the ambient effective normal stress persists unchanged during the faulting event, i.e., upon whether the fault is weak all the time or only during an earthquake.

If the effective normal stress is the same before and during an earthquake, then the initial stress will not exceed the dynamic frictional stress by a factor greater than the ratio of the static and dynamic coefficients of friction, a quantity that is probably of order unity (we have used 4/3). In this case, the frictional strength and the resolved tectonic (i.e., initial) shear stress can be only slightly greater than the ~100 bars permitted by the heat flow constraint, and the tectonic stresses cannot be significantly greater than those permitted for steady state creep. Such low frictional stresses, are, however, less by an order of magnitude than those expected from laboratory results (Byerlee's law) in upper crustal rocks with normal (hydrostatic) fluid pressures. This strength paradox can be resolved by postulating that the fault contains materials with anomalously low static and dynamic friction (for example, hydrated clay minerals) or that near the fault the ambient fluid pressures are near lithostatic and, consequently, the effective normal stress is very small. At present, however, there is little independent evidence that either of these conditions occur generally on the San Andreas fault. The paradox cannot be resolved by explanations of low strength that do not also explain low dynamic friction. For example, the strength of small laboratory samples might be much greater than the strength of a large heterogeneous fault because of the greater probability of the juxtaposition of randomly distributed flaws and local stress concentrations on the latter. This does not explain the low average dynamic frictional resistance implied by the heat flow constraint. The paradox could, of course, be resolved without contradicting laboratory results, or by assuming a changing effective normal stress, if the ratio of the coefficients of static to dynamic friction were an order of magnitude greater than we have supposed. However, this alternative runs into the same observational difficulty as the ones we shall next discuss.

If the average effective normal stress were an order of magnitude less during an earthquake than it was before the earthquake, then the heat flow constraint would be consistent with strengths on the order of ~1 kbar (as suggested by laboratory results for upper crustal rocks with normal fluid pressure) and with ambient tectonic stress differences of a few kilobars. There are several plausible physical mechanisms that might cause such large transient reductions in effective normal stress. The fluid pressure might increase during an earthquake as a result of frictional heating and thermal expansion of pore fluid or by reduction of pore volume or dehydration of clay minerals [*Lachenbruch,* 1980; *Sibson,* 1973; *Raleigh,* 1977], or perhaps the effective normal stress could be reduced dynamically by 'acoustic fluidization,' as recently suggested by *Melosh* [1979]. However, models of this kind are constrained by implications from seismology for the energetics of the earthquake process. The work done by local elastic forces during an earthquake must be accounted for by heat and seismic radiation energy. Stated another way, the average elastic stress operating during an earthquake is the sum of a part allocated to the production of heat (the dynamic frictional resistance) and a part allocated to the production of seismic energy (the 'apparent stress'). It is known from seismic studies of many crustal earthquakes that the initial stress cannot exceed the average elastic stress by more than a few tens of bars (half the 'stress drop'). Hence to a few tens of bars the initial (resolved tectonic) shear stress cannot exceed the frictional resistance (constrained by heat flow to be $\lesssim$100 bars) by more than the magnitude of the apparent stress. Hence models leading to an initial stress of ~1 kbar require that the apparent stress be of similar magnitude; they are inconsistent with seismic estimates of apparent stress, which are generally $\lesssim$50 bars. Consequently, large ambient tectonic shear stresses on the fault are not permitted by the heat flow constraint unless the seis-

mic estimates of apparent stress (and hence of total radiated energy) are very much in error for those earthquakes responsible for most of the cumulative displacement, probably the very large ones. If we take the thermal and seismic observational constraints at face value, it is difficult to justify average tectonic shearing stresses on the fault much in excess of ~200 bars.

In addition to these implications for the stress regime in the immediate vicinity of the fault, the heat flow constraint has implications for stresses in the broad shear zone surrounding the fault when it is applied to interpretation of the broad Coast Range heat flow anomaly. The growth of this broad anomaly southward from Cape Mendocino (generalizations 2 and 3) may be interpreted as the transient effect of the change in thermal conditions that took place at the migrating Triple Junction when subduction gave way to transform faulting. Since the transition to the high heat flow characteristic of the Coast Range is complete ~200 km southeast of Cape Mendocino and since the Triple Junction has been migrating northwestward ~50 km/m.y., this suggests that a steady state is reached in ~4 m.y. and, consequently, that the sources of the anomaly are in the mid- and upper crust (≲20 km). This conclusion is consistent with the rapid fall-off of heat flow toward the Great Valley to the east. There are two simple processes that might account for the anomalous observed heat flow: (1) conductive heating of the North American plate from below when it passes southward from a region in which its base is in contact with a cool subducting slab to a region in which it contacts warmer mantle material; (2) shear-strain heating associated with distortion and possible basal decoupling of the seismogenic layer of the San Andreas fault zone which originates near the Mendocino Triple Junction. An understanding of the nature of the San Andreas fault might depend upon a distinction between the relative contributions of these two processes.

To explain the heat flow transition by the first process without a contribution from shear heating, extreme conditions are necessary, for example, shallow subduction at a depth of only 20 km beneath the Coast Ranges and complete coupling of the North American plate to the underlying mantle when subduction stops. This would result in a buried one-sided spreading center migrating northward (with the Mendocino transform) as a 'hot line' beneath western North America. The lithosphere beneath the Coast Ranges would thicken southward (from 20 km near Cape Mendocino today) by thermal accretion. Taken literally, the model leads to a deep San Andreas fault penetrating the entire lithosphere; it is too simple to account for the inland migration of the locus of surface faulting. Nevertheless, it accounts reasonably well for the distribution of observed heat flow; the rapid transition toward the Great Valley could be accommodated by a rapid steepening of subduction to 40 km (from 20 km beneath the Coast Ranges). If field evidence for extreme conditions of the sort implied by this model cannot be found, it is likely that an appreciable contribution from shear-strain heating will have to be invoked. Although this requirement is speculative at present, it is of interest to consider its implications, when taken with the heat flow constraint, for the mechanics of the fault zone and plate interaction.

We considered models in which the anomalous heat is generated in a broad shear zone (corresponding to the Coast Ranges) by distortion in the seismogenic layer (~14 km thick) combined with a possible contribution from shear flow in a horizontal partial decoupling layer at its base. According to the foregoing interpretation of generalizations 2 and 3, mechanical work in this region must account for the contribution to anomalous heat loss in the Coast Ranges and for seismic energy radiated from the fault(s). Insofar as the tectonic plates are concerned, both of these forms of energy are dissipated and are associated with resistance to plate motion. We identified these losses with the work done by the long-term average stresses operating through the long-term average velocities at the boundaries of this region (the seismogenic layer plus the hypothetical underlying decoupling layer). We found that in order to generate an appreciable heat flow contribution without violating the heat flow constraint on the main fault, it is necessary that the (steady state) basal traction on the seismogenic layer be in the sense that resists (not drives) right lateral fault motion. Under these circumstances, the shearing stress on planes parallel to the fault in the seismogenic layer is a minimum on the main fault and a maximum at the periphery of the fault zone. The maximum permissible mechanically generated heat flow anomaly is limited by how large these peripheral stresses may be and by the amount of decoupling near the base of the seismogenic layer. If the peripheral stresses are limited by the strength of upper crustal rocks with normal fluid pressure (~1.5 kbar), then the mechanical contribution to the broad heat flow anomaly probably could not exceed 0.1–0.2 HFU unless the seismogenic layer were partially decoupled from the underlying crust at its base. If the average right lateral velocity of the base of the decoupling layer were about ½ plate velocity, shear heating could probably account for about ½ of the steady state heat flow anomaly in the Coast Ranges (~0.5 HFU). These results are rather insensitive to the stress allocated to seismic radiation (τ_a), and hence they apply whether the fault is weak all the time or only during earthquakes. Similar results apply to a fault zone containing more than one fault. Hence according to this simplified model, an appreciable mechanical contribution to the broad heat flow anomaly should be associated with a rapid increase in mean shearing stress with distance from the principal fault(s), a testable consequence. If heat generation is significant, the seismogenic layer could offer appreciable resistance to plate motion even though stress on the main fault were negligible; the principal resisting surface would be the horizontal base of the seismogenic layer.

APPENDIX A: GROSS CONDUCTIVE EFFECTS OF FRICTIONAL HEAT FROM A VERTICAL STRIKE SLIP FAULT

We consider effects in the half-space $x > 0$ of heat conducted from a vertical distribution of sources of strength $Q(x)$ commencing at $t = 0$ on the fault plane $y = 0$. The medium is initially at zero temperature, and the surface $x = 0$ is maintained at zero temperature (Figure 1).

A general expression for temperature θ is obtained by integration of the transient result for continuous horizontal line sources lying in the fault plane [*Carslaw and Jaeger*, 1959, p. 261, equation 5].

$$\theta(x, y, t) = \frac{1}{4\pi k}\int_{x_1}^{x_2}\left[-E_i\left(-\frac{y^2 + (x' - x)^2}{4\alpha t}\right) + E_i\left(-\frac{y^2 + (x' + x)^2}{4\alpha t}\right)\right] Q(x')\,dx' \qquad \text{(A1)}$$

where the second term in the integral represents a negative image source as required to meet the zero-temperature condition on $x = 0$.

The Case of Constant Source Strength in the Depth Range (x_1, x_2)

For this case, $Q(x) = Q_c$, a constant, where $x_1 \le x \le x_2$, and $Q(x) = 0$, where $0 < x < x_1$, $x_2 < x$. A change of variables in (A1) leads to

$$\frac{4\pi k}{Q_c}\theta(x, y, t) = \sqrt{4\alpha t}\left\{\int_{(x_1+x)/(4\alpha t)^{1/2}}^{(x_2+x)/(4\alpha t)^{1/2}} - \int_{(x_1-x)/(4\alpha t)^{1/2}}^{(x_2-x)/(4\alpha t)^{1/2}} E_i \cdot [-(m^2+\beta^2)]\, d\beta\right\} \quad \text{(A2)}$$

where

$$m^2 = y^2/(4\alpha t) \quad \text{(A3)}$$

The integral in (A2) may be integrated as follows:

$$\int_a^b E_i(-m^2-\beta^2)\, d\beta = [bE_i(-m^2-b^2) - aE_i(-m^2-a^2)] - \int_a^b \beta d[E_i(-m^2-\beta^2)] \quad \text{(A4)}$$

The integral on the right in (A4) may be written

$$-2\int_a^b e^{-m^2-\beta^2}\frac{\beta^2}{m^2+\beta^2}\, d\beta = -2\int_a^b e^{-m^2-\beta^2} d\beta + 2\int_a^b e^{-m^2-\beta^2}\frac{m^2}{m^2+\beta^2}\, d\beta \quad \text{(A5)}$$

but

$$-2\int_a^b e^{-m^2-\beta^2}\, d\beta = -e^{-m^2}\sqrt{\pi}\,[\operatorname{erf} b - \operatorname{erf} a] \quad \text{(A6)}$$

and

$$2\int_a^b e^{-m^2-\beta^2}\frac{m^2}{m^2+\beta^2}\, d\beta = 2\pi m\left[S\left(\frac{b}{m}, m\right) - S\left(\frac{a}{m}, m\right)\right] \quad \text{(A7)}$$

where the function S is described below. Applying (A4), (A5), and (A6) to (A2) yields the desired general result for the transient temperature rise in the half-space:

$$\theta(x, y, t) = \frac{Q_c}{4\pi k}[F(x_2+x; y, t) - F(x_1+x; y, t) - F(x_2-x; y, t) + F(x_1-x; y, t)] \quad \text{(A8}a\text{)}$$

where

$$F(a; y, t) = aE_i\left(-\frac{y^2+a^2}{4\alpha t}\right) - \sqrt{4\pi\alpha t}\, e^{-y^2/(4\alpha t)} \operatorname{erf}\frac{a}{(4\alpha t)^{1/2}} + 2\pi y S\left(\frac{a}{y}, \frac{y}{(4\alpha t)^{1/2}}\right) \quad \text{(A8}b\text{)}$$

The functions in the three terms on the right in (A8b) are respectively the exponential integral, the error function, and the 'Smith' function; they can be represented as follows:

$$E_i(-u) \equiv -\int_u^\infty e^{-v}\frac{dv}{v} \quad \text{(A9}a\text{)}$$

$$\simeq 0.5772 - \ln u - u \qquad u^2 \ll 1 \quad \text{(A9}b\text{)}$$

$$\operatorname{erf} u \equiv \frac{2}{\sqrt{\pi}}\int_0^u e^{-v^2}\, dv \quad \text{(A10}a\text{)}$$

$$\simeq \frac{2}{\sqrt{\pi}}u \qquad u^2 \ll 1 \quad \text{(A10}b\text{)}$$

$$S(u, m) \equiv \frac{1}{\pi}\int_0^u e^{-m^2(v^2+1)}\frac{dv}{v^2+1} \quad \text{(A11}a\text{)}$$

$$\simeq \frac{1}{\pi}[\tan^{-1} u - um^2] \qquad u^2m^2 \ll 1 \quad \text{(A11}b\text{)}$$

$$\to \frac{1}{2}(1 - \operatorname{erf} m) \qquad u \to \infty \quad \text{(A11}c\text{)}$$

Tables of the exponential integral and the error function are, of course, available in standard handbooks. The function S has been discussed and tabulated by *Smith* [1953] and *Lachenbruch* [1957].

Applying (A9), (A10), and (A11) to (A8) yields the steady state result:

$$\theta(x, y, \infty) = \frac{Q_c}{4\pi k}\Big\{(x_2+x)\ln[y^2+(x_2+x)^2] - (x_1+x) \cdot \ln[y^2+(x_1+x)^2] - (x_2-x)\ln[y^2+(y_2-x)^2] + (x_1-x)\ln[y^2+(x_1-x)^2] + 2y\left[\tan^{-1}\frac{x_2+x}{y} - \tan^{-2}\frac{x_1+x}{y} - \tan^{-1}\frac{x_2-x}{y} + \tan^{-1}\frac{x_1-x}{y}\right]\Big\} \quad \text{(A12)}$$

The temperature in the plane of the fault is obtained by setting $y = 0$ in (A8)

$$\theta(x, 0, t) = \frac{Q_c}{k}\sqrt{\frac{\alpha t}{\pi}}\left\{\frac{1}{2(\pi)^{1/2}}\left[\frac{x_2+x}{(4\alpha t)^{1/2}}E_i\left(-\frac{(x_2+x)^2}{4\alpha t}\right) - \frac{x_1+x}{(4\alpha t)^{1/2}}E_i\left(-\frac{(x_1+x)^2}{4\alpha t}\right) - \frac{(x_2-x)}{(4\alpha t)^{1/2}}E_i\left(-\frac{(x_2-x)^2}{4\alpha t}\right) + \frac{x_1-x}{(4\alpha t)^{1/2}}E_i\left(-\frac{(x_1-x)^2}{4\alpha t}\right)\right] + \frac{1}{2}\left[-\operatorname{erf}\frac{x_2+x}{(4\alpha t)^{1/2}} + \operatorname{erf}\frac{x_1+x}{(4\alpha t)^{1/2}} + \operatorname{erf}\frac{x_2-x}{(4\alpha t)^{1/2}} - \operatorname{erf}\frac{x_1-x}{(4\alpha t)^{1/2}}\right]\right\} \quad \text{(A13)}$$

The factor in front of the braces is the corresponding result for an infinite plane source, and the expression in braces represents edge effects, which, of course, ultimately dominate as the steady state is approached.

The Case of a Linear Increase in Source Strength With Depth

For convenience, we take the linear increase to be of the following form:

$$Q(x) = Q^*\frac{x}{x^*} \qquad x_1 < x < x_2$$

$$Q(x) = 0 \qquad 0 < x < x_1 \qquad x_2 < x$$

The complete transient solution for this case is unwieldy, and we solve only for the temperature on the fault plane $y = 0$. Substituting the above expression in (A1) yields

$$\theta(x, 0, t) = \frac{Q^*}{4\pi k x^*} \int_{x_1}^{x_2} - E_i\left(-\frac{(x^1 - x)^2}{4\alpha t}\right) + E_i\left(-\frac{(x + x^1)^2}{4\alpha t}\right) x^1 \, dx' \quad \text{(A14)}$$

and a change of variables leads to

$$\frac{4\pi k x^*}{Q^*}\theta(x, 0, t) = 4\alpha t \cdot \left\{ \int_{(x_1+x)/(4\alpha t)^{1/2}}^{(x_2+x)/(4\alpha t)^{1/2}} - \int_{(x_1-x)/(4\alpha t)^{1/2}}^{(x_2-x)/(4\alpha t)^{1/2}} E_i(-\beta^2)\beta \, d\beta - \frac{x}{(4\alpha t)^{1/2}} \cdot \left[\int_{(x_1+x)/(4\alpha t)^{1/2}}^{(x_2+x)/(4\alpha t)^{1/2}} + \int_{(x_1-x)/(4\alpha t)^{1/2}}^{(x_2-x)/(4\alpha t)^{1/2}} E_i(-\beta^2) \, d\beta \right] \right\} \quad \text{(A15)}$$

From (A4) and (A6) the integrals within the brackets yield results of the form:

$$-\frac{x}{(4\alpha t)^{1/2}} \int_a^b E_i(-\beta^2) \, d\beta = -\frac{x}{(4\alpha t)^{1/2}} \{ bE_i(-b^2) - aE_i(-a^2) - \sqrt{\pi} [\operatorname{erf} b - \operatorname{erf} a] \} \quad \text{(A16)}$$

In the first two integrals of (A15), integration by parts yields results of the following form:

$$\int_a^b E_i(-\beta^2)\beta \, d\beta = \frac{1}{2} [b^2 E_i(-b^2) - a^2 E_i(-a^2) + e^{-b^2} - e^{-a^2}] \quad \text{(A17)}$$

and the final result is

$$\theta(x, 0, t) = \frac{Q^*}{8\pi k} \frac{1}{x^*} \left\{ (x_2^2 - x^2) \cdot \left[E_i\left(-\frac{(x_2 + x)^2}{4\alpha t}\right) - E_i\left(-\frac{(x_2 - x)^2}{4\alpha t}\right) \right] - (x_1^2 - x^2) \left[E_i\left(-\frac{(x_1 + x)^2}{4\alpha t}\right) - E_i\left(-\frac{(x_1 - x)^2}{4\alpha t}\right) \right] + 4\alpha t [e^{-(x_2+x)^2/(4\alpha t)} - e^{-(x_2-x)^2/(4\alpha t)} - e^{-(x_1+x)^2/(4\alpha t)} + e^{-(x_1-x)^2/(4\alpha t)}] + 2\sqrt{4\pi\alpha t}\, x \left[\operatorname{erf} \frac{x_2 + x}{(4\alpha t)^{1/2}} + \operatorname{erf} \frac{x_2 - x}{(4\alpha t)^{1/2}} - \operatorname{erf} \frac{x_1 + x}{(4\alpha t)^{1/2}} - \operatorname{erf} \frac{x_1 - x}{(4\alpha t)^{1/2}} \right] \right\} \quad \text{(A18)}$$

The most useful case, in which the source strength increases from zero at the surface to Q^* at depth x_2, results in a slight simplification (by setting $x_1 = 0$, $x_2 = x^*$):

$$\theta(x, 0, t) = \frac{Q^*}{8\pi k} \frac{1}{x_2} \left\{ (x_2^2 - x^2) \cdot \left[E_i\left(-\frac{(x_2 + x)^2}{4\alpha t}\right) - E_i\left(-\frac{(x_2 - x)^2}{4\alpha t}\right) \right] + 4\alpha t [e^{-(x_2+x)^2/(4\alpha t)} - e^{-(x_2-x)^2/(4\alpha t)}] + 2\sqrt{4\pi\alpha t}\, x \left[\operatorname{erf} \frac{x_2 + x}{(4\alpha t)^{1/2}} + \operatorname{erf} \frac{x_2 - x}{(4\alpha t)^{1/2}} \right] \right\} \quad \text{(A19)}$$

In the steady state, this reduces to

$$\theta(x, 0, \infty) = \frac{Q^*}{8\pi k} \frac{1}{x_2} \left[(x_2^2 - x^2) \ln \frac{(x_2 + x)^2}{(x_2 - x)^2} + 8x_2 x \right] \quad \text{(A20)}$$

Heat Flow at the Earth's Surface ($x = 0$)

The transient build-up of heat flux q at the earth's surface ($x = 0$) is obtained by differentiation of (A1):

$$q(y, t) = \frac{1}{\pi} \int_{x_1}^{x_2} e^{-(x'^2+y^2)/(4\alpha t)} \frac{x'}{x'^2 + y^2} Q(x') \, dx' \quad \text{(A21)}$$

For the case of a constant source strength Q_c, this yields

$$q(y, t) = \frac{Q_c}{2\pi} \left[E_i\left(-\frac{x_2^2 + y^2}{4\alpha t}\right) - E_i\left(-\frac{x_1^2 + y^2}{4\alpha t}\right) \right] \quad \text{(A22a)}$$

$$\rightarrow \frac{Q_c}{2\pi} \ln \frac{x_2^2 + y^2}{x_1^2 + y^2} \qquad t \rightarrow \infty \quad \text{(A22b)}$$

For the case (corresponding to (A19)) of a linearly increasing source extending from the surface to depth x_2, manipulations similar to those used above lead to

$$q(y, t) = \frac{Q^*}{2\pi x_2} \left\{ \sqrt{4\pi\alpha t}\, e^{-y^2/(4\alpha t)} \operatorname{erf} \frac{x_2}{(4\alpha t)^{1/2}} - 2\pi y S\left(\frac{x_2}{y}, \frac{y}{(4\alpha t)^{1/2}}\right) \right\} \quad \text{(A23a)}$$

$$\rightarrow \frac{Q^*}{\pi} \left[1 - \frac{y}{x_2} \tan^{-1} \frac{x_2}{y} \right] \qquad t \rightarrow \infty \quad \text{(A23b)}$$

where S is the 'Smith' function described earlier (A11).

APPENDIX B: AN APPROXIMATION FROM BYERLEE'S LAW FOR FRICTIONAL STRENGTH IN THE UPPER CRUST

Byerlee's [1978] summary of extensive laboratory measurements of stress on sliding rock surfaces shows that for a wide variety of rock materials, the maximum shearing stress on the sliding surface τ_m attained during each experiment can be expressed in terms of the normal stress σ_n on that surface as follows:

$$\tau_m = C + \mu(\sigma_n - P) \quad \text{(B1a)}$$

where

$$C = 0 \quad \mu \simeq 0.85 \quad \text{if} \quad 0.1 \text{ kbar} < (\sigma_n - P) < 2 \text{ kbar} \quad \text{(B1b)}$$

$$C = 0.5 \text{ kbar} \quad \mu = 0.6 \quad \text{if} \quad 2 \text{ kbar} < (\sigma_n - P) < 15 \text{ kbar} \quad \text{(B1c)}$$

Pore fluid pressure is denoted by P, and the expression in parenthesis is effective normal stress denoted hereafter by σ_n'.

For analytical convenience, we use the following approximation for (B1) [see also *Zoback and Zoback*, 1980]:

$$\tau_m \simeq \mu\sigma_n' \qquad \sigma_n' < 6 \text{ kbar} \quad \text{(B2a)}$$

$$\mu = 0.75 \quad \text{(B2b)}$$

This relation does not depart from (B1) by more than about 11% for a range of effective normal stress from 0 to 6 kbar,

sufficient to accommodate conditions in the upper 15 km or so of the crust. If we let ϕ be the angle formed by the trace of the fault and the direction of greatest principal stress σ_1, the effective normal and shear stresses on the fault plane are given by [e.g., *Jaeger*, 1962]

$$\sigma_n' = \tfrac{1}{2}(\sigma_1' + \sigma_3') - \tfrac{1}{2}(\sigma_1' - \sigma_3')\cos 2\theta \qquad \text{(B3}a\text{)}$$

$$\tau_m = \tfrac{1}{2}(\sigma_1' - \sigma_3')\sin 2\theta \qquad \text{(B3}b\text{)}$$

Combination of (B2a) and (B3) yields

$$\frac{\sigma_3'}{\sigma_n} = 1 - \mu\,\frac{2(\sin\theta)^2}{\sin 2\theta} \qquad \text{(B4)}$$

Assuming fault failure occurs in the most favorably oriented fracture direction,

$$\theta = \frac{1}{2}\left[\frac{\pi}{2} - \tan^{-1}\mu\right] \qquad \text{(B5}a\text{)}$$

$$= 26.6° \qquad \mu = 0.75 \qquad \text{(B5}b\text{)}$$

which leads to the following general relations [see also *Brace and Kohlstedt*, 1980]:

$$\frac{\sigma_n'}{\sigma_3'} = 1.6 \qquad \text{(B6}a\text{)}$$

$$\frac{\sigma_1'}{\sigma_3'} = 4.0 \qquad \text{(B6}b\text{)}$$

$$\frac{\sigma_n'}{\sigma_{avg}'} = 0.64 \qquad \text{(B6}c\text{)}$$

where

$$\sigma_{avg}' = \tfrac{1}{2}(\sigma_1' + \sigma_3') \qquad \text{(B7)}$$

Thus the frictional strength (B1) can be expressed in terms of the effective normal stress, the greatest, least, and average effective principal stresses and the difference in horizontal principal stresses as follows:

$$\tau_m = 0.75\,\sigma_n' \qquad \text{(B8}a\text{)}$$

$$= 1.2\,\sigma_3' \qquad \text{(B8}b\text{)}$$

$$= 0.30\,\sigma_1' \qquad \text{(B8}c\text{)}$$

$$= 0.48\,\sigma_{avg}' \qquad \text{(B8}d\text{)}$$

$$= 0.40\,(\sigma_1 - \sigma_3) \qquad \text{(B8}e\text{)}$$

Acknowledgment. We are very grateful to Robert Jachens and Andrew Griscom for advising us of the unpublished results of their recent gravity study near Cape Mendocino. In addition, we thank Thomas Hanks, Barry Raleigh, Wayne Thatcher, Malcolm Johnston, James Savage, Joe Walsh, and Tanya Atwater for helpful discussion and suggestions.

REFERENCES

Anderson, D. L., The San Andreas fault, *Sci. Am., 225,* 52–68, 1971.

Andrews, D. J., Application of rupture propagation theories to earthquakes, *U.S. Geol. Surv. Open File Rep., 78-380,* 33–70, 1978*a*.

Andrews, D. J., Coupling of energy between tectonic processes and earthquakes, *J. Geophys. Res., 83,* 2259–2264, 1978*b*.

Atwater, T., and P. Molnar, Relative motion of the Pacific and North American plates deduced from sea-floor spreading in the Atlantic, Indian, and south Pacific Oceans, in *Proceedings of the Conference on the Tectonic Problems of the San Andreas Fault System,* pp. 136–148, Stanford University Press, Palo Alto, Calif., 1973.

Benfield, A. E., A heat flow value for a well in California, *Am. J. Sci., 245,* 1–18, 1947.

Berg, C. A., Relation between stress drop, fault friction, and crustal strength in shallow focus strike slip faulting, *J. Geophys. Res., 73,* 2217–2223, 1968.

Berry, F. A. F., High fluid potentials in California Coast Ranges and their tectonic significance, *Am. Assoc. Pet. Geol. Bull., 57,* 1219–1249, 1973.

Blackwell, D. D., Heat flow and energy loss in the Western United States, *Geol. Soc. Am. Mem., 152,* 175–208, 1978.

Brace, W. F., Permeability of crystalline and argillaceous rocks: Status and problems, *Int. J. Rock Mech. Min. Sci.,* in press, 1980.

Brace, W. F., and D. L. Kohlstedt, Limits on crustal stress imposed by laboratory experiments, *J. Geophys. Res., 85,* this issue, 1980.

Brace, W. F., and J. B. Walsh, Some direct measurements of the surface energy of quartz and orthoclase, *Am. Mineral., 47,* 1111–1122, 1962.

Brook, C. A., R. H. Mariner, D. R. Mabey, J. R. Swanson, M. Guffanti, and L. J. P. Muffler, Hydrothermal convection systems with reservoir temperatures ≥90°C, *U.S. Geol. Surv. Circ., 790,* 18–85, 1979.

Brune, J. N., The physics of earthquake strong motion, in *Seismic Risk and Engineering Decisions, Develop. in Geotech. Eng.,* 15, edited by E. Rosenbluthe and C. Lomnitz, pp. 141–177, Elsevier, New York, 1976.

Brune, J. N., T. L. Henyey, and R. F. Roy, Heat flow, stress, and rate of slip along the San Andreas fault, California, *J. Geophys. Res., 74,* 3821–3827, 1969.

Burridge, R., and G. S. Halliday, Dynamic shear cracks with friction as models for shallow focus earthquakes, *Geophys. J. Roy. Astron. Soc., 25,* 261–283, 1971.

Byerlee, J. D., Static and kinetic friction of granite at high normal stress, *Int. J. Rock Mech. Min. Sci., 7,* 577–582, 1970.

Byerlee, J. D., Friction of rocks, *Pure Appl. Geophys., 116,* 615–626, 1978.

Cardwell, R. K., D. S. Chinn, G. F. Moore, and D. L. Turcotte, Frictional heating on a fault zone with finite thickness, *Geophys. J. Roy. Astron. Soc., 52,* 525–530, 1978.

Carslaw, H. S., and J. C. Jaeger, *Conduction of Heat in Solids,* 386 pp., Oxford University Press, New York, 1959.

Combs, J., Heat flow and geothermal resource estimates for the Imperial Valley, in *Cooperative Geological-Geophysical-Geochemical Investigations of Geothermal Resources in the Imperial Valley Area of California,* pp. 5–27, Education Research Service, University of California, Riverside, Calif., 1971.

Dickinson, W. R., and W. S. Snyder, Geometry of subducted slabs related to San Andreas transform, *J. Geol., 87,* 609–627, 1979.

Eaton, J. P., W. H. K. Lee, and L. C. Pakiser, Use of micro-earthquakes in the study of the mechanics of earthquake generation along the San Andreas fault in central California, *Tectonophysics, 9,* 259–282, 1970.

Graham, S. A., and W. R. Dickinson, Evidence for 115 kilometers of right-slip on the San Gregorio-Hosgri fault trend, *Science, 199,* 179–181, 1978.

Hanks, T. C., Earthquake stress drops, ambient tectonic stresses and stresses that drive plate motions, *Pure Appl. Geophys., 115,* 441–458, 1977.

Henyey, T. L., Heat flow near major strike-slip faults in California, Ph.D. thesis, Calif. Inst. of Technol., Pasadena, Calif., 1968.

Henyey, T. L., and G. J. Wasserburg, Heat flow near major strike-slip faults in California, *J. Geophys. Res., 76,* 7924–7946, 1971.

Irwin, W. P., and I. Barnes, Effect of geologic structure and metamorphic fluids on seismic behavior of the San Andreas fault system in central and northern California, *Geology, 3,* 713–716, 1975.

Jaeger, J. C., *Elasticity, Fracture and Flow,* Methuen, London, 1962.

Jennings, C. W., Fault map of California, scale 1:750,000, *Calif. Geol. Map Ser.,* map 1, 1975.

Johnson, A. G., R. L. Kovach, and A. Nur, Fluid-pressure variations and fault creep in central California, *Tectonophysics, 23,* 257–266, 1974.

Kanamori, H., and D. L. Anderson, Theoretical basis of some empirical relations in seismology, *Bull. Seismol. Soc. Am., 65,* 1073–1095, 1975.

Lachenbruch, A. H., Thermal effects of the ocean on permafrost, *Geol. Soc. Am. Bull., 68,* 1515–1530, 1957.

Lachenbruch, A. H., Heat flow in the Basin and Range Province and thermal effects of tectonic extension, *Pure Appl. Geophys., 117,* 34–50, 1978.

Lachenbruch, A. H., Frictional heating, fluid pressure, and the resistance to fault motion, *J. Geophys. Res., 85,* this issue, 1980.

Lachenbruch, A. H., and J. H. Sass, Thermo-mechanical aspects of the San Andreas fault system, in *Proceedings of the Conference on the Tectonic Problems of the San Andreas Fault System,* pp. 192–205, Stanford University Press, Palo Alto, Calif., 1973.

Lachenbruch, A. H., and J. H. Sass, Heat flow in the United States and the thermal regime of the crust, in *The Earth's Crust, Geophys. Monogr. Ser.,* vol. 20, edited by J. G Heacock, pp. 626–675, AGU, Washington, D. C., 1977.

Lachenbruch, A. H., and J. H. Sass, Models of an extending lithosphere and heat flow in the Basin and Range province, *Geol. Soc. Am. Mem., 152,* 209–250, 1978.

Lachenbruch, A. H., and J. H. Sass, Heat flow and energetics of the San Andreas fault zone, *U.S. Geol. Surv. Open File Rep., 80-625,* 47–146, 1980.

Lachenbruch, A. H., J. H. Sass, and S. P. Galanis, Jr., New heat flow results from southern California (abstract), *Eos Trans. AGU, 59,* 1051, 1978.

Lee, T. C., and T. L. Henyey, Heat flow through the southern California borderland, *J. Geophys. Res., 80,* 3733–3743, 1975.

McGarr, A., S. M. Spottiswoode, and N. C. Gay, Observations relevant to seismic driving stress, stress drop, and efficiency, *J. Geophys. Res., 84,* 2251–2261, 1979.

Melosh, H. J., Acoustic fluidization: A new geologic process?, *J. Geophys. Res., 84,* 7513–7520, 1979.

Murata, K. J., T. W. Dibblee, Jr., and J. L. Drinkwater, Thermal effects of large bodies of intrusive serpentinite on overlying Monterey shale; Southern Diablo Range, Cholame area, California, *U.S. Geol. Surv. Prof. Pap., 1082,* 1979.

Nur, A., and J. D. Byerlee, An exact effective stress law for elastic deformation of rock with fluids, *J. Geophys. Res., 76,* 6414–6419, 1971.

Olmsted, F. H., P. A. Glancy, J. R. Harrill, F. E. Rush, and A. S. VanDenburgh, Preliminary hydrogeologic appraisal of selected hydrothermal systems in northern and central Nevada, *U.S. Geol. Surv. Open File Rep., 75-56,* 1975.

O'Neil, J. R., and T. C. Hanks, Geochemical evidence for interaction along the San Andreas and Garlock faults of California, *J. Geophys. Res., 85,* this issue, 1980.

Pilger, R. H., Jr., and T. L. Henyey, Pacific-North American plate interaction and neogene volcanism in coastal California, *Tectonophysics, 57,* 189–209, 1979.

Renner, J. L., D. E. White, and D. L. Williams, Hydrothermal convection systems, *U.S. Geol. Surv. Circ., 726,* 5–57, 1975.

Richards, P. G., Dynamic motions near an earthquake fault: A three-dimensional solution, *Bull. Seismol. Soc. Am., 66,* 1–32, 1976.

Roy, R. F., D. D. Blackwell, and E. R. Decker, Continental heat flow, in *The Nature of the Solid Earth,* edited by E. C. Robertson, pp. 506–543, McGraw-Hill, New York, 1972.

Rutter, E. H., and D. H. Mainprice, The effect of water on stress relaxation of faulted and unfaulted sandstone, *Pure Appl. Geophys., 116,* 634–654, 1978.

Sammel, E. A., Occurrence of low temperature geothermal waters in the United States, *U.S. Geol. Surv. Circ., 790,* 86–131, 1979.

Sass, J. H., A. H. Lachenbruch, R. J. Munroe, G. W. Greene, and T. H. Moses, Jr., Heat flow in the western United States, *J. Geophys. Res., 76,* 6376–6413, 1971.

Sass, J. H., D. D. Blackwell, D. S. Chapman, J. K. Costain, E. R. Decker, L. A. Lawver, and C. A. Swanberg, Heat flow from the crust of the United States, in *Physical Properties of Rocks and Minerals,* edited by Y. S. Touloukian, W. R. Judd, and R. F. Roy, McGraw-Hill, New York, in press, 1980.

Savage, J. C., and R. O. Burford, Geodetic determination of relative plate motion in central California, *J. Geophys. Res., 78,* 832–845, 1973.

Savage, J. C., and M. D. Wood, The relation between apparent stress and stress drop, *Bull. Seismol. Soc. Am., 61,* 1381–1388, 1971.

Savage, J. C., W. H. Prescott, M. Lisowski, and N. King, Deformation across the Salton Trough, California, 1973–1977, *J. Geophys. Res., 84,* 3069–3079, 1979.

Scholz, C. H., J. Beavan, and T. C. Hanks, Metamorphism, argon depletion, heat flow, and stress on the Alpine fault, *J. Geophys. Res., 84,* 6770–6782, 1979.

Sibson, R. H., Interactions between temperature and pore-fluid pressure during an earthquake faulting and a mechanism for partial or total stress relief, *Nature, 243,* 66–68, 1973.

Sieh, K., Study of Holocene displacement history along the south-central reach of the San Andreas fault, Ph.D. thesis, 219 pp., Stanford Univ., Stanford, Calif., 1977.

Smith, R. C. T., Conduction of heat in the semi-infinite solid with a short table of an important integral, *Aust. J. Phys., 6,* 127–130, 1953.

Stesky, R. M., Rock friction-effect of confining pressure, temperature, and pore pressure, *Pure Appl. Geophys., 116,* 690–704, 1978.

Stesky, R. M., and W. F. Brace, Estimation of frictional stress on the San Andreas fault from laboratory measurements, in *Proceedings of the Conference on Tectonic Problems of the San Andreas Fault System,* pp. 206–214, Stanford University Press, Palo Alto, Calif., 1973.

Summers, R., and J. Byerlee, A note on the effect of fault gouge composition on the stability of frictional sliding, *Int. J. Rock Mech. Min. Sci. Geomech. Abstr., 14,* 155–160, 1977.

Taylor, H. P., Jr., Oxygen and hydrogen isotope studies of plutonic granitic rocks, *Earth Planet. Sci. Lett., 38,* 177–210, 1978.

Thatcher, W., Systematic inversion of geodetic data in central California, *J. Geophys. Res., 84,* 2283–2295, 1979*a*.

Thatcher, W., Horizontal crustal deformation from historic geodetic measurements in southern California, *J. Geophys. Res., 84,* 2351–2370, 1979*b*.

Wang, C.-Y., and N.-H. Mao, Shearing of saturated clays in rock joints at high confining pressures, *Geophys. Res. Lett., 6,* 825–828, 1979.

Waring, G. A., Thermal springs of the United States and other countries of the world, *U.S. Geol. Surv. Prof. Pap., 492,* 1965.

Wu, F. T., Mineralogy and physical nature of clay gouge, *Pure Appl. Geophys., 116,* 655–689, 1978.

Wyss, M., Stress estimates for South American shallow and deep earthquakes, *J. Geophys. Res., 75,* 1529–1544, 1970.

Wyss, M., and J. N. Brune, Seismic moment, stress, and source dimensions for earthquakes in the California-Nevada region, *J. Geophys. Res., 73,* 4681–4694, 1968.

Yuen, D. A., L. Fleitout, G. Schubert, and C. Froidevaux, Shear deformation zones along major transform faults and subducting slabs, *Geophys. J. Roy. Astron. Soc., 54,* 93–119, 1978.

Zoback, M. L., and M. D. Zoback, Faulting patterns in north-central Nevada and strength of the crust, *J. Geophys. Res., 85,* 275–284, 1980.

(Received February 27, 1980;
revised May 2, 1980;
accepted June 25, 1980.)